Mechanical Properties and Tension-Tension Fatigue Behavior of a Novel Additively Manufactured Polymer Matrix Composite at Room and Elevated Temperature

THESIS

Grayson M. Harber, Captain, USAF

AFIT-ENY-MS-22-S-119

DEPARTMENT OF THE AIR FORCE
AIR UNIVERSITY

AIR FORCE INSTITUTE OF TECHNOLOGY

Wright-Patterson Air Force Base, Ohio

DISTRIBUTION STATEMENT A.
APPROVED FOR PUBLIC RELEASE; DISTRIBUTION UNLIMITED.

The views expressed in this thesis are those of the author and do not reflect the official policy or position of the United States Air Force, Department of Defense, or the United States Government. This material is declared a work of the U.S. Government and is not subject to copyright protection in the United States.

AFIT-ENY-MS

Mechanical Properties and Tension-Tension Fatigue Behavior of a Novel Additively Manufactured Polymer Matrix Composite at Room and Elevated Temperature

THESIS

Presented to the Faculty

Department of Aeronautics and Astronautics

Graduate School of Engineering and Management

Air Force Institute of Technology

Air University

Air Education and Training Command

In Partial Fulfillment of the Requirements for the

Degree of Master of Science in Materials Science

Grayson M. Harber, BS

Captain, USAF

July 2022

DISTRIBUTION STATEMENT A.
APPROVED FOR PUBLIC RELEASE; DISTRIBUTION UNLIMITED.

AFIT-ENY-MS

Mechanical Properties and Tension-Tension Fatigue Behavior of a Novel Additively Manufactured Polymer Matrix Composite at Room and Elevated Temperature

Grayson M. Harber, BS

Captain, USAF

Committee Membership:

Dr. Marina Ruggles-Wrenn
Chair

Dr. Jevan Furmanski
Member

Maj Ryan Kemnitz, PhD
Member

Abstract

The tension-tension fatigue behavior of a novel additively manufactured (AM) carbon fiber reinforced polymer matrix composite was studied. This novel material system consists of T1100 carbon fibers, and a UV photocured resin developed by Continuous Composites and Sartomer. Tensile properties and tension-tension fatigue were investigated for the 0/90 fiber orientation as well as for the ±45 fiber orientation. Specimens with 0/90 fiber orientation were tested at ambient lab temperature (23 °C) and at elevated temperature (150 °C), while the specimens with the ±45 fiber orientation was tested only at ambient lab temperature. Tension-tension fatigue testing was carried out with a frequency of 1 Hz, and a ratio of minimum to maximum stress of R=0.1. Fatigue runout for this investigation was defined as 200,000 cycles. Results obtained for the AM composite in this study were compared to the results obtained in previous studies for traditionally manufactured (TM) aerospace-grade carbon fiber/resin composite systems. The tension-tension fatigue performance of the additively manufactured material system with 0/90 fiber orientation was somewhat worse than that of the traditionally manufactured aerospace-grade composites with 0/90 fiber orientation at both room and elevated temperature. The additively manufactured material system ±45 fiber orientation exhibited better tension-tension fatigue performance than the ±45 aerospace-grade composite. The AM composite exhibited considerable degree of specimen-to-specimen variability, and consequently considerable data scatter. Before testing the AM composite specimens were imaged using X-Ray Computed Tomography in order to gain insight into how the unique microstructure produced by this novel fabrication method impacts mechanical behavior. The X-Ray Computed Tomography images were instrumental in explaining some of the anomalous behaviors, as well as the

specimen-to-specimen variability of the AM composite for elastic modulus. The additive manufacturing process shows considerable promise for rapid and cost-effective fabrication of composite parts. However, at present additive manufacturing produces composites with numerous internal defects and unordered microstructure that cause wide variability in both the mechanical properties and mechanical response of each specimen. The microstructure of each specimen must become much more consistent from one specimen to another. Until a consistent mechanical response can be achieved for each specimen, this material will be unsuitable for structural applications.

Acknowledgments

I would like to first and foremost thank God for carrying me through this effort. I want to thank my wife for standing by me and enabling me to devote my time to the creation of this thesis. I would like to thank Dr. Ruggles-Wrenn for her guidance and patience during this research. I would like to thank Dr. Furmanski for capturing the X-Ray CT images presented in this thesis. I would like to thank Maj Ryan Kemnitz for giving his time to hear the defense of this thesis. I would also like to thank Mr. Mike Ranft and Mr. Jamie Smith for their time and attention to fixing the myriad of issues that would have prevented this thesis from being written. I would not have gotten to this point without the concerted efforts of all of the individuals listed above, and I cannot put into words how grateful I am for your assistance.

Grayson M. Harber

Table of Contents

Abstract v
Acknowledgments vii
Table of Contents viii
List of Figures x
List of Tables xiii
I. Introduction 14
1.1 Motivation 14
1.2 Problem Statement 16
1.3 Research Objectives 17
1.4 Methodology 18
II. Background 19
2.1 Composite Materials 19
2.2 Polymer Matrix Composites 20
2.2.1 Polymer Matrices 20
2.2.2 Reinforcing Fibers 21
2.2.3 Fiber Architectures 22
2.3 Polymer Matrix Composites - Traditional Manufacturing (TM) 23
2.4 Polymer Matrix Composites - Novel Manufacturing Method 25
2.5 Mechanical Behavior of Polymer Matrix Composites 28
2.5.1 Tensile Behavior 28
2.5.2 Fatigue Behavior 29
2.5.3 Temperature Effects 30
2.6 Previous Research 31
2.6.1 Additively Manufactured Polymer Matrix Composites 31
III. Materials and Test Specimens 33
3.1 Novel Additivity Manufactured Polymer Matrix Composite 33
3.2 Specimen Geometry 35
3.3 Specimen Preparation 35
IV. Experimental Setup and Testing Procedures 38

4.1 Testing Equipment 38
4.2 Tuning of Testing Equipment 40
4.3 Mechanical Testing Procedures 44
4.3.1 Room Temperature Elastic Modulus Measurements 44
4.3.2 Monotonic Tensile Tests 44
4.3.3 Tension-Tension Fatigue Tests 45
4.4 Optical Microscopy 46
4.5 X-Ray Computed Tomography 46
V. Experimental Results and Discussion 48
5.1 Assessment of Specimen-to-Specimen Variability 48
5.2 Thermal Expansion 52
5.3 Monotonic Tensile Tests 54
5.3.1 Monotonic Tension at Room Temperature 55
5.3.2 Monotonic Tension at Elevated Temperature 58
5.3.3 Comparison of AM-PMC and TM-PMC Monotonic Tension Behavior 60
5.4 Tension-Tension Fatigue at 23 °C 63
5.4.1 Fatigue Performance of the 0/90 AM-PMC 63
5.4.1.1 Comparison of 0/90 AM-PMC and TM-PMC Fatigue Performance 70
5.4.2 Fatigue Performance of the ±45 AM-PMC 71
5.4.2.1 Comparison of ±45 AM-PMC and TM-PMC Fatigue Performance 76
5.5 Tension-Tension Fatigue at 150 °C 78
5.5.1 Fatigue Performance of the 0/90 AM-PMC at 150 °C 78
5.5.1.1 Comparison of Fatigue Performance at 23 °C and 150 °C 81
5.5.1.2 Comparison of AM-PMC and TM-PMC Fatigue Performance at Elevated Temperature 85
5.6 Retained Tensile Properties 87
5.7 Optical Microscopy 91
5.8 X-Ray Computed Tomography 94
5.8.1 Correlation of CT Images with Initial Elastic Modulus Measurements 95
5.8.2 Correlation of CT Images with Tension-Tension Fatigue Results 106
VI. Conclusions and Recommendations 111
6.1 Conclusions 111
6.2 Recommendations 112

Bibliography 114

List of Figures

Figure 1. A system that prints composite parts with a thermoplastic matrix material..... 26
Figure 2. The print system used by Continuous Composites® 27
Figure 3. A representative stress strain curve for a polymer matrix composite and its separate phases [8]. 29
Figure 4. A notional S-N curve [8]. 30
Figure 5. A schematic showing the effects of the stiffness of the phases of a polymer matrix composite on the shift of the composite's S-N curve. 31
Figure 6. Standard dogbone-shaped tensile specimen. 35
Figure 7. Average percent weight loss vs. time for each composite panel. 37
Figure 8. Equipment shown is a) station #1, b) station #2, c) station #3, d) room temperature knife edge extensometer, e) silica rod high temperature extensometer, f) single crystal silica high temperature extensometer 40
Figure 9. Displacement and displacement command versus time for specimen 313-1. Note that displacement is on an absolute scale..... 41
Figure 10. Displacement and displacement command versus time for station one. Note that displacement is on an absolute scale..... 42
Figure 11. Range of tuning responses when P gain is plotted against D gain [15] 43
Figure 12. The optical microscope used to take optical micrographs [16]..... 46
Figure 13. The X-Ray CT used for this effort with specimens installed for scanning 47
Figure 14. Modulus values for each specimen in panels 306 and 313 49
Figure 15. The two groupings of modulus values obtained for specimens in panel 306. One grouping occurs at the 85 GPa level, and the other at the 70 GPa level. 50
Figure 16. Specimen cutting plan for composite panels. Note 1: specimen number 14 does not exist. Note 2: specimens 1-13 oriented perpendicular to specimens 15-20. 50
Figure 17. Stacking sequence of specimens 1-13 (left) and specimens 15-20 (right) 51
Figure 18. Modulus values for the specimens of panel 314 52

Figure 19. Thermal strain measured for specimen 306-3 during temperature increase from 23 to 150 °C and thermal soak at 150 °C. 53
Figure 20. Typical tensile stress-strain curve obtained for the 0/90 composite at 23°C. 56
Figure 21. Typical tensile stress-strain curve obtained for the ±45 composite at 23 °C. 57
Figure 22. Typical tensile stress-strain curves obtained for the 0/90 and ±45 fiber orientations at room temperature. 58
Figure 23. Tensile stress-strain curve obtained for specimen 313-19 at 150 °C. 59
Figure 24. Tensile stress-strain curve obtained for specimen 306-18 at 150 °C. 60
Figure 25. Fatigue S-N curve obtained for the 0/90 AM-PMC at room temperature 64
Figure 26. Typical evolution of the stress-strain hysteresis response for the 0/90 AM-PMC specimens tested in tension-tension fatigue at 23 °C. Curves shifted by 0.1% for clarity. 65
Figure 27. Evolution of the stress-strain hysteresis response for specimen 306-9 tested in tension-tension fatigue at 23 °C (σ max = 656 MPa, Nf > 200,000). 66
Figure 28. Evolution of the stress-strain hysteresis response for specimen 306-9 between cycles 100,000 and 180,000, highlighting the visible step-up in damage development. 66
Figure 29. Evolution of the stress-strain hysteresis response for specimen 306-9 between cycles 100,000 and 170,000, highlighting the gradual damage development. 67
Figure 30. Evolution of the stress-strain hysteresis response for specimen 306-8 tested in tension-tension fatigue at 23 °C (σ max = 712 MPa, Nf = 9,543). 68
Figure 31. Normalized modulus vs cycles for specimens 306-15 (σ max = 605 MPa, Nf > 200,000), 306-17 (σ max = 650 MPa, Nf > 200,000), and 306-4 (σ max = 693 MPa, Nf > 200,000). 69
Figure 32. Normalized modulus vs cycles for specimen 306-8 (σ max = 712 MPa, Nf = 9,543). 70
Figure 33. Fatigue S-N curve obtained for ±45 AM-PMC at room temperature 72
Figure 34. Fatigue S-N curves obtained for 0/90 and ±45 AM-PMC specimens at room temperature. Maximum stress is shown in terms of %UTS. 73
Figure 35. Typical evolution of the stress-strain hysteresis response with cycles for the ±45 specimens 74
Figure 36. Normalized hysteretic modulus vs cycles for the ±45 specimens 75
Figure 37. Normalized hysteretic modulus vs cycles to failure for specimens 314-7, 314-8, 314-11, and 314-15 76

Figure 38. Actual maximum stress vs. cycles to failure (S-N) curve obtained for the 0/90 AM-PMC specimens at 150 °C 79
Figure 39. Normalized maximum stress vs. cycles to failure (S-N) curve obtained for the 0/90 AM-PMC specimens at 150 °C 80
Figure 40. Typical evolution of the stress-strain hysteresis response of the 0/90 AM-PMC at 150 °C (specimen 306-12, σ max = 718 MPa, Nf = 55,158). 80
Figure 41. Actual maximum stress vs. cycles to failure (S-N) curve obtained for the 0/90 AM-PMC specimens at 23 and 150 °C. 82
Figure 42. Normalized maximum stress vs. cycles to failure (S-N) curve obtained for the 0/90 AM-PMC specimens at 23 and 150 °C. 82
Figure 43. Evolution of the stress-strain hysteresis response for specimen 306-5 (σ max = 679 MPa, Nf = 65,563) tested in fatigue at 150 °C. 84
Figure 44. Post-fatigue tension to failure stress-strain curve for specimen 306-9 88
Figure 45. Modulus values for specimen 306-9, three distinct damage regimes. Modulus values are given in GPa 89
Figure 46. Optical micrograph showing typical failure of AD-PMC specimens with 0/90 fiber orientation (specimen 306-10, fatigue at 150 °C, σ max = 673 MPa, Nf = 4,856). 91
Figure 47. Specimen 313-4 before failure (left) and after failure (right) 92
Figure 48. Optical micrograph showing typical failure of AD-PMC specimens with ±45 fiber orientation (specimen 314-15, fatigue at 23 °C, σ max = 60 MPa, Nf = 14,932). (a) Front view, (b) side view, (c) opposite side view. 93
Figure 49. An X-Ray CT image of the gauge section of specimen 306-1 94
Figure 50. X-Ray CT images of test specimens cut from panel 306. Specimens are ordered by descending initial modulus value. Modulus values are given in units of GPa. 97
Figure 51. X-Ray CT images of specimens 306-1, 306-12, 306-15, and 306-20 with corresponding initial modulus values given in units of GPa. 99
Figure 52. X-Ray CT images of specimens 313-15, 313-16, 313-17, 313-18, 313-19, and 313-20 101
Figure 53. X-Ray CT images of test specimens cut from panel 314. Specimens are ordered by descending initial modulus value. Modulus values are given in units of GPa. 103
Figure 54. X-Ray CT image of specimen 314-19 105

Figure 55. X-Ray CT images of specimens tested at 23 °C in fatigue with the maximum stress level set to 85%UTS. Specimen 306-13 (σ max = 691 MPa, Nf = 30,648). Specimen 306-6 (σ max = 702 MPa, Nf = 180,780). Specimen 306-4 (σ max = 693 MPa, Nf > 200,000). 107
Figure 56. X-Ray CT images of the 0/90 specimens tested at 150 °C in fatigue with the maximum stress level set to 85%UTS. Specimen 306-5 (σ max = 679 MPa, Nf = 65,563). Specimen 306-3 (σ max = 678 MPa, Nf = 16,795). Specimen 306-10 (σ max = 673 MPa, Nf = 4,856). Specimen 313-20 (σ max = 678 MPa, Nf = 1,610). 108
Figure 57. X-Ray CT image of specimen 313-18 tested at 150 °C in fatigue with the maximum stress level set to 82.5%UTS (σ max = 653 MPa, Nf > 200,000). 109
Figure 58. X-Ray CT images of specimen 314-8 (σ max = 59 MPa, Nf = 168,010) and specimen 314-7 (σ max = 59 MPa, Nf = 22,617). 110

List of Tables

Table 1: Various fiber materials with their advantages and disadvantages [3] 21

Table 2: Average values (±standard deviation) of elastic modulus, maximum tensile strength and elongation at break for unfilled (B33 and B50) and fiber-reinforced (B33G5 and B50C5) composite materials. The mechanical properties of CFR composites containing sized 33

Table 3: Safety data sheet of the resin used in the research material [10]. 34

Table 4: Composite panel data provided by the manufacturer [10]..... 34

Table 5: General Specimen Information..... 35

Table 6: A summary of the measurements of each specimen from each panel. 36

Table 7: The settings for tuning displacement control..... 42

Table 8: Room temperature elastic modulus test results 48

Table 9: Thermal strains measured in elevated temperature fatigue tests 53

Table 10: Summary of tensile properties for the AD-composite at 23 °C and 150 °C..... 55

Table 11: Results of room-temperature tension to failure tests for 0/90 and ±45 specimens..... 55

Table 12: Tensile properties obtained for the AM composite with 0/90 fiber orientation at 150 °C 59

Table 13: Tensile properties obtained for two TM-PMCs at room and elevated temperatures. Data for IMR/977-3 composite from Lam [12]. Data for NRPE/T650-35 from Wilkinson [13]. 61

Table 14: Tension-tension fatigue results for the AM-PMC with 0/90 fiber orientation at 23 °C63

Table 15: Tension-tension fatigue results for the IM7/977-3 composite with 0/90 fiber orientation at 23 °C 70

Table 16: Tension-tension fatigue results for the AM-PMC with ±45 fiber orientation at 23 °C 71

Table 17: Tension-tension fatigue results for the IM7/977-3 composite with ±45 fiber orientation at 23 °C 77

Table 18: Tension-tension fatigue results for the AM-PMC with 0/90 fiber orientation at 150 °C 78

Table 19: Tension-tension fatigue results for the NRPE/T650-35 composite with 0/90 fiber orientation at 329 °C 86

Table 20: Retained tensile properties of the AM-PMC specimens subjected to 200,000 of prior fatigue at 23 or 150 °C 88

I. Introduction

1.1 Motivation

In order to ensure national security and to project power, the Air Force employs the most advanced assets in the world. The US has enjoyed an overwhelming technological advantage against its enemies since the end of the Cold War. The US has been the driver of innovation and technological advancement for many decades. However, innovation has accelerated all over the world. The age of tremendous technological advantage in the skies is coming to a close. The Air Force needs new and radical ideas to push forward in order to stay ahead of the innovation curve of the rest of the world if it is going to continue being the global dominant power.

The area of advancement that has enabled the modern military wonders such as the F-22, F-35, and B-2 is materials science. Without the advanced materials these aircraft would not be able to function. One material family that plays a major role in high performance aircraft is composite materials. A structural composite is a material system comprising two or more different phases, designed such that the mechanical performance and properties of the composite are superior to those of the constituent phases operating independently. The utilization of composites is exploding in the aerospace industry. The Boeing 787 is comprised of 50% composite material [1]. The Air Force needs to find new and innovative ways to embrace this trend or else it will fall behind.

Carbon fiber reinforced polymer-matrix composites offer distinct advantages over traditional materials. Their strength to weight ratio is far above that of metals. In aerospace applications, this property of utmost importance. Carbon fiber reinforced composites have been studied extensively, are reasonably well understood, and widely implemented in aerospace

applicaitons. Today the real opportunity for innovation is in the design and application of composite parts that would allow for the production of the highest performing aircraft in the world. It is critical that the Air Force operates the highest performing aircraft possible. This not only gives our Airmen the most survivability possible, but also enables the continued security of the interests of United States.

1.2 Problem Statement

Carbon fiber reinforced composite parts designed for the aerospace industry exhibit exceptionally high performance, but that performance comes at a high cost. Fabrication of carbon fiber reinforced composites is a lengthy and expensive process that offers few avenues for innovation. Due to the high cost of fabrication of composite parts, creating and testing new designs is a challenging process. The costly manufacturing process is holding back composites from being utilized in more aircraft applications. Additionally, current fabrication techniques limit composite parts to geometries that can be formed from two-dimensional sheets or panels. Aircraft parts of more complex geometries still have to be made from metallic alloys. Advances in composites fabrication that would produce three-dimensional parts could represent a new opening in the aerospace structures design space that could pay huge weight-saving dividends.

The Air Force Research Laboratory in collaboration with Continuous Composites Inc. (Coeur d'Alene, Idaho) has been investigating the use of additive manufacturing to produce aerospace-grade carbon fiber reinforced composite parts. Fabrication of composite parts via additive manufacturing would represent a massive leap forward in the composite innovation space. Successful use of additive manufacturing could reduce the cost of carbon fiber reinforced composite parts as well as enable fabrication of three-dimensional parts. This investigation has made considerable progress. The first batch of additively manufactured (AM) carbon fiber

reinforced composite panels has been fabricated successfully. However, before the AM composites can be further inserted into aircraft applications, their structural integrity and environmental durability must be assured. Basic mechanical properties of the AM composite panels must be measured and their response to basic types of mechanical loading must be studied. The results should be compared those obtained for the traditionally manufactured (TM) composites to ascertain that the benefits gained by additive manufacturing do not come at the cost of degraded mechanical properties and performance. This effort is a pilot study of the tensile elastic modulus, tensile strength, and tension-tension fatigue performance of a novel AM composite material, as well as fiber orientation.

1.3 Research Objectives

The objective of this research is to establish basic mechanical properties and characterize the tension-tension fatigue behavior of a novel AM composite material, and compare the performance of the AM composite to TM composites. Elastic modulus and ultimate tensile strength (UTS) of the composite material are determined for both 0/90 (on-axis) and ±45 (off-axis) fiber orientations. It is recognized that the fiber-dominated response of the 0/90 composite is dramatically different from the matrix-dominated response of the ±45 composite. Hence the mechanical properties and behavior of both 0/90 and ±45 fiber orientations must be thoroughly understood. Monotonic tension to failure tests are followed by tension-tension fatigue testing, both on-axis and off-axis. Tensile tests and cyclic fatigue tests are performed at room temperature (23 °C) as well as at 150 °C to explore the material performance over the in-service temperature range. The results obtained for the AM carbon fiber reinforced composite are compared to those obtained for the TM aerospace grade composite with similar constituents. Such comparison is critical to assessing the efficacy of additive manufacturing technique for

composite materials. The additive manufacturing process creates a unique microstructure, and the effects of this microstructure on mechanical behavior of composites are currently unknown. Pre- and post-test microstructure of test specimens is characterized using X-Ray computed tomography (CT) in an attempt to gain insight into the mechanical response of and damage mechanisms operating in the AM composite.

1.4 Methodology

The following tasks were carried out in order to achieve the objectives laid out above:

1. Perform monotonic load/unload tension tests at low (well below the elastic limit) load levels to determine the elastic modulus of each test specimen in order to assess specimen to specimen variability.
2. Perform tension-to-failure tests at 23 °C to determine the ultimate tensile strength and to characterize the tensile stress-strain behavior of both 0/90 and ±45 fiber orientations. Perform tension-to-failure test at 150 °C to measure the tensile properties of the 0/90 composite. Due to very limited supply of the test material, high-temperature tensile properties of the ±45 composite could not be measured. It is recommended that such measurements be carried out as part of a follow-on effort.
3. Perform tension-tension fatigue tests at a frequency of 1 Hz with an R ratio of minimum to maximum stress of 0.1. Fatigue run-out is defined as survival of 200,000 cycles. Fatigue tests of the 0/90 composite are carried out at 23 and 150 °C. Fatigue tests of the ±45 composite are limited to 23 °C due to short supply of the test material. All specimens that reach fatigue run-out are tested in tension to failure at the temperature of the fatigue test in order to measure the retained tensile properties.

4. Results of the monotonic tension and tension-tension fatigue tests obtained for the AM composite are compared with those obtained for a TM composite with similar constituents.
5. Examine failed specimens under an optical microscope to gain insight into failure mechanisms.
6. Perform X-Ray CT scanning of selected test specimens. Analyze the X-Ray CT images to elucidate the microstructural features of and damage mechanisms operating in the AM composite.

II. Background

2.1 Composite Materials

Composite materials are materials consisting of two or more separate phases combined in a single structural unit [2]. The goal of a composite material is to have better mechanical performance than each constituent phase operating independently by capitalizing on the strengths of each of the constituent phases. Humans have been using composites since ancient times by combining straw with mud to create bricks. Limited innovation was made in the area of composites until the 1900s when modern resins and fibers began to be discovered [2]. Fiber reinforced composites are the area of focus for this effort, specifically carbon fiber reinforced polymer matrix composites (CF-PMCs).

2.2 Polymer Matrix Composites

Carbon fiber reinforced polymer matrix composites (CF-PMCs) consist of two different phases: the fibers and the matrix. Matrix materials can be polymer, metal, or ceramic. In high-performance carbon fiber reinforced polymer matrix composites, the purpose of the polymer matrix is to protect and support the fibers and to provide the local load transfer between the fibers. The high strength, high modulus continuous carbon fibers are the backbone of the composite. The fibers determine the composite strength and stiffness in the on-axis of fiber direction. Taken independently, the fibers are not sufficiently rigid to be used in a structural application. Polymer matrix has much lower strength and stiffness than a typical engineering alloy. However, when reinforcing fibers are combined with a polymer matrix, we have a strong, lightweight material with an excellent strength-to-weight ratio, an important metric for aerospace applications. While engineering alloys typically have excellent strength properties, they are very

dense and have a considerably lower strength-to-weight ratio than the PMCs. Polymer matrix composites fill this need for a strong but lightweight material.

2.2.1 Polymer Matrices

Polymer matrix materials are divided into two broad categories: thermoplastics and thermosets. The choice of matrix material, or resin, is very important to the thermal properties of the polymer matrix composite. Thermoplastics are characterized by the ability of the polymer to dramatically soften or even melt at high temperatures, and re-solidify upon cooling. The source of this property lies in the polymer microstructure. Thermoplastics are composed of long molecular chains that are not connected through chemical bonds, but are held together predominantly through intermolecular forces. Conversely, in the case of the thermosets, the polymer chains are bound together via cross-linking. During curing, covalent bonds are formed linking molecular chains and creating a network of bonds. This process, known as cross-linking, prevents melting of thermosets. Thermoplastic polymer chains are able to slide past one another, but because thermoset polymer chains are bound together, their motion is heavily restricted. This restriction of motion leads to generally better mechanical properties at higher temperatures than those of the thermosets. Typically, thermosets are harder than thermoplastics, furthermore they exhibit better dimensional stability [3]. Thermosets are the matrix material of choice for most structural applications of CF-PMCs, including aerospace applications.

2.2.2 Reinforcing Fibers

The fibers used to reinforce composites can be constructed using many different materials. Table 1 displays a list of common fiber types and their advantages and disadvantages.

Table 1: Various fiber materials with their advantages and disadvantages [4]

Fiber	Advantages	Disadvantages
E-glass, S-glass	High strength Low cost	Low stiffness Short fatigue life High temperature sensitivity
Aramid (Kevlar)	High tensile strength Low density	Low compressive strength High moisture absorption
Boron	High stiffness High compressive strength	High cost
Carbon (AS4, T300, IM7)	High strength High stiffness	Moderately high cost
Graphite (GY-70, pitch)	Very high stiffness	Low strength High cost
Ceramic (Silicon carbide, alumina)	High stiffness High use temperature	Low strength High cost

Though there are many different types of fibers, glass and carbon fibers are the most commonly used in polymer matrix composites. Glass fibers are widely used in low to medium performance composites due to their high tensile strength and low cost, however they are not suited to high performance composites due to their low stiffness [4]. Carbon fibers are used in high performance composites, such as aerospace-grade composites.

2.2.3 Fiber Architectures

The strength of polymer matrix composite parts has just as much to do with the way the fibers are arranged within the matrix as it does the choice of the fiber material. A single fiber will be grouped with other single fibers to make a yarn, or tow [4]. A tow can be woven with other tows, or laid out unidirectionally to form a ply. Plies are then stacked to form a laminate. The order in which plies are stacked is termed the stacking sequence.

Each ply has a fiber direction associated with it. The angles in of the plies are measured counterclockwise from the intended load direction of the part. Stacking plies of multiple

directions upon one another is how the properties of the composite sheet are tailored. Plies can have more than one fiber direction if the fibers are woven together to form a fabric. Additionally, fibers can be continuous or discontinuous. Continuous fibers span the length of the part uninterrupted. Discontinuous fibers have breakages along the length of the fibers. This research effort will be conducted using a CF-PMC laminate consisting of unidirectional plies reinforced with continuous fibers. The research composite is fabricated using additive manufacturing (AM), a novel manufacturing method.

2.3 Polymer Matrix Composites - Traditional Manufacturing (TM)

Due to their excellent mechanical properties, CF-PMCs have many advantages over other classes of materials. However, one of their chief drawbacks is the cost of producing CF-PMC parts. This high cost can be traced back to the manufacturing process of this material. It is very energy intensive and requires the hands-on labor of many skilled workers. Because this research investigates CF-PMC with a thermosetting resin as the matrix material, the traditional manufacturing process for CF-PMCs with thermosetting matrix materials will be the only one outlined herein. Additionally, autoclave molding will be the process outlined as it is the method used for fabricating parts with the highest performance requirements [4].

Life of a composite part begins as what is known as “prepreg”. Unidirectional or woven fiber layers are preimpregnated with partially cured resin. At this stage the ratio of fibers to matrix, ply thickness, and other qualities are adjusted to meet the customer’s specifications [4]. The prepreg is then collected in rolls and shipped to the customer. This process is automated and does not require the intervention of skilled workers, and is thus not cost-prohibitive. The end product of this process, i. e. the prepreg, is one of the elements that drives up the cost of CF-PMC parts. Prepreg is a partially cured product, and thus must be kept at very low temperatures

in order to prevent it from curing prematurely. Prepreg is typically stored at -18 °C (0 °F) in order to halt curing, and even then, it still has a limited shelf life [4]. Refrigeration is a very power intensive process. It is very expensive to store large amounts of prepreg, as the larger the volume that needs to be refrigerated, the higher the refrigeration costs. Storage of prepreg is one of the high-cost elements of CF-PMCs fabrication. Additionally, if the prepreg is not used before its shelf life elapses, the manufacturer does not guarantee that it will meet the mechanical specifications the customer ordered. Hence there is a high potential for waste, which further drives up the cost of manufacturing composite parts.

Once a part geometry is designed by engineers, the mold, or tool, needs to be produced. This tool is typically a large metal block machined with a very high degree of precision. The prepreg is laid on top of the mold in order for the part to take its shape. Skilled workers will carefully hand-lay plies upon the tool in the desired stacking sequence. Then a vacuum bag will be placed around the part in order to compact the plies, but also to get rid of any gases produced in the curing process, thus reducing void volume [4]. Because this process is not automated, it takes considerable time to produce parts on a large scale. The labor and time factors of this step further drive up the cost of CF-PMCs parts.

The final step in production is the curing of the part in an autoclave. The vacuum sealed part is enclosed in an autoclave at elevated temperature for the duration of the curing process. During autoclave curing, the ambient temperature and pressure can be modulated to suit the cure process along with the time spent in the autoclave. Each cure process is unique to the resin system used in the part, as well as the size of the part. Holding temperatures in excess of 150 °C for 5 - 24 hours is very costly, especially for large volume parts. In order to manufacture the wings of the 777X, Boeing utilize an autoclave that is 28 feet in diameter by 120 feet long. This

is an enormous volume of space to utilize as an autoclave [5]. Operating an autoclave of this size uses tremendous amounts of power. Not only is an autoclave an oven, but it is also a sealed pressure vessel as it is necessary to ensure that the pressure remains appropriate for the curing part. Not only must temperature and pressure be controlled, but airflow over the part is crucial to ensuring a uniform temperature gradient while curing.

Once all of these steps are complete, the part is inspected and used in manufacturing the component. While this method creates high quality parts, it is very inflexible. Autoclave molding thrives when used for parts with steady demand and well-defined geometries. Due to the numerous and time-consuming steps involved, a large amount of lead time is required. Sharp increases or decreases in demand are the enemy of autoclave molding. The manufacturer only has so many autoclaves, and curing can only happen at a certain rate. Conversely, if demand drops, the manufacturer risks being left with waste in the form of expired prepreg. Due to the inherent cost associated with this method, it stifles innovation. Manufacturers are loath to change part geometries, as that requires the fabrication of all-new tooling and cure procedures. A minor design tweak can oftentimes cost more money and man-hours than manufacturers are willing to spend. The high cost and low flexibility associated with traditional CF-PMC fabrication has led to exploring novel fabrication techniques, such as additive manufacturing.

2.4 Polymer Matrix Composites - Novel Manufacturing Method

A novel manufacturing method developed by the company Continuous Composites® seeks to change the way CF-PMCs are produced in the future. This process involves the use of additive manufacturing and a photocuring thermoset resin. This process is fundamentally different from autoclave molding. This novel manufacturing process does not require a prepreg, special tooling or bagging of finished parts. Furthermore, this process is automated.

Additive manufacturing (AM) of is not a new idea when it comes to composite manufacturing. Additive manufacturing of thermoplastic carbon fiber reinforced composites has been researched for some years [6]. The AM process utilizes essentially the same setup as a traditional desktop polymer 3D printer that can be purchased for home use. Figure 1 shows a diagram of a nozzle system that is used in the printing of CF-PMCs with a thermoplastic matrix.

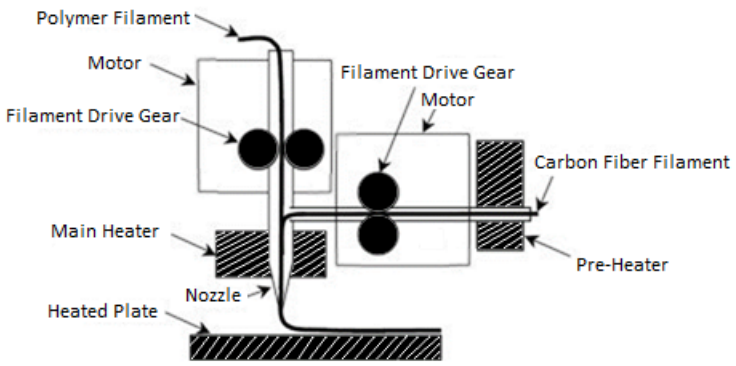

Figure 1. A system that prints composite parts with a thermoplastic matrix material.

The process shown in Figure 1 is essentially the same process as that used in a desktop polymer 3D printer except for the added carbon fiber extruder perpendicular to the polymer filament. Simultaneously, a polymer filament and a carbon fiber are drawn together in a heater, then extruded through a nozzle. This combination is then deposited onto a heated table where the polymer solidifies, and the nozzle is moved across the table in order to achieve the desired part geometry [7].

Parts manufactured using thermoplastic matrix composites have lesser mechanical properties than the thermoset matrix composites. Up to now, thermoset resins had not been considered for use in additive manufacturing. Thermoset resins are liquid before they cure, and

curing takes time. If a thermoset resin were extruded using the setup shown in Figure 1, the process would fail. Liquid resin would spill everywhere, and a structurally useful composite part would not be made. To overcome this hurdle, Continuous Composites® have developed a proprietary resin system that cures instantly when exposed to UV radiation. This innovation allows the fiber to be continuously impregnated and extruded, and cured right on the print bed as the nozzle passes. Figure 2 is a diagram of the system utilized by Continuous Composites® to additively manufacture polymer matrix composites (AM-PMCs).

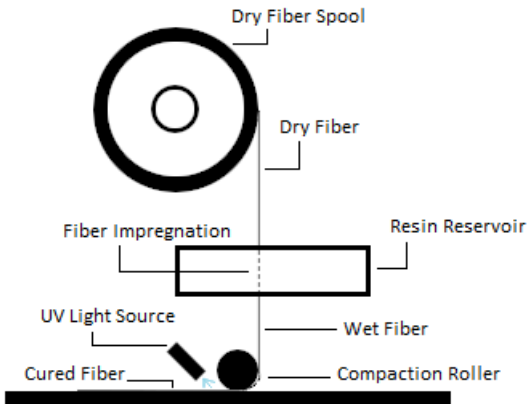

Figure 2. The print system used by Continuous Composites®

As seen in Figure 2, dry fiber is drawn through a resin reservoir, impregnating it with resin. Wet fiber is spooled onto a compaction roller, and instantly, or "snap", cured by a UV radiation source. While the UV curing is not a complete curing, it is just enough to keep the part geometry rigid. The printed part still needs to go into an oven for the curing to be finished off thermally. This process is altogether different from autoclave curing. The finished part is simply placed in a basic industrial oven, not an autoclave. Pressure does not need to be controlled, and vacuum bags are not required. It is much less costly to operate a simple oven rather than a sensitive autoclave.

The potential advantages of this method are many. This process gives engineers the ability to design much more freely. With autoclave molding, designers are limited to geometries achievable by stacking 2D plies on top of one another. With additive manufacturing, that is not the case. New, varied, and complex geometries can be produced that could not be produced using traditional methods. There is virtually no lead time when producing parts. The only bottleneck is the number of printers the manufacturer owns. The iterative design process can occur much more rapidly, as small design tweaks do not require an entirely new tool to be produced. Material waste is kept to a minimum, as production can smoothly scale with demand. If demand drops, the manufacturer can simply slow the production of parts without worrying about prepreg expiring.

Before all of these potential benefits can be realized, however, much work needs to be done investigating the mechanical properties and performance of the composite fabricated via this novel method. This is an entirely new material system produced via an entirely new production method. It is unknown how the new, proprietary resin system as well as the new production method will affect the mechanical behavior of this material.

2.5 Mechanical Behavior of Polymer Matrix Composites

This effort aims to characterize the basic mechanical properties and tension-tension fatigue behavior of this novel AM-PMC with the [0/90] and [±45] fiber orientations at 23 °C and 150 °C.

2.5.1 Tensile Behavior

Monotonic tension test to failure is the most fundamental experiment that must be performed when a new structural material is introduced. Critical data obtained in a tensile test is used to generate basic tensile properties, such as elastic modulus and ultimate tensile strength

and a tensile stress-strain curve. Figure 3 shows a representative stress-strain curve for a 0/90 polymer matrix composite, as well the stress-strain curves for its separate phases [8]. As can be seen from Figure 3, each phase behaves differently, and the composite response lies somewhere between the responses of its phases.

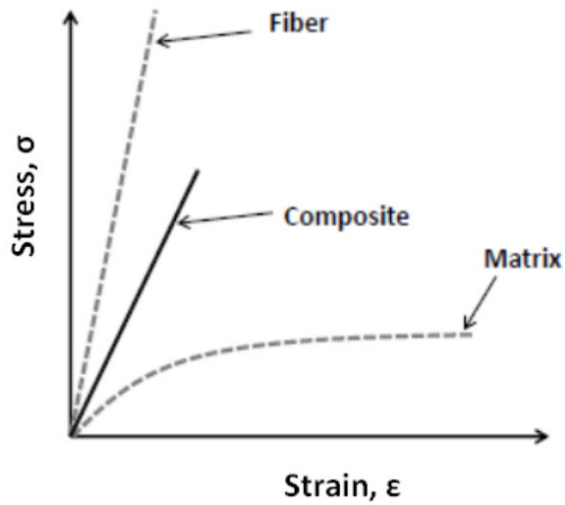

Figure 3. A representative stress strain curve for a polymer matrix composite and its separate phases [8].

A stress-strain curve plots the engineering stress (σ) vs. the engineering strain (ε). A stress-strain plot can also be used to determine the modulus of elasticity (E) of the tested material. The modulus of elasticity is a measure of the stiffness of a material, and is defined as the slope of the linear portion of the stress-strain curve. Another fundamental property that can be determined from a stress-strain curve is ultimate tensile strength (UTS), defined as the highest stress reached during a tensile test.

2.5.2 Fatigue Behavior

Once the UTS of a material has been determined, fatigue testing can commence. Fatigue testing involves cyclically loading and unloading a test specimen and recording the number of

cycles to failure. The UTS must be known in order to decide on the maximum fatigue stress levels and to develop the fatigue test matrix. This research effort explored tension-tension fatigue performance of the AM composite. Hence cyclic fatigue tests were performed with the R (ratio of minimum to maximum stress) of 0.1. Once a series of cyclic fatigue tests with various levels of maximum stress is completed, the data is presented as a maximum stress vs. cycles to failure (S-N) curve. A schematic depicting typical S-N fatigue curves is shown in Figure 4 [8], where the maximum stress in cycle is plotted vs. the number of cycles to failure.

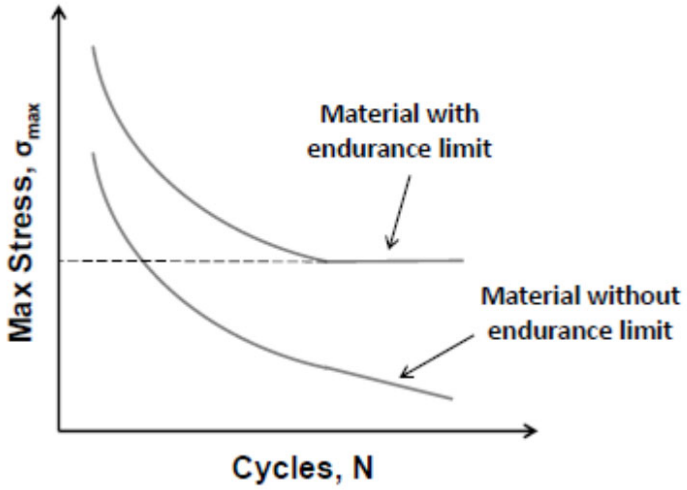

Figure 4. A notional S-N curve [8].

An endurance limit seen in Figure 4 is a horizontal asymptote of an S-N curve. By definition, the material will not fail if cycled with the maximum stress at or below the endurance limit.

2.5.3 Temperature Effects

Temperature affects both the tensile properties and the fatigue behavior of a polymer matrix composite. Elevated temperature can soften the matrix, as well as the fibers, although to a lesser extent. This softening of the material will tend to "shift" the S-N curve. Figure 5, where

strain is plotted vs. cycles to failure, displays the general effects of softening or stiffening of the components of a composite upon the S-N curve [9].

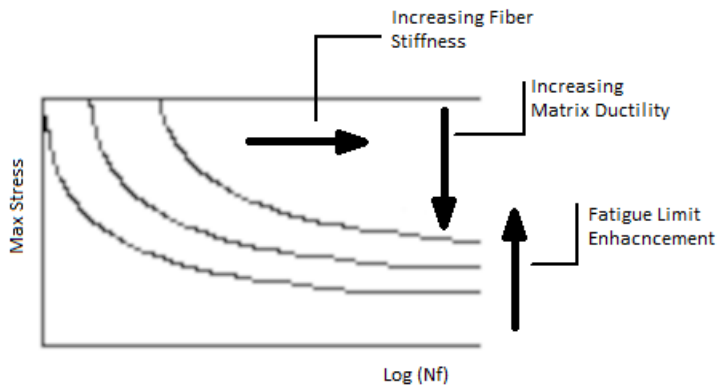

Figure 5. A schematic showing the effects of the stiffness of the phases of a polymer matrix composite on the shift of the composite's S-N curve.

Because elevated temperature softens both the matrix and the fibers, it is expected that an S-N curve generated for a composite will shift down and to the left, resulting in a lower fatigue life.

2.6 Previous Research

2.6.1 Additively Manufactured Polymer Matrix Composites

This additively manufactured material system is aiming and replace the standard commercial off the shelf carbon fiber reinforced composite parts. At present, the mechanical behavior of the traditionally manufactured carbon fiber composites (TM-PMCs) is well documented and understood. Even after more than 70 years of researching and using structural PMCs, fabrication cost is the largest barrier to their widespread insertion into structural applications. When 3D printing became a mainstream topic of research, it did not take long for composites researches to use the new technology. The first efforts at printing fiber reinforced

composites used thermoplastic matrix materials. Such printing is called fused filament fabrication [10]. In a study that investigated the use of such a manufacturing method, Tekinalp et al. were able to make thermoplastic parts with considerably high tensile strength and elastic modulus, ranging from 30-65 MPa UTS and 2-14 GPa elastic modulus as fiber loading increased from 0 to 40% [11].

The matrix material represented in this studyis ABS - a polymer made with three different monomers: acrylonitrile, butadiene, and styrene. Whereas the strength of the ABS-matrix composites can be enhanced by adding more carbon fibers, their thermal performance will still be lacking. The ABS resin has a low glass transition temperature of 105 °C. A glass transition temperature is the temperature at which long-range motion of polymer chains is no longer inhibited by the natural entanglement of the polymer chains. At the glass transition temperature, the polymer has not melted, but it is no longer capable of carrying any useful load for structural purposes.

Thermosetting polymers have a much better high-temperature performance than the thermoplastic polymers. That is why the thermosetting resins are the matrix material of choice for the vast majority of the PMCs. To address the behaviors specific to thermosets, researchers were seeking ways to make a liquid resin harden instantaneously, yet in a controlled manner, after leaving the print head. Such procedures were termed “out of autoclave” curing procedures. One recently proposed method is called “frontal polymerization”. This method involves a self-propagating exothermic reaction wave that transforms liquid monomers into solid polymer instantaneously as it is being printed [12]. The heat generated by the curing process itself is fuel for the curing process to continue. These resins must be very specific, however. Continuous Composites proposed to use UV photocuring. In 2016, a group of researchers developed and

tested a photocured resin, then fabricated test specimens using this resin. The unidirectional composite specimens were also fabricated using the photocured resin. The neat resin (unfilled) specimens and the unidirectional composite specimens were tested in tension to failure at room temperature [13]. Tensile properties obtained in these tests are summarized in Table 2.

Table 2: Average values (±standard deviation) of elastic modulus, maximum tensile strength and elongation at break for unfilled (B33 and B50) and fiber-reinforced (B33G5 and B50C5) composite materials. The mechanical properties of CFR composites containing sized

Property	B33	B50	B33G5	B50C5	B50C5-S
Elastic modulus E' (GPa)	2.6±0.7	2.7±0.4	3.5±0.3	3.9±0.9	4.4±0.9
Maximum tensile strength (MPa)	35.1±8.9	16.0±2.9	41.7±5.1	30.6±5.9	33.8±4.9
Elongation at break (%)	1.8±0.7	0.6±0.2	1.6±0.1	0.9±0.2	1.0±0.2

These results were the first of their kind at the time. This material was very far from being usable in a structural application, but was novel in its use of a thermosetting resin. This resin is the precursor to the material that Continuous Composites has developed.

III. Materials and Test Specimens

3.1 Novel Additivity Manufactured Polymer Matrix Composite

The material of investigation for this research effort is a novel additively manufactured polymer matrix composite (AM-PMC) developed and fabricated by Continuous Composites®. The reinforcing carbon fibers were T1100 fibers produced by Toray®. The resin system utilized by Continuous Composites® is a proprietary acrylic-based system produced by Sartomer®. This resin cures instantly when exposed to UV radiation. Due to the proprietary nature of the resin, only limited information is available regarding the resin composition (Table 3).

Table 3: Safety data sheet of the resin used in the research material [14].

Chemical Name	CAS-No.	GHS Classification
Acrylic Ester	Proprietary	H317, H411
Trifunctional acrylate monomer	Proprietary	H318, H317, H412
Tricyclodecane dimethanol dimethacrylate	43048-08-4	H317, H411
Peroxyesters	Proprietary	H242, H332, H315, H317, H400, H412
Phenyl bis(2, 4, 6-trimethylbenzoyl)- phosphine oxide	162881-26-7	H317, H413

Three composite panels were supplied for this effort. Two panels had the 0/90 fiber orientation, while one panel had the ±45 fiber orientation. Panel information provided by Continuous Composites® is summarized in Table 4 [14].

Table 4: Composite panel data provided by the manufacturer [14].

Quantity	Description	Fiber	Resin	Targeted Fiber Volume Fraction	Targeted Void Volume Fraction
2	(0/90) – 1' x 1' x 2.5 mm	T1100 – 12K	GF2.4	40%	<2%
1	±45 – 1' x 1' x 2.5 mm	T1100 – 12K	GF2.4	40%	<2%

3.2 Specimen Geometry

Standard dogbone-shaped tensile specimens (Figure 6) were used in all tests. This specimen geometry ensures that failure occurs within the specimen gauge section.

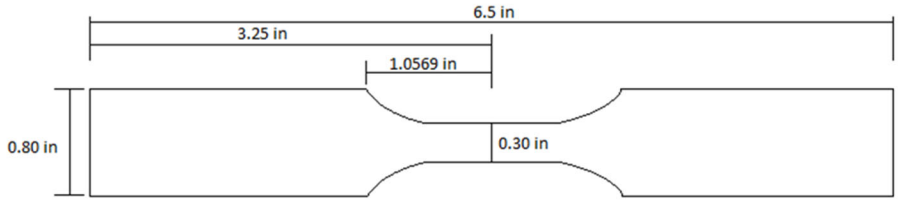

Figure 6. Standard dogbone-shaped tensile specimen.

3.3 Specimen Preparation

Specimens were cut from the as-received panels by the AFIT Model and Fabrication Shop via diamond grinding. Three panels were supplied for this research effort. The panels were labeled 306, 313, and 314. Panels 306 and 313 had the 0/90 fiber orientation, and panel 314 had the ±45 fiber orientation. In total 56 specimens were cut from the three panels. Table 5 shows specimen count and labeling convention for each panel.

Table 5: General Specimen Information

Panel No.	Fiber Orientation	Example Specimen Label	Number of Specimens
306	0/90	306-1	19
313	0/90	313-1	19
314	±45	314-1	18

The dimensions of the specimens were measured using Mitutoyo Absolute Solar Digimatic Caliper, Model N0. CD-S6-CT. Gauge section width and thickness were measured in order to determine the cross-sectional area of each specimen. Table 6 presents average specimen thickness, width and cross-sectional area for each composite panel.

Table 6: A summary of the measurements of each specimen from each panel.

Panel No.	Average Specimen Width (mm)	Average Specimen Thickness (mm)	Average Specimen Cross Sectional Area (mm^2)
306	7.651	2.622	20.063
313	7.638	2.619	20.013
314	7.685	2.581	19.836

Each specimen was washed using household soap and water to remove any contaminants left over from the machining process. Washed specimens were first dried with paper towel, then dried in a vacuum oven at 80 °C at a pressure of 4 in Hg to expel the absorbed moisture. Three specimens from each panel were taken out and weighed periodically using a Mettler Toledo balance accurate to ±0.9 mg. Figure 7 shows average percent weight loss vs. time for each composite panel. Once the weight loss approached the asymptotic solution, the specimens were considered dry and ready for testing. The specimens were removed from the oven and stored at

room temperature in a desiccator maintained at ~15% relative humidity in order to minimize moisture reabsorption from laboratory air.

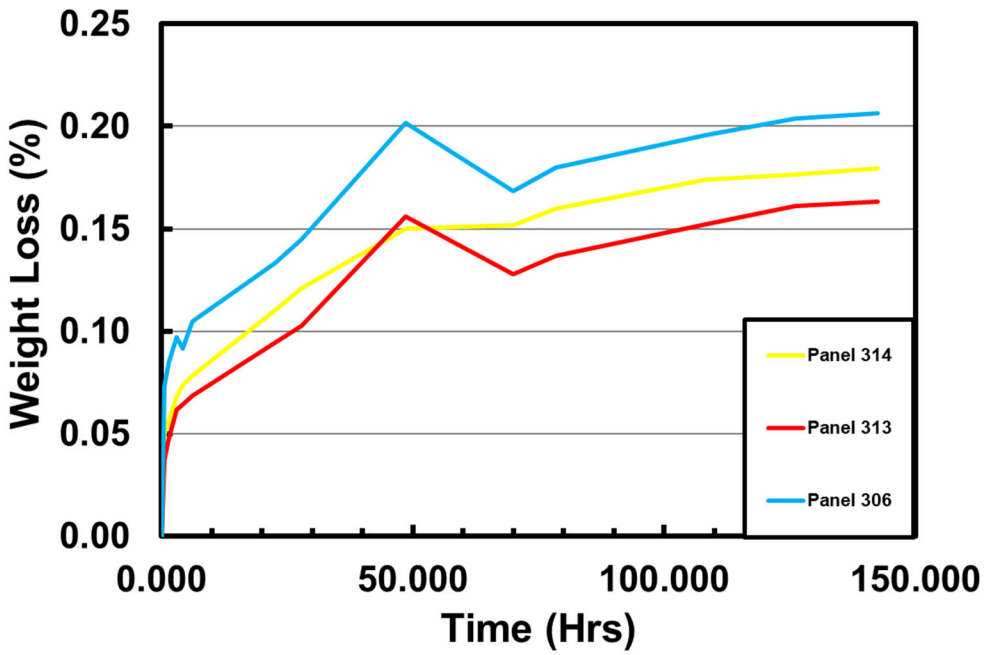

Figure 7. Average percent weight loss vs. time for each composite panel.

Fiberglass tabs were bonded to the gripping sections of each specimen in order to prevent damage from the wedge grips of the testing machine. The VPG Micro Measurements M-Bond 200 adhesive, an all-in-one, room temperature curing epoxy was use to bond the tabs to the specimens.

For tests requiring the use of an MTS low-contact force elevated temperature extensometer, indentations had to be made in one side of the specimen. Specimens were indented using a punch tool manufactured by MTS and a small hammer. Indentations were made using the least force possible to ensure that the specimen would not experience diminished fatigue life due

to the indentations while also ensuring that the extensometer maintained uninterrupted contact with the specimen.

IV. Experimental Setup and Testing Procedures

4.1 Testing Equipment

Mechanical testing was split amongst three different load frames. Load frame number one was a vertically configured model 810 MTS servo-hydraulic testing machine outfitted with a 100 kN model 647.10A load cell, an MTS model 661.20E-03 force transducer, a 100 kN MTS model 609.10A-01 alignment fixture, and MTS model 647.10 wedge grips. Room temperature modulus testing, along with roughly half of the room temperature fatigue testing was performed on this load frame. Load frame number one utilized an MTS model 632.26F-20 extensometer with knife-edge contacts.

Load frame number two was a vertically configured model 810 MTS servo-hydraulic testing machine outfitted with an MTS model 661.20E-03 force transducer, a 100 kN MTS model 609.10A-01 alignment fixture, and MTS model 647.10 wedge grips. The other half of room temperature fatigue testing was performed on this load frame. This load frame was equipped for high temperature testing, and roughly half of the high temperature work occurred on this load frame. This load frame was equipped with an MTS model 653.01A furnace system, as well as an MTS model 632.53E-14 high temperature extensometer with silica rods.

Load frame number three was a vertically configured model 810 MTS servo-hydraulic testing machine outfitted with an MTS model 661.19E-04 force transducer, a 100 kN MTS model 609.02A-01 alignment fixture, and MTS model 647.02B-03 wedge grips. This load frame was equipped for high temperature testing as well, and the other half of the high temperature work occurred on this load frame. This load frame was equipped with an AMTECO model HRF5-350-27-2700 furnace system, as well as an MTS model 632.53E-14 high temperature extensometer with single crystal silica rods.

All load frames utilized a FlexTest 40 digital controller was used for controlling input signals and acquiring data. All testing utilized the MTS station manager, running a configuration file created under MTS building release 5.2B. All testing procedures were creating on the MTS station manager, allowing for automated testing under all test conditions. Figure 8 displays all testing equipment used.

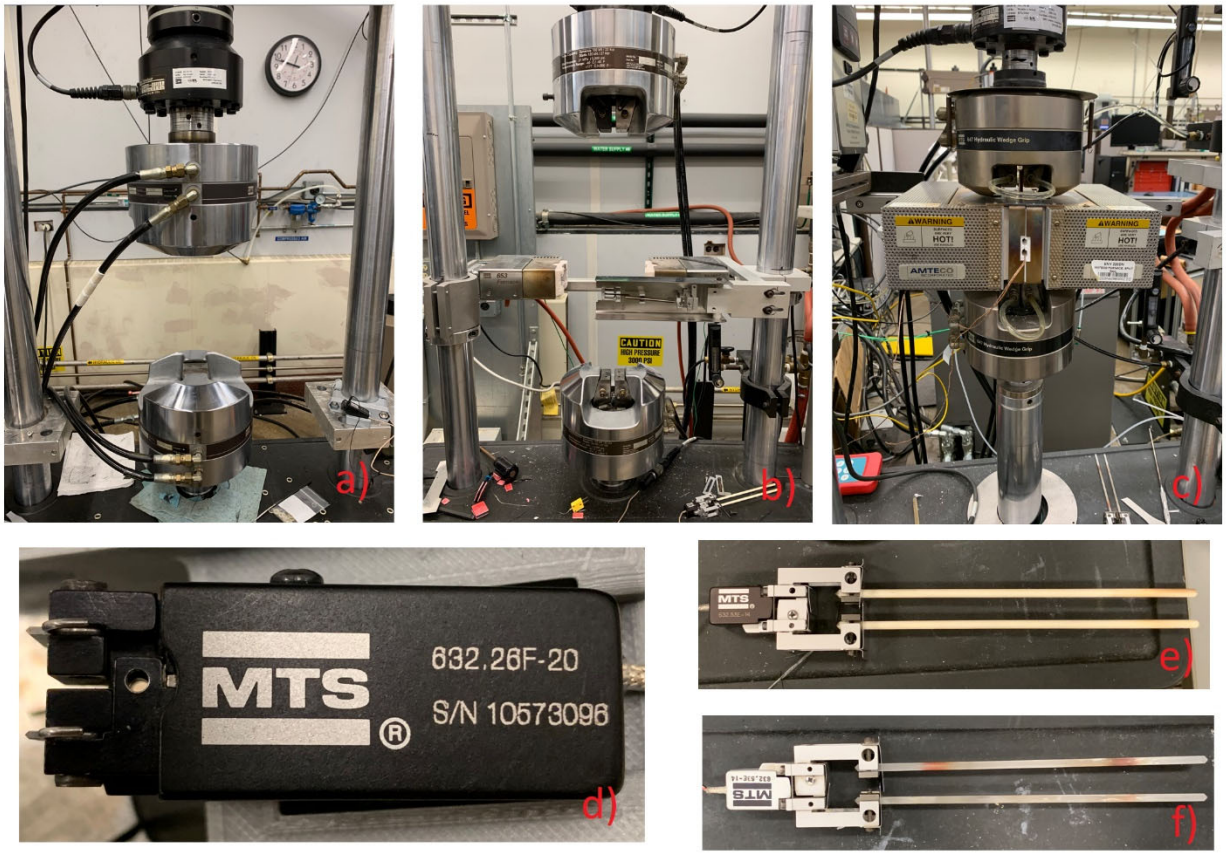

Figure 8. Equipment shown is a) station #1, b) station #2, c) station #3, d) room temperature knife edge extensometer, e) silica rod high temperature extensometer, f) single crystal silica high temperature extensometer

4.2 Tuning of Testing Equipment

The load frame controllers can be operated primarily in three different modes: displacement control, force control, and strain control. During this testing, only force and displacement control were utilized. During the tension to failure portion of the research, it was uncovered that the load frames were out of tune for this material when the load frames were operated in displacement control. Unusual perturbations in the tension to failure specimen's stress strain curves prompted further investigation. When one of the 0/90 specimen's displacement and displacement command was graphed against time, the problem was revealed. Figure 9 shows the graph of specimen 313-1 that revealed the issue.

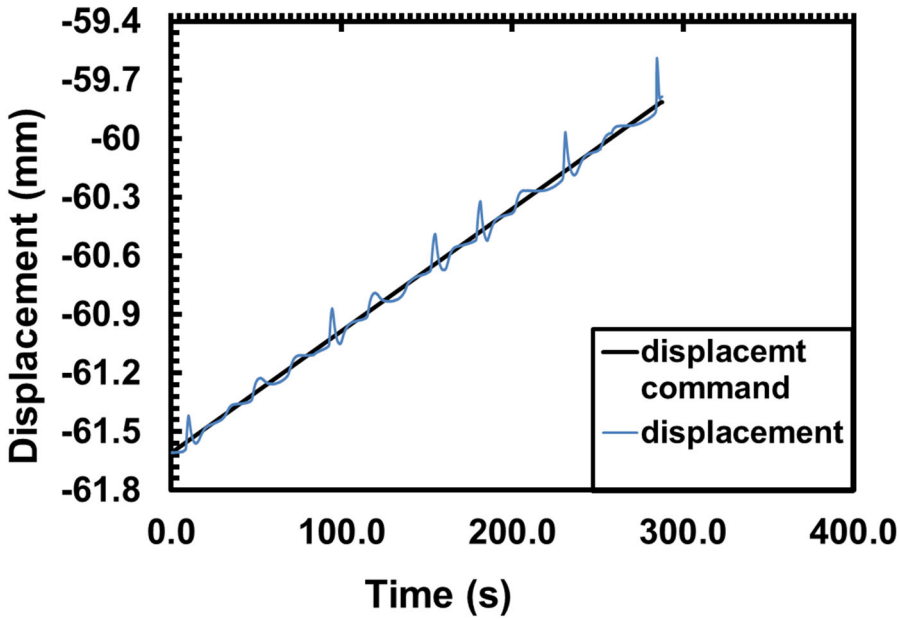

Figure 9. Displacement and displacement command versus time for specimen 313-1. Note that displacement is on an absolute scale

Figure 10 shows the displacement command versus the displacement response of the load frame actuator graphed against time for station one when no specimen was loaded. Due to the regular,

periodic nature of the displacement response failing to follow the displacement command, it can be concluded that the load frame was out of tune.

The tuning of the MTS Flex Test 40 digital controller needed to be adjusted for displacement control. Tuning the controller consists of having the load frame perform some form of action, while adjusting the gains of the controller withing the station manager. For tuning displacement control, the load frame is commanded to move the actuator between a given displacement range in a periodic fashion. This movement is not sinusoidal; however, it is a square wave. Square waves cause very drastic, quick movements. The logic behind tuning square waves is that if the load frame can perform this abrupt motion perfectly, it should be able to perform gentler actions even more so.

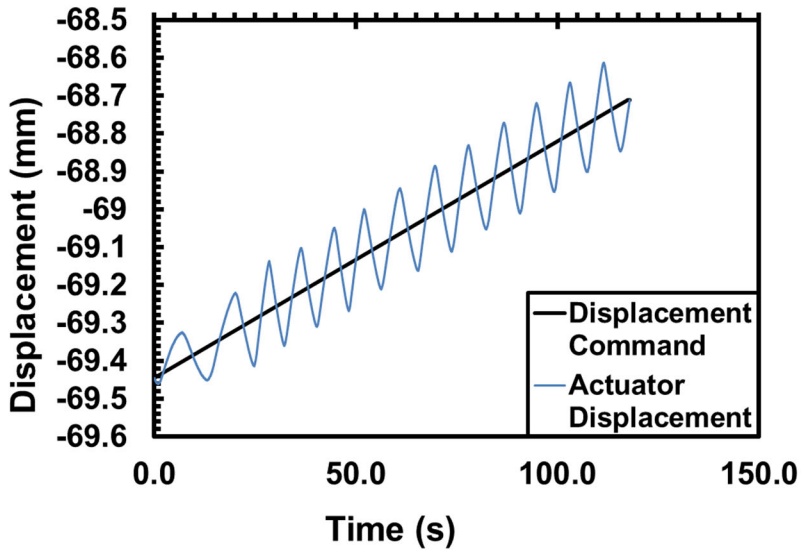

Figure 10. Displacement and displacement command versus time for station one. Note that displacement is on an absolute scale.

The tuning procedure per the MTS user manual is first to place the software in tuning mode by selecting “tuning” as the operator. Next access the function generator and input the following settings per Table 7.

Table 7: The settings for tuning displacement control

Control	**Setting**
Wave Shape	Square
Frequency	1 Hz
Target Setpoint	0 mm
Amplitude	10% of full scale

Next set up the scope to view displacement and displacement command on the same scale. Then observe the displacement and displacement command to see how closely the displacement matches the displacement command. Figure 11 is the graphic that MTS provides to show what proper tuning looks like.

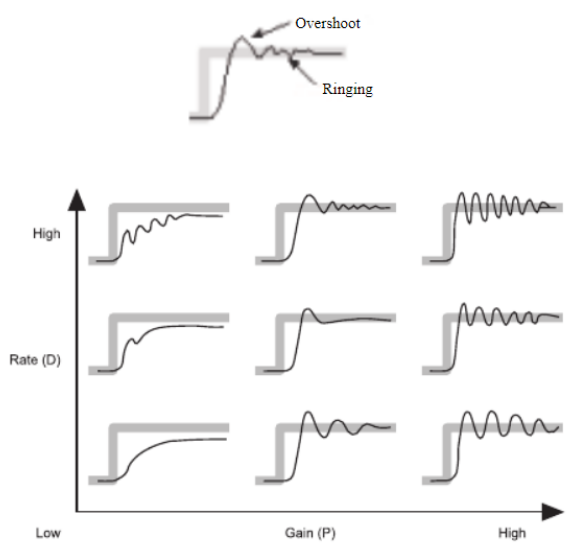

Figure 11. Range of tuning responses when P gain is plotted against D gain [15]

The only action left is to adjust the various gains to observe the response. The gains are labeled P, I, D, and F gain. F gain was not adjusted for this effort, and it remained at zero. D gain was also not adjusted as it did not have any apparent effect on the displacement response waveform. It remained as it was found in the tuning file with a value of 0.26588. P gain is a proportional response gain, and directly affects the error between the response and the command. I gain is an integral response, and it affects the error response over the time history of the command. P and I gains were greatly increased from 10 and 5 respectively, to 95 and 40 respectively. As a general rule of thumb, I gain should be 50% of P gain, but in this case an I gain of 40 gave the best results.

The poor tuning was only discovered after three of each fiber orientation for room temperature were tested. Due to a lack of specimens, only one more test was carried out to ensure that the UTS was within the bounds of the tests that had already been conducted, as UTS is the most important property to take away from tension to failure tests when preparing to perform tension-tension fatigue tests. In both cases, the fourth tension to failure test had a UTS that matched with the tests already performed, leading to the conclusion that the poor tuning did not affect the average UTS.

4.3 Mechanical Testing Procedures

4.3.1 Room Temperature Elastic Modulus Measurements

Elastic modulus measurements occurred before any other mechanical testing. Measuring the elastic modules of each specimen established specimen to specimen variability, as well as panel to panel variability. For the 0/90 specimens, each specimen was loaded to 20 MPa and unloaded back to 0 MPa three times. Each cycle lasted 20 seconds. Performing three cycles ensured an average could be accurately determined. Determination of the elastic modulus was

performed via line of best fit. For the ±45 specimens, the procedure was identical except the max load was limited to 10 MPa to ensure a linear material response, and that the specimens weren't damaged prematurely. A grip pressure of 5 MPa was used for this series of testing.

4.3.2 Monotonic Tensile Tests

Tension to failure tests were carried out at room temperature and also at 150 °C. Tension to failure testing established a UTS for use later in fatigue testing. Both 0/90 and ±45 fiber orientations were tested at room temperature; however, due to the limited quantity of ±45 specimens, elevated temperature testing for this fiber orientation was not carried out. 4 specimens were consumed for each fiber orientation and at each temperature regime. This ensured that a statistically relevant UTS value could be generated. A grip pressure of 15 MPa was used for this series of tests.

The procedure consisted of loading a specimen via displacement control at a rate of 0.00625 mm/s until failure. Failure was marked by a sudden decrease in load carried by the specimen, followed by a load rate of zero. For elevated temperature testing, the procedure was identical aside from two preceding steps. The furnace temperature was raised to the proper setpoint over a 25 minute period. The temperature was allowed to equilibrate for 60 minute period. Following these two steps, the procedure proceeds identical to room temperature.

4.3.3 Tension-Tension Fatigue Tests

For all testing temperatures and fiber orientations, tension-tension fatigue testing occurred with a maximum stress ratio of R = 0.1 and frequency of 1 Hz. The UTS values from the tension to failure tests were averaged. Various percentages of that UTS were used as the maximum load levels for each test. The runout condition was set to be 200,000 cycles. If a

specimen lasted all 200,000 cycles, a tension to failure test was carried out using the same process as already outlined above.

During the tension-tension fatigue tests, the maximum and minimum load for each cycle was recorded. Also recorded was the full loading history of the following range of cycles:

- The first 26 cycles
- Every 10th cycle from 30-100 cycles
- Every 100th cycle from 100-1,000 cycles
- Every $1{,}000^{th}$ cycle from 1,000-10,000 cycles
- Every $10{,}000^{th}$ cycle from 10,000-200,000 cycles

4.4 Optical Microscopy

Optical microscopy was carried out on a Zeiss SteREO Discovery V12 stereoscopic optical microscope with a Zeiss SYCOP 3 control panel and a Zeiss EMS 3 controller. The control software used was the Zeiss ZEN Core V2.7 software. Micrographs were taken at a magnification level of 8 times magnification. The microscope and peripheries are shown in Figure 12.

Figure 12. The optical microscope used to take optical micrographs [16]

4.5 X-Ray Computed Tomography

X-Ray Computed Tomography (CT) images were collected by Dr. Jevan Furmanski at AFRL/RXCC to assist in understanding this material and its behavior on a deeper level. The unique nature of the additive manufacturing process necessitated this data collection as it creates a unique and uninvestigated microstructure that makes direct comparisons with TM-PMCs difficult.

X-Ray CT images were collected on a Zeiss Xradia 620 Versa 3D X-Ray Microscope. The resolution of the images collected for this effort were 20-micron voxels. Data and image processing was performed on Dragonfly Pro Workstation (Version 2021.3 Build 1087) software. The X-Ray CT is shown in Figure 13.

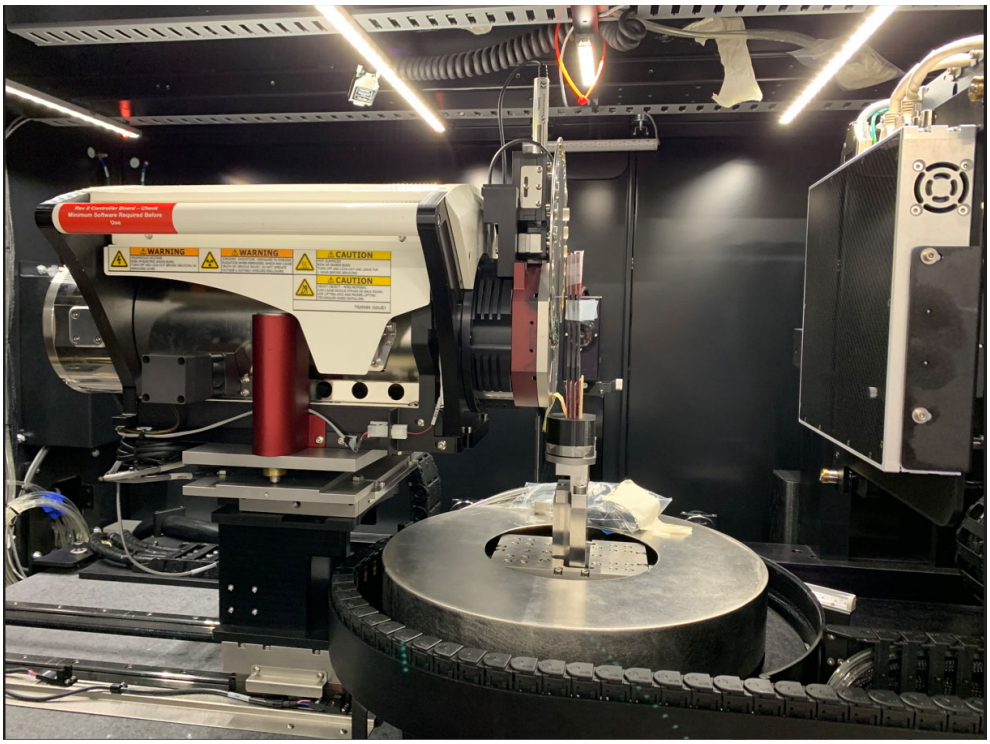

Figure 13. The X-Ray CT used for this effort with specimens installed for scanning

V. Experimental Results and Discussion

5.1 Assessment of Specimen-to-Specimen Variability

Due to the novel nature of this material and its manufacturing process, variability between panels and specimens in excess of what one would normally expect from aerospace-grade carbon fiber reinforced composites was expected. This variability stems from internal defects within the specimens, as well as slight dimensional differences in each specimen following the machining process. The metric used to assess specimen-to-specimen variability was elastic modulus. Section 4.3.1 outlines the process that was used for measuring the elastic modulus of each specimen. A line of best fit was used to assess the data gathered from the modulus tests, and the results are compiled in Table 8. Figure 14 shows a direct comparison of the elastic modulus values obtained for panels 306 and 313.

Table 8: Room temperature elastic modulus test results

Panel	Fiber Orientation	Average Modulus (GPa)	Standard Deviation (GPa)	Coeff. Of Variation
306	0/90	80.01	10.26	12.82
313	0/90	80.48	4.44	5.52
314	±45	16.36	3.45	21.09

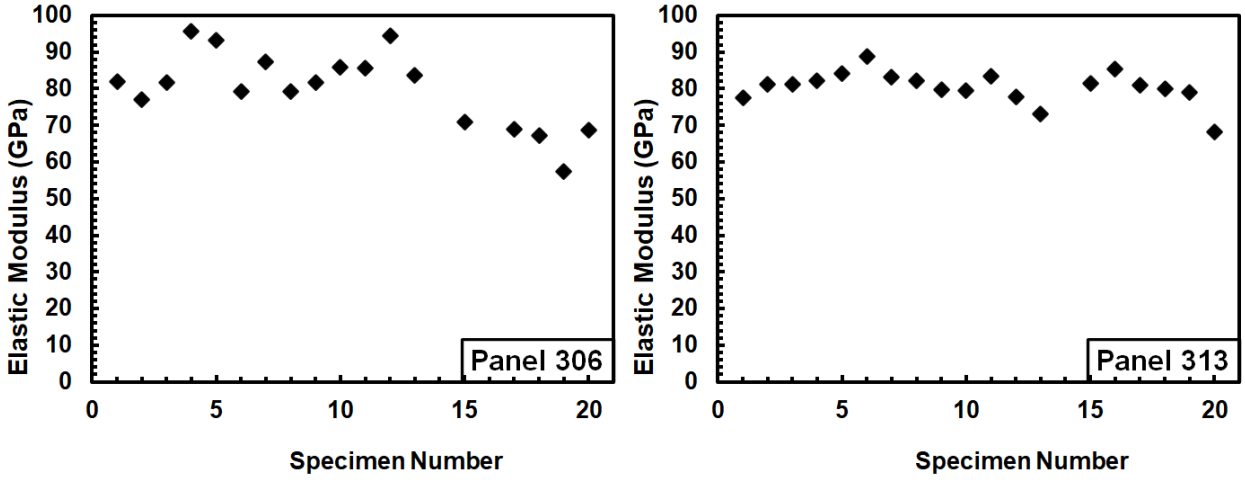

Figure 14. Modulus values for each specimen in panels 306 and 313

Of note are the average modulus values of the two 0/90 panels. The average modulus values obtained for panels 306 and 313 are nearly identical. However, the modulus data obtained for panel 306 have a much higher coefficient of variation as seen in Table 8. Modulus values obtained for specimens in panel 306 exhibit considerably more scatter than those obtained for specimens in panel 313 (Figure 14). Note that these two panels were fabricated using the same manufacturing process. Initial modulus values obtained for specimens in panel 306 are further examined in Figure C. Data points in Figure 15 can be organized into two distinct groups. Specimens 1-13 produced markedly higher initial modulus values than specimens 15-20. To gain further insight into the phenomena behind the discrepancy in the initial modulus values obtained for specimens 1-13 and those obtained for specimens 15-20, we examine the specimen cutting plan for panel 306 (Figure 16).

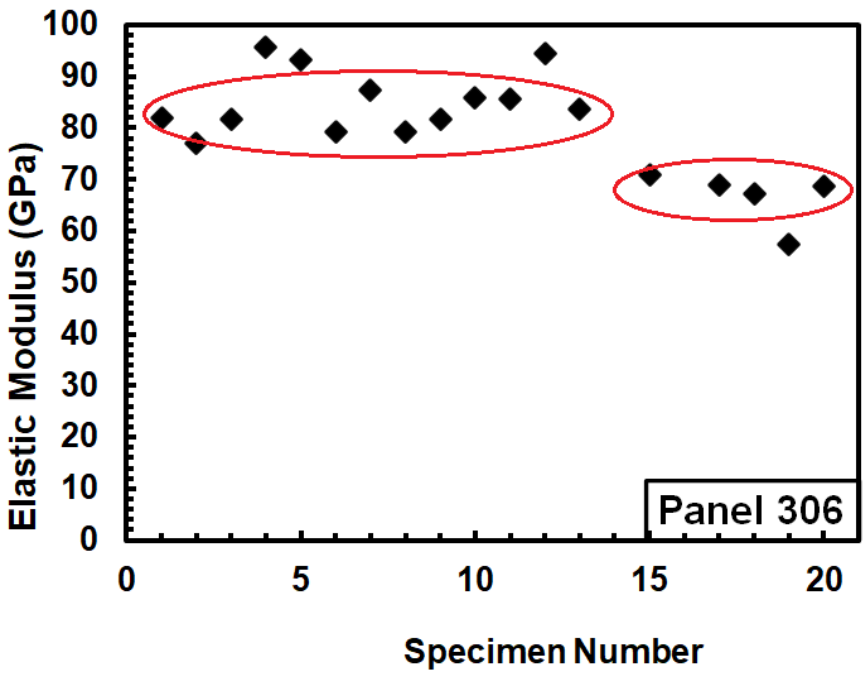

Figure 15. The two groupings of modulus values obtained for specimens in panel 306. One grouping occurs at the 85 GPa level, and the other at the 70 GPa level.

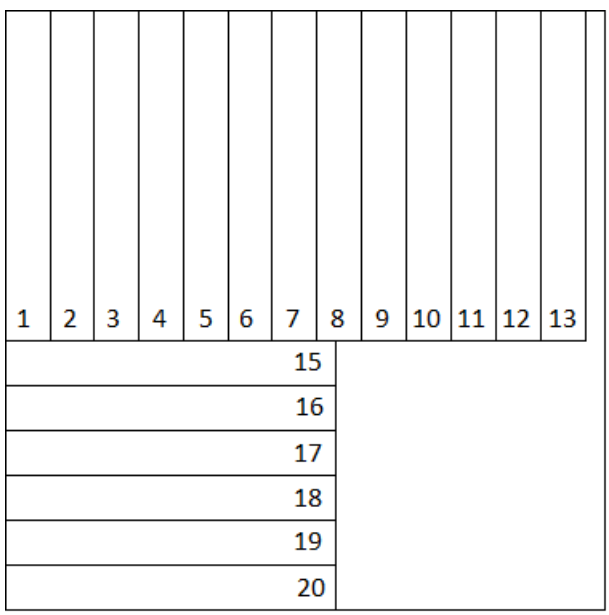

Figure 16. Specimen cutting plan for composite panels. Note 1: specimen number 14 does not exist. Note 2: specimens 1-13 oriented perpendicular to specimens 15-20.

It is seen that specimens 15-20 (specimen 16 was improperly machined, so it was discarded) produced the initial modulus values grouped at 70 GPa. Note that specimens 15-20 were cut perpendicular to specimens 1-13. All specimens in composite panel 306 have an equal number of 0° plies and 90° plies. However, the stacking sequence for specimens 1-13 is the opposite of the stacking sequence for specimens 15-20 (see Figure 17). Such difference in stacking sequence should not make any difference in mechanical properties. Both stacking sequences in Figure 17 result in the same amount of reinforcing fibers oriented along the specimen axis (the 0° fibers). Indeed, the different stacking sequences for specimens 1-13 and specimens 15-20 do not affect the modulus results obtained for panel 313. Hence we suspect that internal defects introduced during composite manufacturing are behind lower modulus values obtained for specimens 15-20 in panel 306. Apparently, the portion of panel 306, from which specimens 15-20 were cut, contained internal defects that the rest of that panel did not.

0°
90°
0°
90°
90°
0°
90°
0°

90°
0°
90°
0°
0°
90°
0°
90°

Figure 17. Stacking sequence of specimens 1-13 (left) and specimens 15-20 (right)

Initial modulus measurements obtained for the ±45 specimens of panel 314 are presented in Figure 18. Note two outliers in Figure 18, specifically the initial modulus values obtained for specimens 11 and 19. Initial modulus values obtained for the rest of the specimens in panel 314

are fairly consistent. However, even if the modulus values obtained for specimens 11 and 19 are removed from consideration, the coefficient of variation is still a relatively high 10.45. A coefficient of variation of 10 or lower would suggest the specimen-to-specimen variability is small enough to be neglected. Notably, modulus values obtained for specimens in panel 306 also produced a coefficient of variation greater than 10. High coefficients of variation noted for the modulus values in panels 306 and 316 suggest that considerable specimen-to-specimen variability is present in both 0/90 and ±45 panels. Further refining of the manufacturing process is necessary in order to produce a consistent and predictable end product.

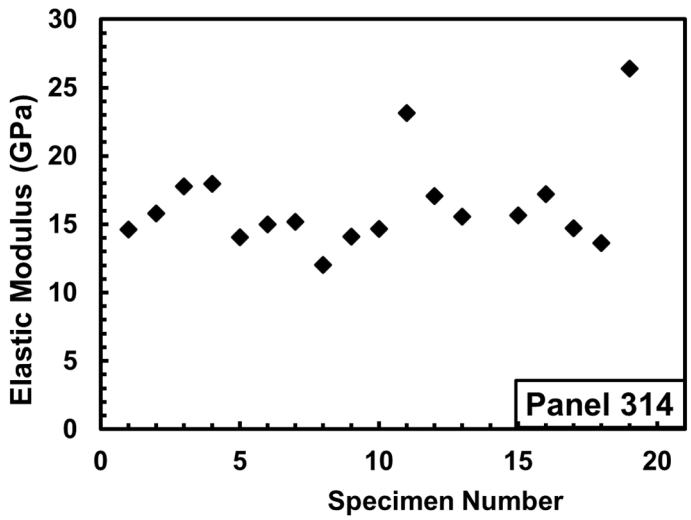

Figure 18. Modulus values for the specimens of panel 314

5.2 Thermal Expansion

This research effort included a series of tension-tension fatigue tests performed at 150 °C. In these tests, strain was measured and recorded during heat-up to test temperature and the 45-min. soak at test temperature as well as during the fatigue test. Hence thermal expansion of the composite could be assessed. A representative plot of thermal strain measured and recorded

during heat-up and soak is shown in Figure 19. Thermal strains measured in the high-temperature fatigue tests are summarized in Table 9.

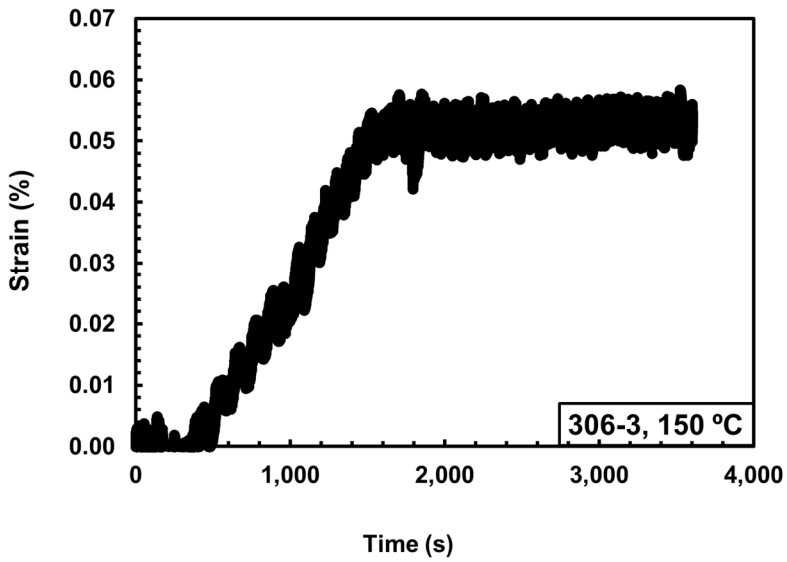

Figure 19. Thermal strain measured for specimen 306-3 during temperature increase from 23 to 150 °C and thermal soak at 150 °C.

Table 9: Thermal strains measured in elevated temperature fatigue tests

Panel/ Specimen	Fiber Orientation	T_{Left} Command (°C)	T_{Right} Command (°C)	Strain (%)
306-12	0/90	154	148	0.0355
306-10	0/90	194	0	0.1137
313-7	0/90	154	148	0.0552
306-3	0/90	154	148	0.0526
306-5	0/90	154	148	0.0613
306-20	0/90	154	148	0.0112
313-6	0/09	194	0	0.0733
313-18	0/90	194	0	0.2718
Average				**0.0843**

Note that elevated temperature testing was carried out on two different load frames. Specimens 306-10, 313-6, and 313-18 were all tested on Station 3, as laid out in section 4.3.2. The furnace

at Station 3 does not have the left and right heating zones, rather it has the upper and lower heating zones. Therefore, for specimens tested in Station 3, T_{Left} represents the temperature command for the upper zone and T_{Right}, the temperature command for the lower zone. Setting the temperature command for the upper zone as T_{Left} = 194 °C and the temperature command for the lower zone as T_{Right} = 0 °C resulted in the test specimen achieving and maintaining the desired test temperature of 150 °C.

5.3 Monotonic Tensile Tests

The results of tension to failure tests obtained at room temperature (23 °C) as well as at 150 °C are summarized in Table 10, where average values of the elastic modulus, ultimate tensile strength (UTS), normalized UTS, and failure strain are reported for each fiber orientation.

The elastic modulus, E, was determined as the slope of the initial linear region of a stress-strain curve. Engineering stresses obtained in tension to failure tests were normalized in order to reduce data scatter due to specimen-to-specimen variability. Normalized stress was calculated as follows:

$$\sigma_{normalized} = \sigma_{actual} \frac{E_{avg}}{E_{specimen}} \tag{5.1}$$

Where $\sigma_{normalized}$ is the normalized stress, σ_{actual} is the actual engineering stress, E_{avg} is the average elastic modulus for a given fiber orientation, and $E_{specimen}$ is the elastic modulus of the individual specimen. Calculation and examination of normalized stresses facilitates comparison between results obtained for different test specimens for a given fiber orientation.

Table 10: Summary of tensile properties for the AD-composite at 23 °C and 150 °C.

Fiber Orientation	Temperature (°C)	Average Elastic Modulus (GPa)	Average UTS (MPa)	Average Normalized UTS (MPa)	Average Failure Strain (%)
0/90	23	79.72	818.22	813.13	1.226
±45	23	16.35	92.34	92.21	2.124
0/90	150	48.20	805.30	489.33	1.632

Note the normalized UTS for the elevated temperature 0/90 specimens. It is 60.8% of the non-normalized value. This large difference between the two values was due to the large drop in elastic modulus at elevated temperature. Due to this drop, normalizing the UTS for the elevated temperature 0/90 specimens is not a reliable metric for judging the strength of these specimens.

5.3.1 Monotonic Tension at Room Temperature

The results obtained in the room-temperature tension to failure tests are presented in Table 11.

Table 11: Results of room-temperature tension to failure tests for 0/90 and ±45 specimens

Panel/ Specimen	Fiber Orientation	Temperature (°C)	Elastic Modulus (GPa)	UTS (MPa)	Normalized UTS (MPa)	Strain at Failure (%)
306-1	0/90	23	82.07	803.85	824.55	1.158
306-2	0/90	23	77.05	840.65	809.56	1.470
313-1	0/90	23	77.47	776.45	747.38	1.092
313-4	0/90	23	82.29	851.94	871.04	1.185
314-1	±45	23	14.62	96.14	85.92	1.693
314-2	±45	23	15.81	89.26	86.28	2.534
314-3	±45	23	17.77	89.41	97.10	2.089
314-16	±45	23	17.22	94.57	99.52	2.181

Note that the tensile properties obtained for the 0/90 fiber orientation exhibit little scatter, indicating low specimen-to-specimen variability. Coefficients of variation calculated for the 0/90

modulus values and the 0/90 UTS values are both below 10.0. Similar observations can be made regarding the tensile properties obtained for the ±45 specimens. Conversely, failure strain data obtained for both fiber orientations exhibit considerable scatter. Tensile stress-strain behavior of the 0/90 composite is typified in Figure 20. As expected, tensile response of the 0/90 specimens is fiber-dominated. The 0/90 tensile stress-strain curves are linear to failure. The linear nature of the 0/90 tensile stress-strain curves also suggests that during the manufacturing process, the fibers were laid down correctly along the 0° direction.

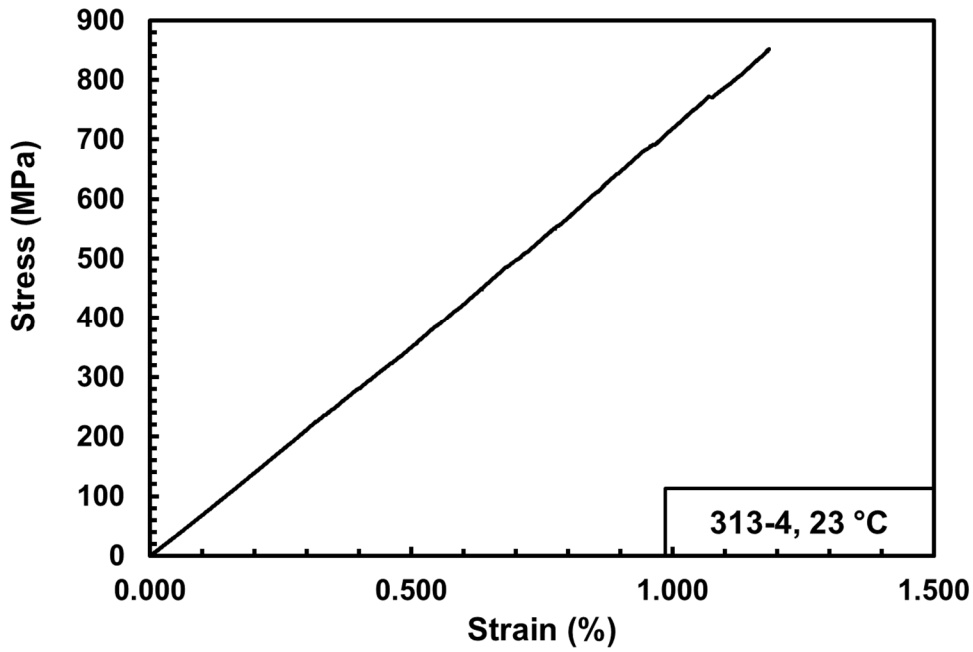

Figure 20. Typical tensile stress-strain curve obtained for the 0/90 composite at 23°C.

Tensile stress-strain behavior of the ±45 composite at 23 °C is typified in Figure 21. Clearly the tensile strength of the ±45 fiber orientation is much lower than that of the 0/90 fiber orientation. This result is not surprising since the tensile behavior of the ±45 composite is dominated by the weak viscoelastic matrix, while the tensile response of the 0/90 composite is

dominated by the strong linear elastic carbon fibers. The stress-strain behavior of the ±45 fiber orientation becomes nonlinear at approximately 40 MPa. Notably, failure of the ±45 specimens does not occur at the point of maximum stress. After reaching the UTS, stress decreases while strain continues to increase until failure. As expected, tensile stress-strain behavior of the AM composite with ±45 fiber orientation is qualitatively the same as that reported for a typical TM carbon fiber reinforced polymer matrix composite with the ±45 fiber orientation.

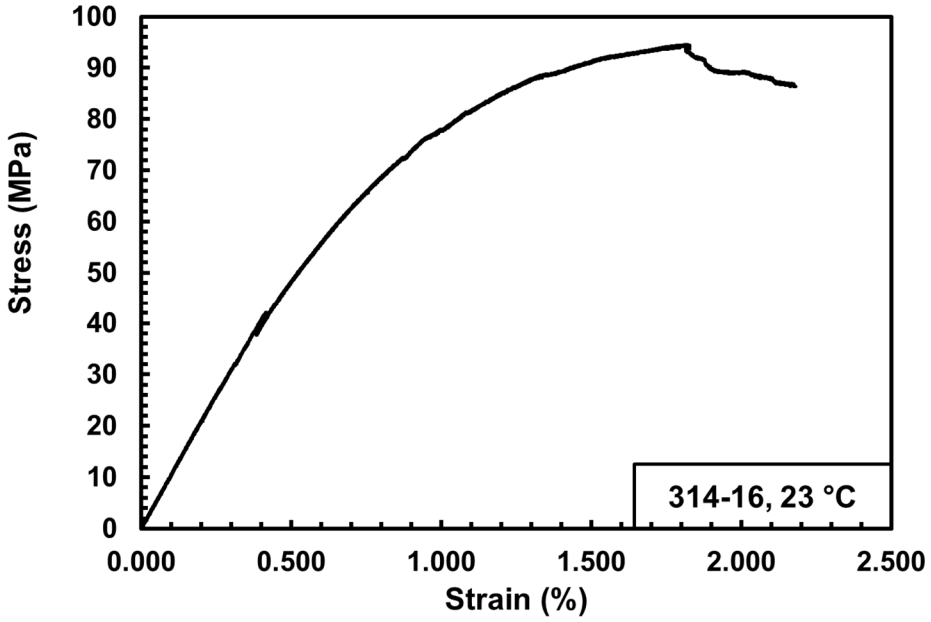

Figure 21. Typical tensile stress-strain curve obtained for the ±45 composite at 23 °C.

Typical tensile stress-strain curves obtained for the 0/90 and ±45 fiber orientations shown together in Figure 22. A comparison in Figure 22 clearly highlights the differences in tensile stress-strain behaviors produced by the 0/90 and the ±45 composites.

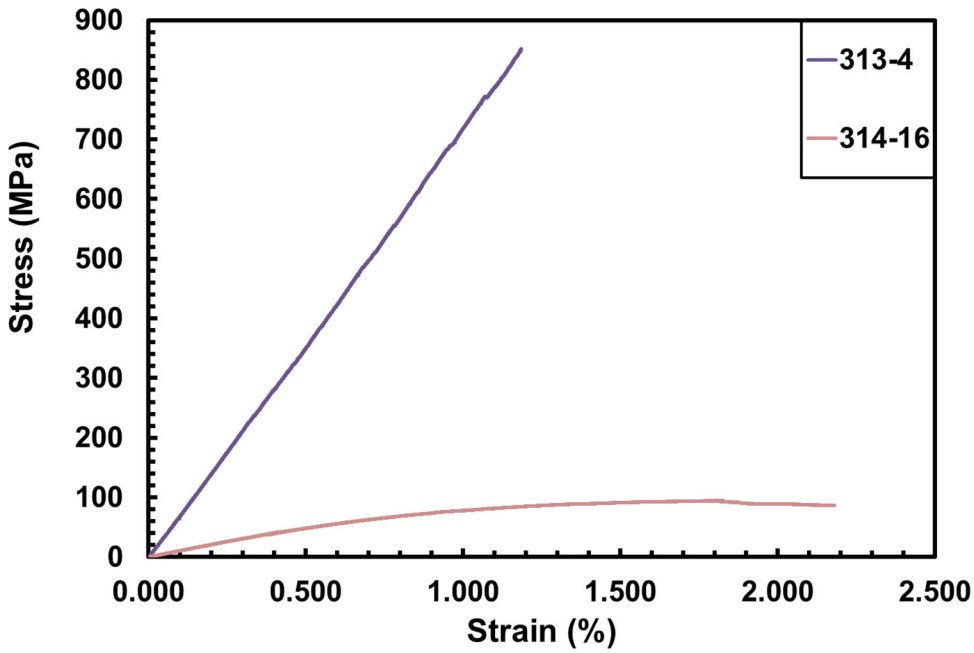

Figure 22. Typical tensile stress-strain curves obtained for the 0/90 and ±45 fiber orientations at room temperature.

5.3.2 Monotonic Tension at Elevated Temperature

Specimens with 0/90 fiber orientation were tested in tension to failure at 150 °C in laboratory air. Test results are summarized in Table 12. Due to shortage of test material, specimens with ±45 fiber orientation were not tested in tension to failure at elevated temperature. We recommend that this testing be performed in the follow-on effort. Because the tensile response of the ±45 composite is dominated by the response of the viscoelastic polymer matrix, tension tests at 150 °C are expected to produce interesting and informative results.

Table 12: Tensile properties obtained for the AM composite with 0/90 fiber orientation at 150 °C

Panel/ Specimen	Fiber Orientation	Temperature (°C)	Elastic Modulus (GPa)	UTS (MPa)	Failure Strain (%)
313-8	0/90	150	-*	771.03	-*
313-19	0/90	150	37.23	821.75	1.470
313-9	0/90	150	46.87	826.37	1.648
306-18	0/90	150	60.51	801.80	1.618

*No strain data available

Results in Table 12 demonstrate that temperature greatly affects the elastic modulus of the 0/90 specimens. In contrast, the elevated temperature had virtually no effect on the UTS. Likewise, failure strains at 150 °C increased only marginally compared to the values obtained at 23 °C. Representative stress-strain curves obtained at 150 °C are shown in Figure 23 and Figure 24.

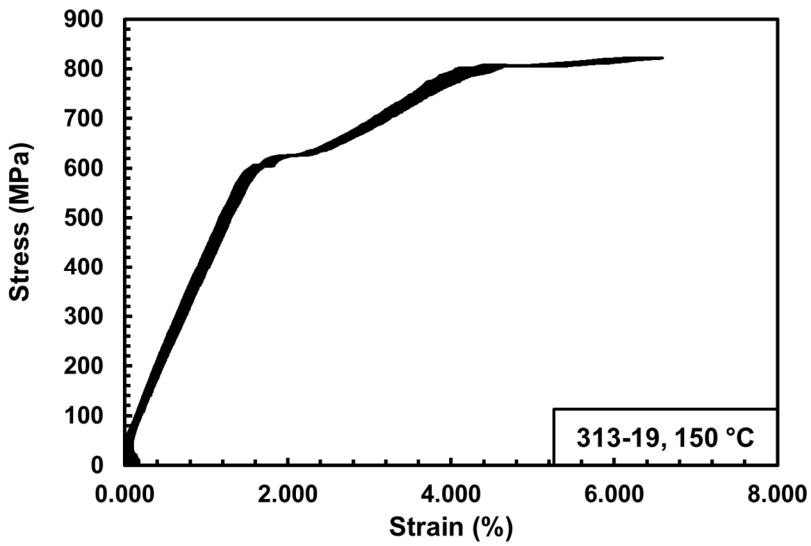

Figure 23. Tensile stress-strain curve obtained for specimen 313-19 at 150 °C.

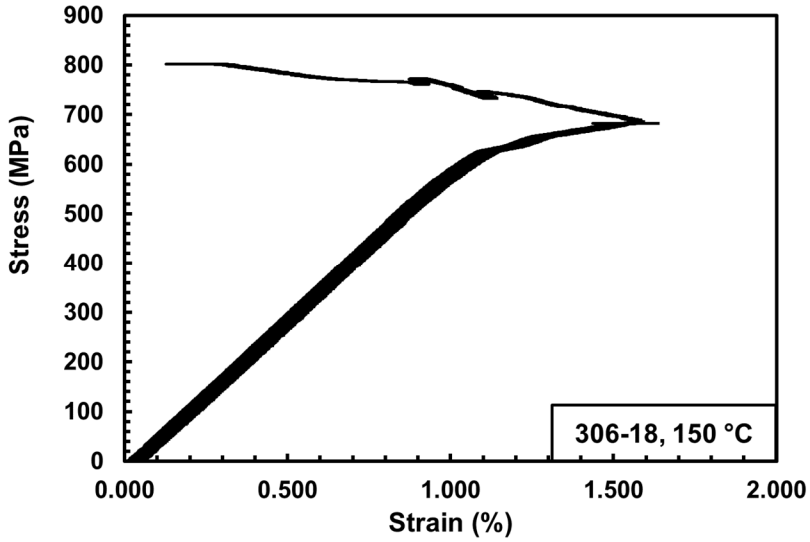

Figure 24. Tensile stress-strain curve obtained for specimen 306-18 at 150 °C.

Both tensile stress-strain curves exhibit a range of linear elastic behavior. Once the stress exceeds the elastic limit a strain perturbation is observed. It may be argued that such strain perturbation is an artifact caused by extensometer slippage. Yet it is possible that such strain perturbations are caused by local damage events occurring in the composite.

5.3.3 Comparison of AM-PMC and TM-PMC Monotonic Tension Behavior

As mentioned earlier, additive manufacturing techniques promise to reduce fabrication costs associated with manufacturing composite parts using traditional methods. Yet benefits gained in one area frequently come at the cost of losses in another. Hence it is important to ascertain that the mechanical properties and performance of the AM composites remain comparable to those of the TM composites. Hence we compare the results obtained for the AM composite in this work to the results of prior studies of the TM composites. Ideally, the TM composite would have the same constituents as the AM composite. Yet in the absence of the TM

composite with the same resin and fibers as the AM composite studied in this work we turn to TM composites that use carbon fibers, but have different resins. Previous studies at AFIT examined mechanical performance of typical aerospace grade composites [16, 17]. The data from these two studies is used as the baseline to which we compare results obtained for the AM-PMC in this work. Tensile properties obtained in prior work for the baseline TM-PMCs are presented in Table 13.

Table 13: Tensile properties obtained for two TM-PMCs at room and elevated temperatures. Data for IMR/977-3 composite from Lam [16]. Data for NRPE/T650-35 from Wilkinson [17].

Material Type	**Fiber Orientation**	**Temperature (°C)**	**Elastic Modulus (GPa)**	**UTS (MPa)**
IM7/977-3	0/90	23	79.8	1037
IM7/977-3	0/90	23	78.3	1042
IM7/977-3	0/90	23	80.8	1043
IM7/977-3	±45	23	16.7	279
IM7/977-3	±45	23	17.8	278
IM7/977-3	±45	23	17.0	272
NRPE/T650-35	0/90	329	60.93	834.4
NRPE/T650-35	0/90	329	58.03	809.6
NRPE/T650-35	0/90	23	56.87	831.8

Results in Table 13 reveal that the room-temperature values of the elastic modulus obtained for the AM-PMC (79.72 GPa for the 0/90 fiber orientation and 16.35 GPa for the ±45 fiber orientation) compare well to the modulus values obtained for the TM-PMC materials. The room-temperature UTS values obtained for the AM-PMC also compare well with those reported for the NRPE/T650-35. In contrast, the room-temperature UTS values reported for the IMR/977-3 significantly exceed those obtained for the AM-PMC (818 MPa). As regards the UTS, the IM7/977-3 composite outperforms the AM-PMC material for both fiber orientations. This result is surprising in the case of the 0/90 fiber orientation. Tensile properties and response of the 0/90

fiber orientation are fiber-dominated. The tensile strengths of the IM7 fibers and of the T1100 fibers used in the AM-PMC are 2510 MPa and 7000 MPa, respectively [18, 19]. Because the AM-PMC is reinforced with the stronger fibers, it should produce higher 0/90 UTS. Yet the 0/90 UTS of the AM-PMC is some 20% lower than the 0/90 UTS of the IM7/977-3 composite. The underperformance of the AM-PMC could be due to the additive manufacturing process making an uneven composite microstructure. This uneven microstructure could lead to stress concentrations within the composite specimen causing premature failure.

As mentioned above, the ±45 UTS of the AM-PMC (92 MPa) is also considerably lower than the ±45 UTS of the IM7/977-3 material system. Tensile properties and behavior of the ±45 composite are dominated by the polymer matrix. Due to the proprietary nature of the resin used in the AM-PMC tensile properties of this resin are not available for comparison with the matrix properties of the IM7/977-3 material system. However, the low ±45 UTS values obtained for the AM-PMC suggest that the resin used in the AM composite could be very brittle and fail at low stress levels.

In this work the 0/90 AM-PMC was also tested at 150 °C. However, the two TM-PMC examined in prior studies at AFIT (see Table 13) were not. Hence a direct comparison of tensile properties and behavior at 150 °C is not possible. The NRPE/T650-35 composite was tested in tension with one side of the specimen at 329 °C and the other side open to laboratory air. These results are now compared to the results obtained for the 0/90 AM-PMC at 150 °C. While not ideal, this comparison offers an interesting insight. The high-temperature UTS values obtained for the AM-PMC and the TM-PMC are close. A different trend is observed regarding the high-temperature elastic modulus. While elevated temperature has little effect on the elastic modulus of the 0/90 NRPE/T650-35 composite, the modulus of the 0/90 AM-PMC drops by some 40% as

the temperature increases from 23 to 150 °C. Note that the NRPE/T650-35 materials system is specifically designed for high temperature applications while the AM-PMC is not.

5.4 Tension-Tension Fatigue at 23 °C

5.4.1 Fatigue Performance of the 0/90 AM-PMC

All fatigue tests were performed with a ratio of minimum stress to maximum stress of R = 0.1 at a frequency of 1 Hz. Fatigue run-out was set to 200,000 cycles. A summary of the tension-tension fatigue results obtained for the 0/90 AM-PMC at room temperature (23 °C) is presented in Table 14. The results are also shown as maximum stress vs. cycles to failure (S-N) curve in Figure 25. It can be seen that there is a small difference in maximum stresses resulting in fatigue failure and those resulting in fatigue runout of 200,000 cycles. Interestingly, there is much scatter cyclic life at a stress level of 85% UTS. Three tests were performed with that maximum stress, producing three very cyclic lives - 30,648 cycles, 180,780 cycles, and 200,000 (fatigue runout).

Table 14: Tension-tension fatigue results for the AM-PMC with 0/90 fiber orientation at 23 °C

Specimen Number	Maximum Stress (%UTS)	Maximum Stress (MPa)	Normalized Maximum Stress (MPa)	Cycles to Failure
306-15	75	605.87	684.74	200,000*
313-12	90	728.85	752.20	3,571
306-9	80	656.11	644.65	200,000*
306-13	85	691.28	662.89	30,648
306-17	80	649.71	756.19	200,000*
306-4	85	693.47	581.11	200,000*
306-11	82	682.84	639.87	200,000*
306-8	87	712.47	721.31	9,543
306-6	85	701.70	710.68	180,780

* Fatigue run-out; defined as 200,000 cycles. Failure of specimen did not occur when the test was terminated.

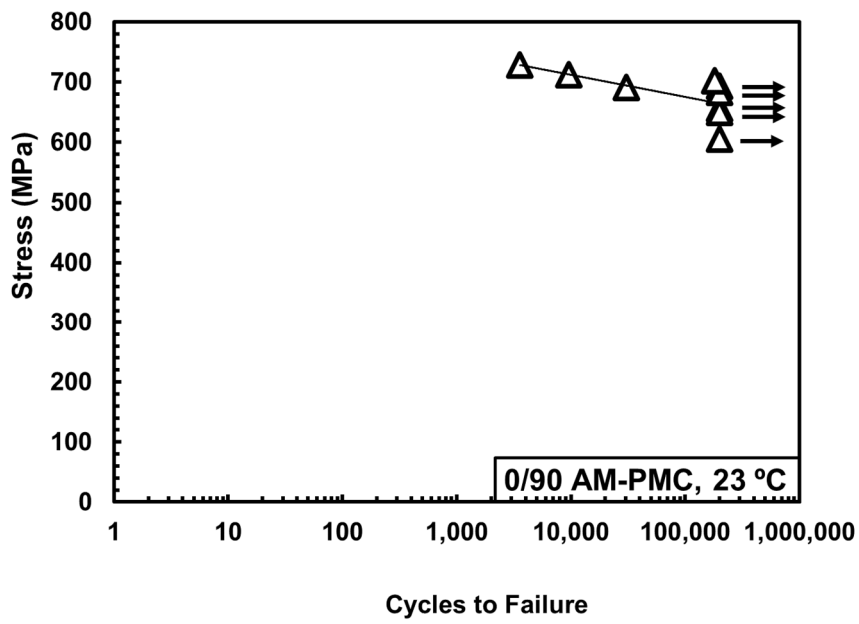

Figure 25. Fatigue S-N curve obtained for the 0/90 AM-PMC at room temperature

It is likely that various randomly distributed internal defects in the specimens tested with the fatigue stress of 85 %UTS are behind the observed data scatter. The presence and distribution of the internal defects in the test material are further discussed in subsequent sections where the X-Ray CT data are presented. Because we observed fatigue failures as well as a fatigue runout in tests performed with the maximum stress of 85%UTS, we propose that fatigue runout stress be set to 82%UTS. Figure 26 (specimen 306-11, σ_{max} = 682 MPa, N_f > 200,000) shows a representative evolution of the stress-strain hysteresis response for the 0/90 AM-PMC specimens that achieved fatigue runout of 200,000 cycles. Note that the curves in Figure 26 are shifted by 0.1% for clarity.

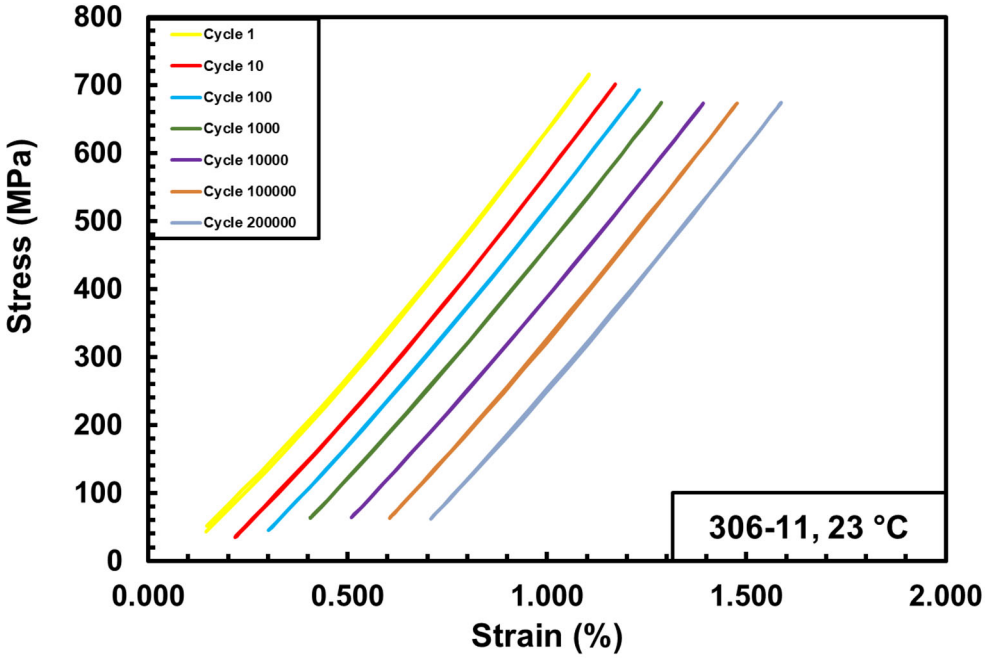

Figure 26. Typical evolution of the stress-strain hysteresis response for the 0/90 AM-PMC specimens tested in tension-tension fatigue at 23 °C. Curves shifted by 0.1% for clarity.

The evolution of the stress-strain hysteresis response recorded for specimen 306-9 (σ_{max} = 656 MPa, N_f > 200,000) presented in Figure 27 differs considerably from the typical results shown in Figure L. It can be seen that specimen 306-9 produced a much wider stress-strain hysteresis loop during the last recorded cycle. Figure 28 shows the evolution of the stress-strain hysteresis response for specimen 306-9 between cycles 100,000 and 180,000. Note the visible change in the appearance of the hysteresis loop that signals the step-up in damage development. Apparently, the damage events that caused this behavior occurred between cycles 170,000 and 180,000. Figure 29 shows the evolution of the stress-strain hysteresis response for specimen 306-9 between cycles 100,000 and 170,000, highlighting the gradual damage development. The stress-strain hysteresis loops in Figure 29 can be seen gradually widening and becoming more "S" shaped as the fatigue cycling progresses.

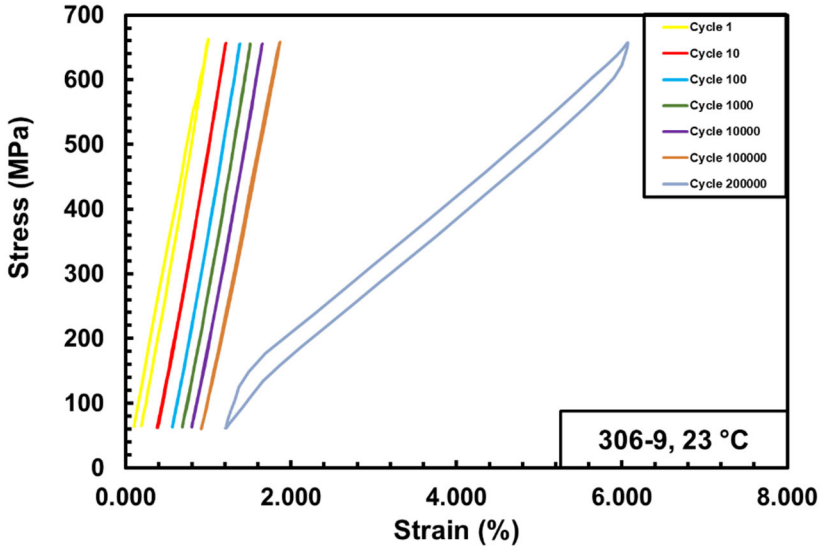

Figure 27. Evolution of the stress-strain hysteresis response for specimen 306-9 tested in tension-tension fatigue at 23 °C (σ max = 656 MPa, Nf > 200,000).

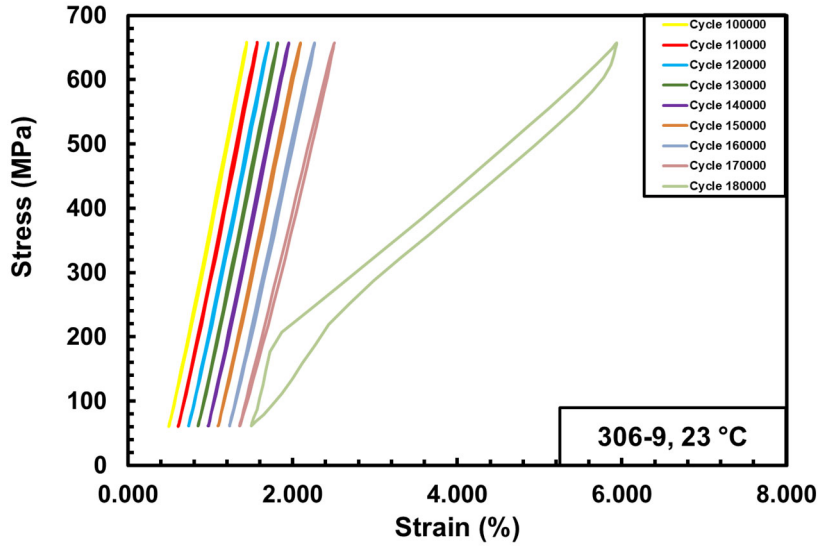

Figure 28. Evolution of the stress-strain hysteresis response for specimen 306-9 between cycles 100,000 and 180,000, highlighting the visible step-up in damage development.

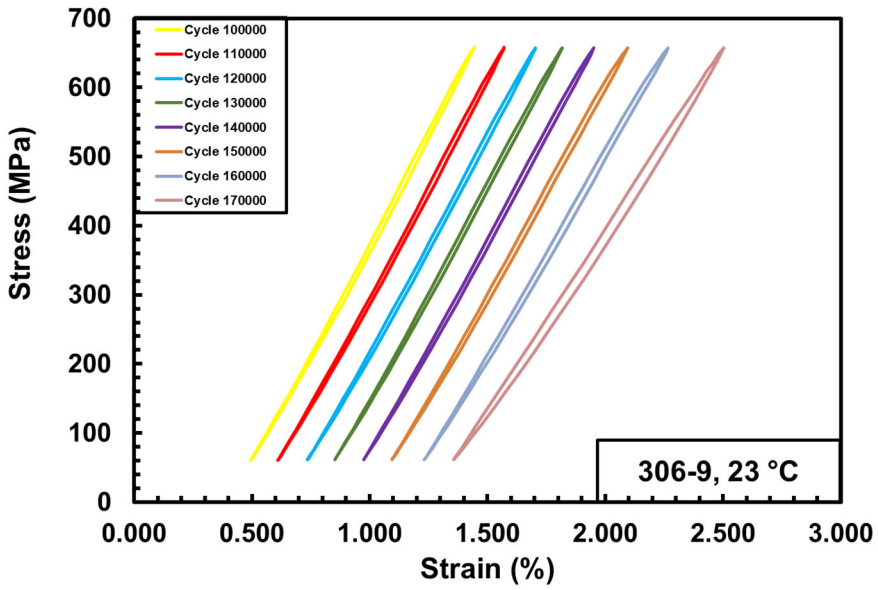

Figure 29. Evolution of the stress-strain hysteresis response for specimen 306-9 between cycles 100,000 and 170,000, highlighting the gradual damage development.

Changing shape of the stress-strain hysteresis loops indicate progressive damage development. The exact damage mechanism occurring in specimen 306-9 is difficult to ascertain. However, it is likely that the dominant damage mechanism operating in this case was delamination. As seen in Figure 26, the typical stress-strain hysteresis loops obtained for specimens that achieved fatigue runout do not exhibit much change in the slope or area within the loop. The change in slope of the stress-strain loop indicates a change in the stiffness of the specimen. The area of the hysteresis loop represents the energy lost per cycle. Having an unloading path that nearly mirrors the loading path indicates nearly linear behavior. As the specimen accrues more damage, such as seen in Figure 29, the stress-strain loops will widen and their slope will decrease, indicating departure from the linear elastic behavior. Eventually, the stress-strain hysteresis may take on a more distorted shape such as seen in Figures 27 and 28. Note that specimens 313-12 and 306-8 produced the stress-strain hysteresis behavior similar to that noted for specimen 306-9. Notably,

specimens 313-12 (σ_{max} = 752 MPa, N_f = 3,571) and 306-8 (σ_{max} = 712 MPa, N_f = 9,543) also produced much shorter cyclic lives, while specimen 306-9 reached fatigue runout of 200,000 cycles. As seen in Figure 30, specimen 306-8 accrues damage in a more gradual manner; the appearance of the stress-stain hysteresis loops changes gradually.

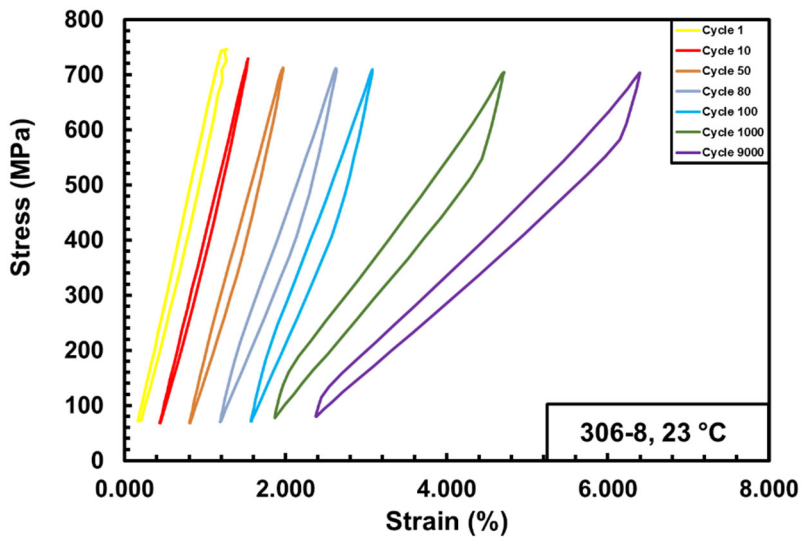

Figure 30. Evolution of the stress-strain hysteresis response for specimen 306-8 tested in tension-tension fatigue at 23 °C (σ max = 712 MPa, Nf = 9,543).

To assess the damage development during cyclic fatigue, it is instructive to consider the change in hysteresis modulus with fatigue cycles. Note that the hysteresis modulus is calculated from peak and valley stress-strain data in a fatigue cycle. A typical variation in normalized modulus (i.e. modulus divided by the hysteresis modulus of the first cycle) obtained in this work is shown in Figure 31.

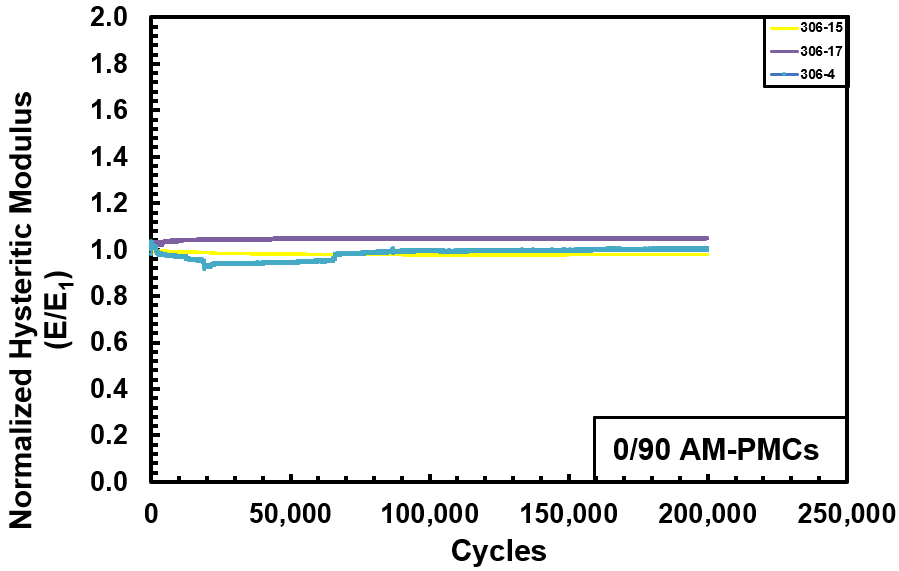

Figure 31. Normalized modulus vs cycles for specimens 306-15 (□max = 605 MPa, Nf > 200,000), 306-17 (□max = 650 MPa, Nf > 200,000), and 306-4 (□max = 693 MPa, Nf > 200,000).

Note that all specimens represented in Figure 31 achieved fatigue run-out of 200,000 cycles. Hence it is not surprising that little change in modulus is seen in Figure 31. A general trend was noted for the 0/90 specimens where audible "crunch" noises were heard during the first dozen or so cycles. The noises would cease after these early cycles. The audible noises are likely a result of local failure events occurring in the composite interior. Many plots of the normalized modulus vs cycles to failure reflect these early failure events; the normalized modulus drops during early cycles, then continues at a near constant level. An example of this trend is seen in Figure 32 where the normalized modulus is plotted vs cycles to failure for specimen 306-8 (σ_{max} = 712 MPa, N_f = 9,543).

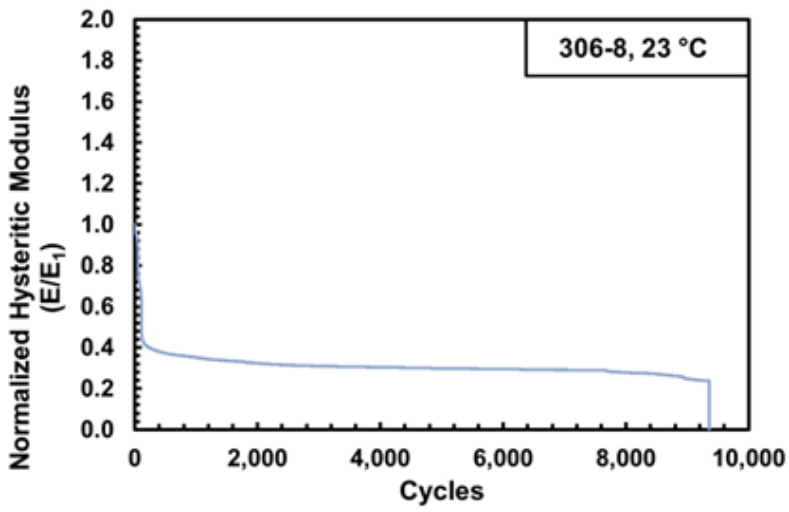

Figure 32. Normalized modulus vs cycles for specimen 306-8 (□max = 712 MPa, Nf = 9,543).

Figure 32. Normalized modulus vs cycles for specimen 306-8 (σ_{max} = 712 MPa, N_f = 9,543).

5.4.1.1 Comparison of 0/90 AM-PMC and TM-PMC Fatigue Performance

The fatigue results obtained for the 0/90 AM-PMC at 23°C in this work were compared with the fatigue results obtained for the 0/90 IM7/977-3 material system studied previously. Results of the previous study are presented in Table 15.

Table 15: Tension-tension fatigue results for the IM7/977-3 composite with 0/90 fiber orientation at 23 °C

Material Type	Maximum Stress (%UTS)	Maximum Stress (MPa)	Cycles to Failure
IM7/977-3	80	827	200,000*
IM7/977-3	90	932	200,000*

* Fatigue run-out defined as $2x10^5$ cycles. Failure of specimen did not occur when the test was terminated

The IM7/977-3 material systems clearly outperforms the AM-PMC in tension-tension fatigue at 23 °C. The IM7/977-3 system has a high runout stress of 90% of its UTS, whereas the AM-PMC achieves runout at the maximum stress of 82% UTS. Additional fatigue testing of the AM-PMC is recommended for the follow-on effort in order to establish statistical confidence in the results and permit better comparison with the results obtained for the TM aerospace-grade composites.

5.4.2 Fatigue Performance of the ±45 AM-PMC

All fatigue tests were performed with a ratio of minimum stress to maximum stress of R = 0.05 at a frequency of 1 Hz. Fatigue run-out was set to $2x10^5$ cycles. A summary of the tension-tension fatigue results obtained for the ±45 AM-PMC at room temperature (23 °C) is presented in Table 16. The results are also shown as maximum stress vs. cycles to failure (S-N) curve in Figure 33.

Table 16: Tension-tension fatigue results for the AM-PMC with ±45 fiber orientation at 23 °C

Specimen Number	Maximum Stress (%UTS)	Maximum Stress (MPa)	Normalized Maximum Stress (MPa)	Cycles to Failure
314-11	80	72.15	51.02	4962
314-9	65	56.74	65.90	88345
314-5	50	44.39	51.66	200,000*
314-13	60	52.53	55.22	200,000*
314-8	63.5	59.10	80.54	168010
314-15	65	60.14	62.94	14932
314-7	65	59.55	64.17	22617

* Fatigue run-out defined as $2x10^5$ cycles. Failure of specimen did not occur when the test was terminated

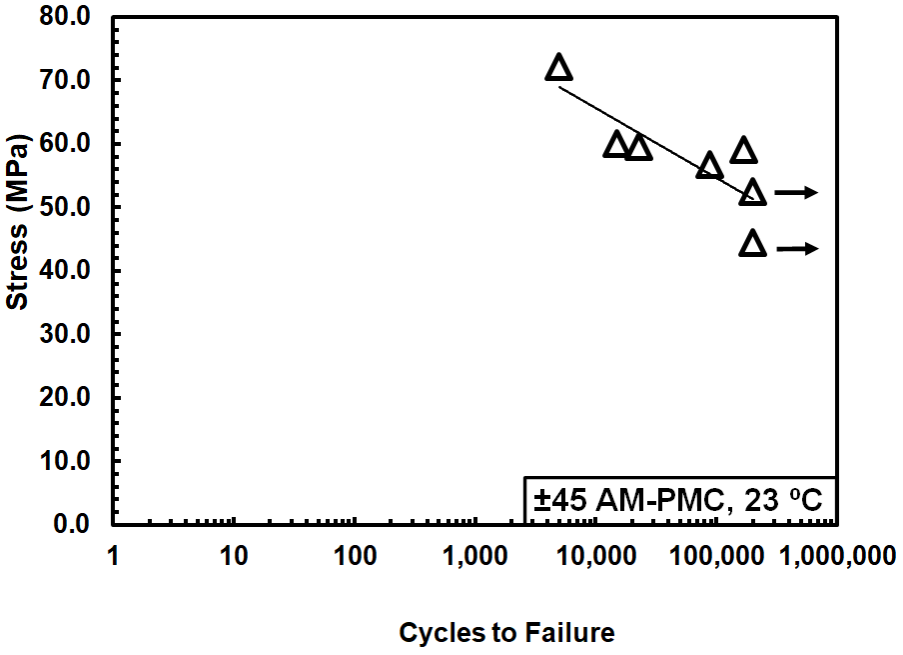

Figure 33. Fatigue S-N curve obtained for ±45 AM-PMC at room temperature

For the ±45 AM-PMC specimens, the fatigue limit was reached at 60% of UTS. The results presented in Table 16 for specimens 314-11 and 314-8 are worth noting. Statistically, they are outliers that suggest that the normalized maximum stress is not a useful measure. Specimens 314-11 and 314-8 have the second highest and lowest elastic modulus values respectively. Hence the normalized maximum stresses calculated for these specimens differ significantly from the actual maximum stresses. Furthermore, slope of the S-N curve plotted on the basis of the normalized maximum stress is the opposite of that traditionally expected. Hence the S-N data obtained for the ±45 specimens plotted on the basis of the actual maximum stress.

The S-N data obtained for the 0/90 and ±45 specimens are compared in Figure 34 where the maximum stress is plotted in terms of %UTS. The fatigue envelope for the ±45 specimens is much wider than that for the 0/90 specimens. In the case of the ±45 specimens, the S-N data

cover the maximum stress range from 60 to 80 %UTS. In contrast, the S-N data for the 0/90 specimens cover a much narrower maximum stress range of 80-90 %UTS.

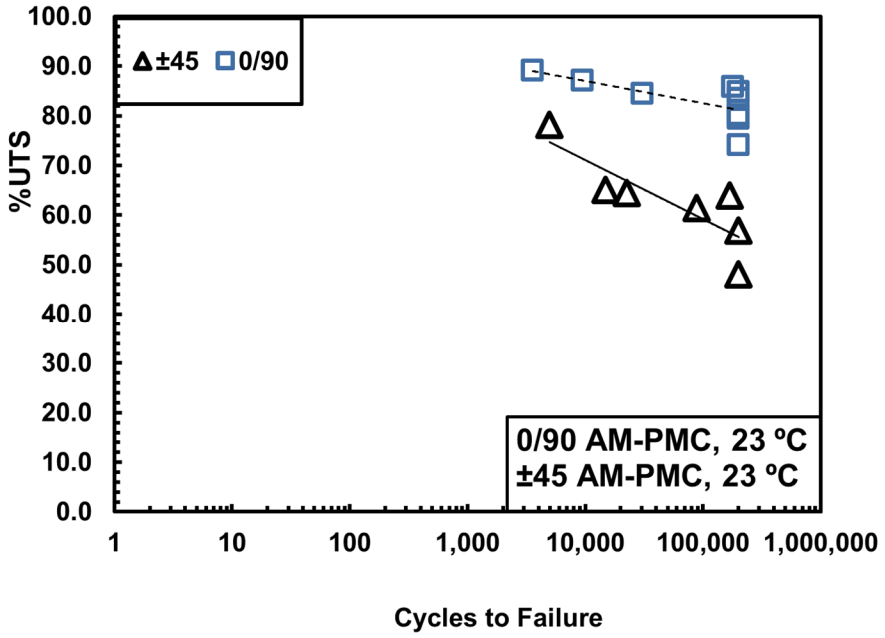

Figure 34. Fatigue S-N curves obtained for 0/90 and ±45 AM-PMC specimens at room temperature. Maximum stress is shown in terms of %UTS.

Figure 35 shows a representative evolution of the stress-strain hysteresis response the ±45 AM-PMC specimens. It can be seen that the stress-strain hysteresis loops become noticeably wider as the cycling continues. Furthermore, the slope of the hysteresis loops decreases with cycles. Changes to the stress-strain hysteresis indicate progressive damage occurring in the composite. Clearly, damage development in the ±45 specimens is more pronounced than in the 0/90 specimens. It is noteworthy that none of the stress-strain hysteresis loops generated for the ±45 specimen have the "S" shape see in the stress-strain hysteresis loops generated for the 0/90 specimens (see for example Figure 30). This observation indicates that damage mechanisms operating in the 0/90 specimens differ from those dominating the ±45 specimens.

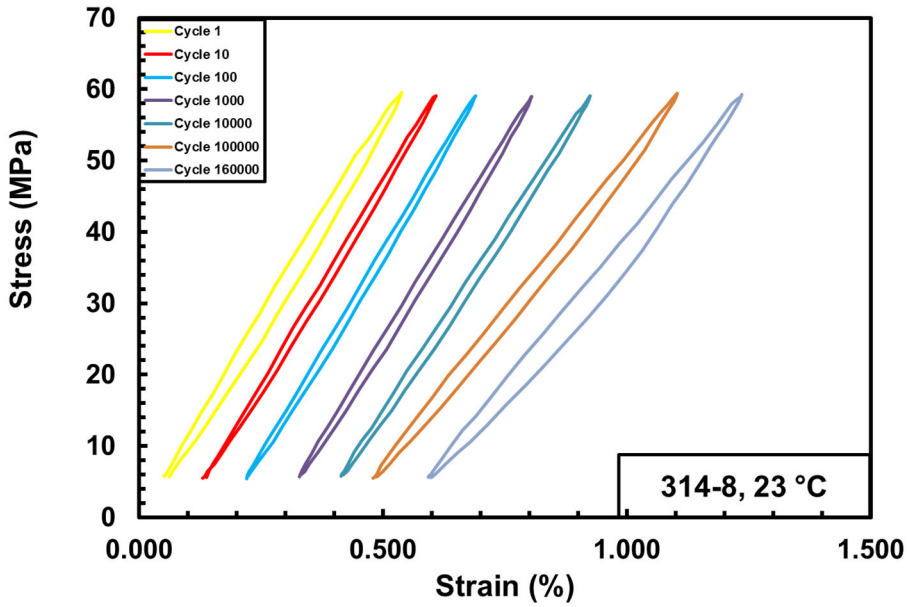

Figure 35. Typical evolution of the stress-strain hysteresis response with cycles for the ±45 specimens

The change in the normalized hysteresis modulus with cycles for the ±45 specimens is shown in Figure 36. Note that the trend seen in Figure 36 is different from that reported for the 0/90 specimens above. Unlike in the case of the 0/90 specimens, the normalized moduli obtained for the ±45 specimens do not exhibit a sharp decrease during early cycles. No audible "crunch" noises were associated with the first dozen cycles during testing of the ±45 specimens.

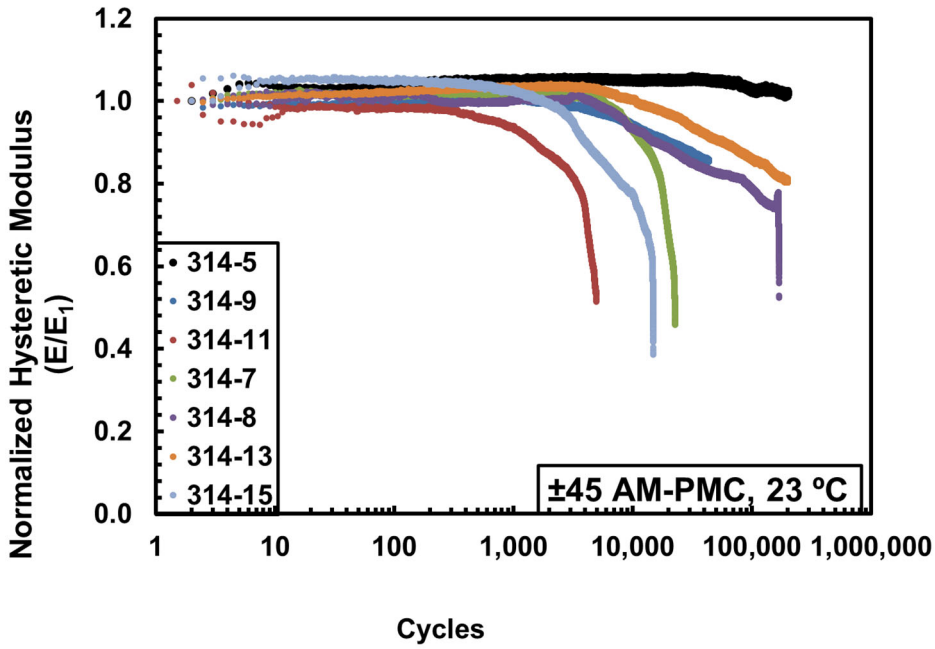

Figure 36. Normalized hysteretic modulus vs cycles for the ±45 specimens

One interesting item to note from Figure 36 is that specimens 314-7, 314-8, 314-11 and 314-15 failed when their normalized moduli dropped to about the same level (0.46, 0.52, 0.52 and 0.39), 0.4751 on average. This observation is highlighted in Figure 37, which shows the change in modulus with fatigue cycles for just these four specimens. Notably only one specimen that failed in fatigue (specimen 314-9) did not follow this trend. Specimen 314-9 failed when its normalized modulus dropped to about 0.8. It is recognized that the mechanical properties and behavior of the ±45 composite are matrix dominated. It is possible that the normalized modulus of the ±45 composite of approximately 0.4751 corresponds to a failure threshold for the matrix of this material system. We further note that the maximum stress levels used in testing specimens 314-7, 314-8, 314-11 and 314-15 range from 60 to 80 %UTS. Given that this behavior is seen over such a wide spread of load levels, it suggests that this behavior is due to the material system itself, and not due to the test conditions.

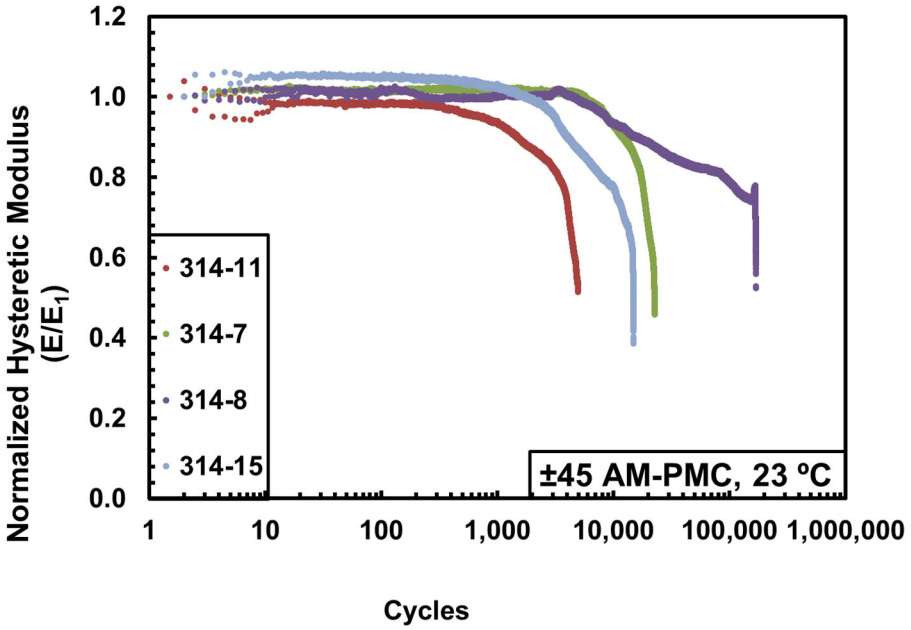

Figure 37. Normalized hysteretic modulus vs cycles to failure for specimens 314-7, 314-8, 314-11, and 314-15

5.4.2.1 Comparison of ±45 AM-PMC and TM-PMC Fatigue Performance

The fatigue results obtained for the ±45 AM-PMC at 23 °C in this work were compared with the fatigue results obtained for the ±45 IM7/977-3 material system studied previously. Results of the previous study are presented in Table 17.

Table 17: Tension-tension fatigue results for the IM7/977-3 composite with ±45 fiber orientation at 23 °C

Material System	Maximum Stress (% UTS)	Maximum Stress (MPa)	Cycles To Failure
IM7/977-3	40	105	200,000*
IM7/977-3	50	131	200,000*
IM7/977-3	55	144	1,237
IM7/977-3	60	159	18,384
IM7/977-3	60	155	11,354
IM7/977-3	70	177	311
IM7/977-3	70	180	138
IM7/977-3	70	181	3,918
IM7/977-3	80	164	1
IM7/977-3	80	194	10
IM7/977-3	80	206	2070

* Fatigue run-out defined as $2x10^5$ cycles. Failure of specimen did not occur when the test was terminated

The ±45 AM-PMC outperforms the ±45 IM7/977-3 material system in tension-tension fatigue at 23 °C. The ±45 IM7/977-3 composite achieves runout at 50% UTS. Furthermore, its cyclic life is reduced to less than 1,000 cycles in tests performed with the maximum stresses at or above 70% UTS. The AM-PMC achieves runout at 50% UTS. Moreover, its cyclic lives were at or above 1,000 cycles in all tests performed in this work. In the case of the ±45 AM-PMC the shortest cyclic life of 4,962 cycles was produced at the maximum stress of 80% UTS. The range of maximum stresses in the S-N curve produced for the ±45 AM-PMC is wider than that in the case of the ±45 IM7/977-3 material system. Additionally, the ±45 AM-PMC specimens could be successfully tested in tension-tension fatigue with the maximum stresses at high percentage of the composite's UTS. This result is particularly noteworthy considering that the UTS of the ±45 AM-PMC was noticeably lower than that of the ±45 IM7/977-3 material system.

5.5 Tension-Tension Fatigue at 150 °C

5.5.1 Fatigue Performance of the 0/90 AM-PMC at 150 °C

Several 0/90 AM-PMC specimens were tested in tension-tension fatigue at 150 °C. All fatigue tests were performed with a ratio of minimum stress to maximum stress of R = 0.05 at a frequency of 1 Hz. Fatigue run-out was set to $2x10^5$ cycles. A summary of the tension-tension fatigue results obtained for the 0/90 AM-PMC at 150 °C is presented in Table 18. The results are also shown as maximum stress vs. cycles to failure (S-N) curve in Figure 38.

Table 18: Tension-tension fatigue results for the AM-PMC with 0/90 fiber orientation at 150 °C

Specimen Number	Maximum Stress (%UTS)	Maximum Stress (MPa)	Normalized Maximum Stress (MPa)	Cycles to Failure
313-6	80	633.86	573.17	200,000*
306-12	90	718.24	610.01	55,158
306-5	85	678.74	584.48	65,563
306-20	70	569.39	644.87	200,000*
313-20	85	677.85	797.25	1,610
306-3	85	678.29	666.42	16,795
313-7	80	639.58	617.41	200,000*
306-10	85	672.66	628.51	4,856
313-18	82.5	653.41	655.67	200,000*

* Fatigue run-out; defined as $2x10^5$ cycles. Failure of specimen did not occur when the test was terminated.

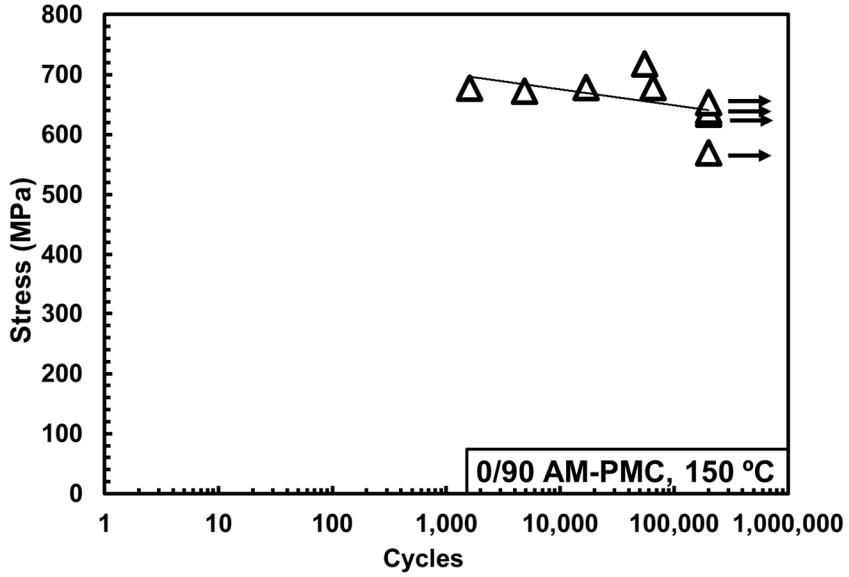

Figure 38. Actual maximum stress vs. cycles to failure (S-N) curve obtained for the 0/90 AM-PMC specimens at 150 °C

At 150 °C the 0/90 AM-PMC achieved fatigue runout at the maximum stress of 82.5%UTS. Specimen 306-12, which was tested with the maximum stress set to 90% UTS, produced an anomalous result. Because it was tested with the highest maximum stress level, it was expected to have the shortest cyclic life of all the specimens. However, data in Figure 38 demonstrate that it was not so. Note that Figure 38 presents the actual maximum stress vs. cycles to failure. When we account for specimen-to-specimen variability and plot the normalized maximum stress vs. cycles to failure (Figure 39), the anomaly disappears. The S-N curve in Figure 39 has a conventional appearance, where the highest maximum stress corresponds to the shortest cyclic life.

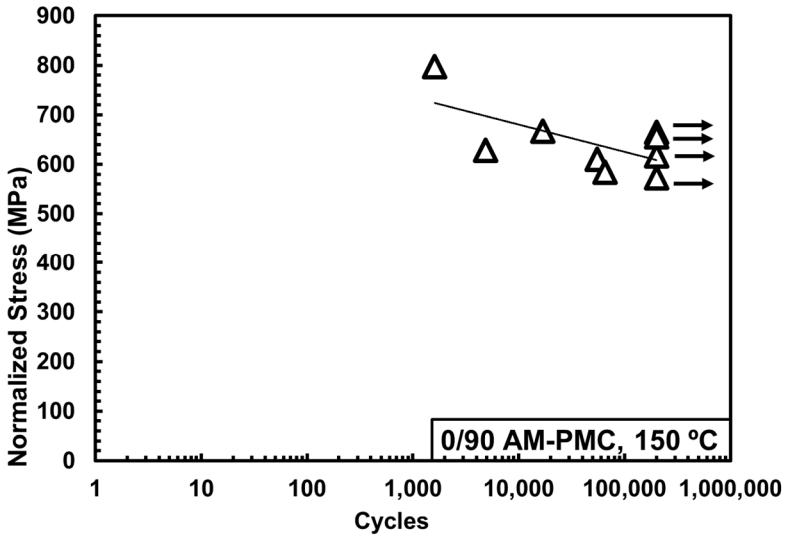

Figure 39. Normalized maximum stress vs. cycles to failure (S-N) curve obtained for the 0/90 AM-PMC specimens at 150 °C

A representative plot of the evolution of the stress-strain hysteresis response of the 0/90 AM-PMC at 150 °C is shown in Figure 40.

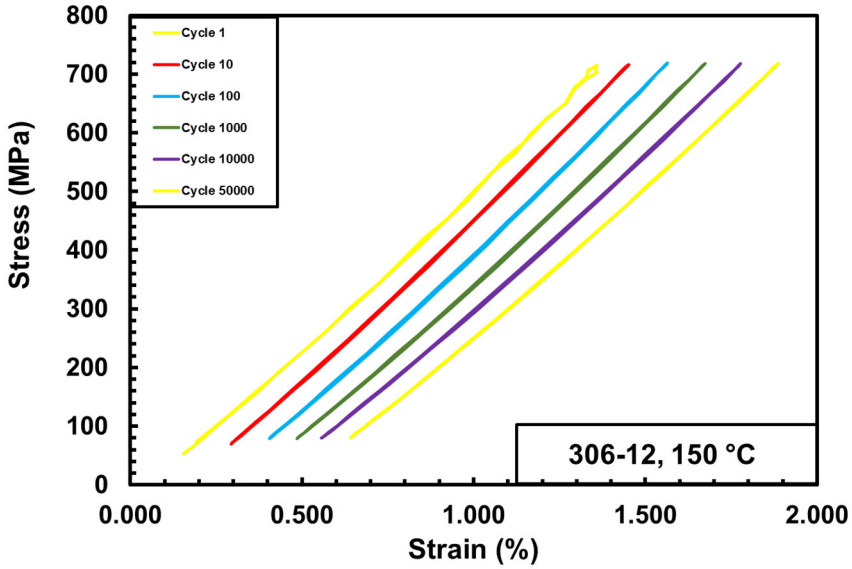

Figure 40. Typical evolution of the stress-strain hysteresis response of the 0/90 AM-PMC at 150 °C (specimen 306-12, σ max = 718 MPa, Nf = 55,158).

The strain-strain hysteresis loops change little with cycles, only slight decrease in hysteretic modulus is observed.

5.5.1.1 Comparison of Fatigue Performance at 23 °C and 150 °C

Tension-tension fatigue S-N data obtained at 150 °C are compared to the data obtained at 23 °C in Figs. CC and DD. Note that Figure 41 presents the actual maximum stress vs. cycles to failure. In order to account for specimen-to-specimen variability, the S-N data are plotted the normalized maximum stress vs. cycles to failure in Figure 42.

It is noteworthy that fatigue results produced at the maxi v mum stress of 85%UTS at both 23 and 150 °C exhibit considerable data scatter. At 150 °C, the cyclic lives produced at the maximum stress set to 85% UTS range from 1,610 cycles to 65,563 cycles. At 23 °C the cyclic lives produced at the maximum stress set to 85% UTS cover a wider cycle range (30,648 - 200,000). Note that one specimen tested at the maximum stress set to 85% UTS at 23 °C achieved fatigue runout of 200,000 cycles.

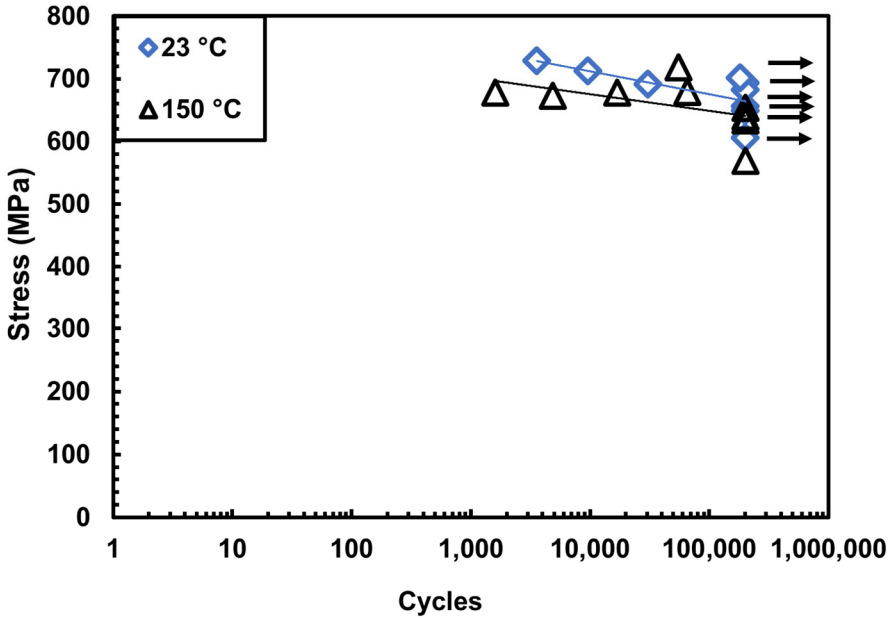

Figure 41. Actual maximum stress vs. cycles to failure (S-N) curve obtained for the 0/90 AM-PMC specimens at 23 and 150 °C.

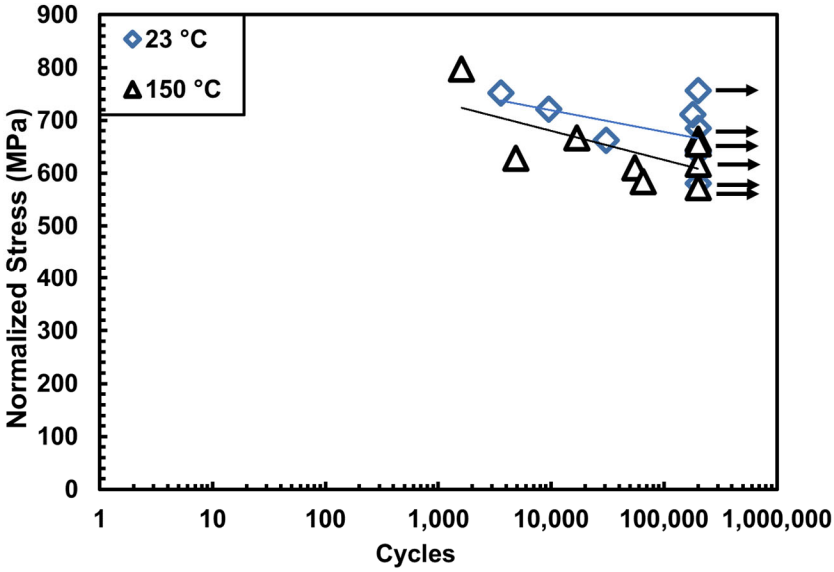

Figure 42. Normalized maximum stress vs. cycles to failure (S-N) curve obtained for the 0/90 AM-PMC specimens at 23 and 150 °C.

In addition to considerable data scatter, anomalous fatigue behavior is noted at both 23 and 150 °C. Results in Figure 42 show that specimens tested with higher maximum stress levels achieve fatigue runout while those tested with lower maximum stress levels produce shorter cyclic lives. The most drastic example of such behavior is represented by specimen 306-17, which achieved fatigue runout when tested with the highest maximum stress level of all specimens tested at 23 °C. We recommend that additional specimens cut from multiple panels be tested to gather a larger body of data to form statistically meaningful conclusions regarding the composite's fatigue performance. The degree of specimen-to-specimen variability inherent in the composite panels used in this work is too high. Many more specimens need to be tested to overcome the specimen-to-specimen variability and to produce statistically significant conclusions. Yet this preliminary study suggests that the S-N curves obtained at 23 °C and 150 °C (see Figures 41 and 42) have nearly the same slope, indicating that S-N data obtained at 23 °C and those obtained at 150 °C can be fitted with similar power law equations.

Next we consider the evolution of the stress-strain hysteresis response of the 0/90 specimens tested at 23 °C and those tested at 150 °C. Recall that several 0/90 specimens tested in fatigue at 23 °C produced the stress-strain hysteresis loops that gradually widened and became more "S" shaped as the fatigue cycling progressed (Figure 30). The elevated temperature specimens did not show the drastic "S" shaped deformations such as seen in Figure 30. The 0/90 specimens tested at 150 °C accrued damage with fatigue cycles. Such damage development manifested itself in the typical fashion by gradual widening of the stress-strain hysteresis loops as well as decreasing their slope. Specimen 306-5 (σ_{max} = 679 MPa, N_f = 65,563) produced stress-strain hysteresis response (Figure 43) closest to that noted for some 0/90 specimens tested at 23 °C (see Figure 30). Note that the final stress-strain hysteresis loop in Figure 43 widens

dramatically, but does not take on the “S” shape seen in the case of 0/90 specimens tested at 23 °C.

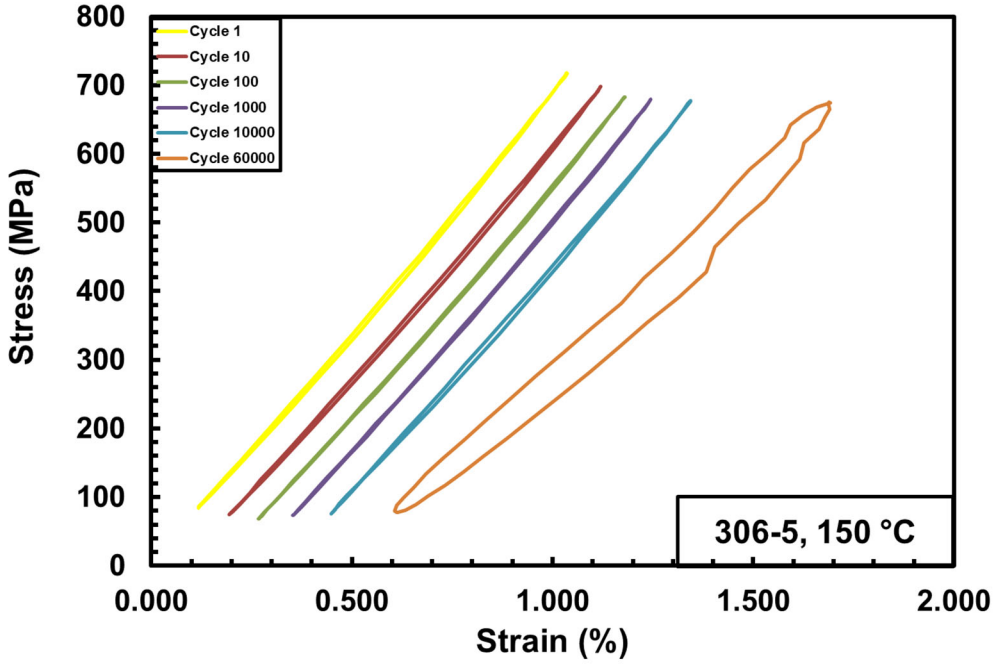

Figure 43. Evolution of the stress-strain hysteresis response for specimen 306-5 (σ max = 679 MPa, Nf = 65,563) tested in fatigue at 150 °C.

As expected, degradation of the hysteretic modulus with cycles was also noted in fatigue tests performed at 150 °C. However, the character of modulus degradation was somewhat different from that observed in fatigue tests performed at 23 °C. Specimens that achieved fatigue runout at 150 °C displayed little to no modulus degradation with cycles. Specimens that failed in fatigue at 150 °C displayed a somewhat more erratic modulus degradation behavior. Recall that in the case of specimens tested at 23 °C, the hysteretic modulus would initially decrease, then level out until failure such as seen in specimen 306-8 in Figure 32. Some specimens tested at elevated temperature exhibited an initial increase in modulus with cycles, followed by decrease

in modulus with cycles. Such behavior is not uncommon for the 0/90 composites and is attributed to fibers straightening out during early cycles. Yet this behavior was not seen in the room temperature tests.

Based on these observations, we conclude that the elevated temperature does affects the performance of the AM composite system. The matrix is the most temperature sensitive component of the composite. The changes in mechanical behavior seen in elevated temperature tests point to a softening of the matrix material. The straightening of fibers seen in elevated temperature tests, but not at room temperature could be due to the matrix becoming pliable enough for fibers to move. We also note that the X-Ray CT revealed many voids in the material around the first few surface layers. Elevating the temperature could soften the matrix enough to make these surface layers re-adhere to the rest of the composite panel, causing the difference in the appearance of hysteretic loops produced at room and elevated temperature. The damage mode could change, or the onset of the type of damage that produces the drastic "S" shaped hysteresis loops could be delayed enough for other damage modes to cause failure first.

5.5.1.2 Comparison of AM-PMC and TM-PMC Fatigue Performance at Elevated Temperature

Results of the current study produced at 150 °C are compared with the results of the previous study exploring the elevated temperature tension-tension fatigue of the NRPE/T650-35 material system. Table 19 presents the tension-tension fatigue results from prior work [17] for the NRPE/T650-35 material system at elevated temperature.

Table 19: Tension-tension fatigue results for the NRPE/T650-35 composite with 0/90 fiber orientation at 329 °C

Material System	Maximum Stress (% UTS)	Maximum Stress (MPa)	Cycles To Failure
NRPE/T650-35	90	740.1	2,756
NRPE/T650-35	90	740.8	1,148
NRPE/T650-35	88	723.9	10,916
NRPE/T650-35	85	699.6	11,286
NRPE/T650-35	80	658.0	23,768
NRPE/T650-35	75	618.4	121,136
NRPE/T650-35	70	576.3	200,000*
NRPE/T650-35	60	494.5	200,000*

* Fatigue run-out defined as $2x10^5$ cycles. Failure of specimen did not occur when the test was terminated

Elevated temperature fatigue performance of the AM-PMC specimens exceeds the fatigue performance of the NRPE/T650-35 composite with 0/90 fiber orientation. However, we note that the NRPE/T650-35 composite was tested at substantially higher temperature than the AM-PMC in this study (329 °C vs 150 °C). The NRPE/T650-35 material system achieved runout at 70% of its UTS and produced cyclic lives ranging from 1,148 to 2,756 cycles when tested with maximum stress levels set to 90% of its UTS. At 150 °C, the AM-PMC achieves runout at 82.5% of its UTS and producing a cyclic life of 55,158 cycles at 90% of its UTS. When tested with the maximum stress set to 80 %UTS, the NRPE/T650-35 material system survived only 23,768 cycles. It is important to compare the performance of the AM-PMC to that of the current state-of-the-art TM composites in order to ascertain that the benefits of the additive manufacturing technique are not achieved at a high cost of degraded mechanical performance. Yet we recognize that we cannot directly compare the performance of the AM-PMC at 150°C to that of the NRPE/T650-35 at 329°C because of the considerably different test temperatures. Should the data for a TM-PMC at 150°C become available, a direct comparison can be carried out.

However, it is worth mentioning that the NRPE/T650-35 material system is tailored for high temperature performance. Evaluating the AM-PMC next to this material system may not be entirely fair. However, the AM-PMC is intended for use in aerospace applications where high temperatures are common. Comparing the AM-PMC to the current state-of-the-art high-temperature composites is a good measure of how much AM-PMC has to improve.

5.6 Retained Tensile Properties

Assessment of retained strength and stiffness properties is helpful in evaluating the degree of damage caused to the composite by prior fatigue loading. Retained tensile properties of all specimens that achieved fatigue runout of 200,000 cycles were evaluated in tension to failure tests conducted at temperature of the fatigue test. Results are presented in Table 20. Note that specimen 306-9 exhibited anomalous tensile stress-strain behavior during the post-fatigue tension test (Figure 44). This anomalous behavior is likely caused by extensive damage build-up that occurred during fatigue. Because the retained elastic modulus for specimen 306-9 could not be readily measured, it is not included in Table 20.

Table 20: Retained tensile properties of the AM-PMC specimens subjected to 200,000 of prior fatigue at 23 or 150 °C

Panel/ Specimen	Fiber Orientation	Temperature (°C)	Initial Elastic Modulus (GPa)	Retained Elastic Modulus (GPa)	Modulus Retention (%)	Retained UTS (MPa)	UTS Retention (%)	Strain at Failure (%)
306-15	0/90	23	71.00	61.44	86.54	837.47	102.35	1.205
306-9	0/90	23	81.76	-	-	809.56	98.94	8.298
306-17	0/90	23	68.95	64.99	94.26	842.84	103.01	1.299
306-4	0/90	23	95.76	65.90	68.82	864.03	105.60	1.252
306-11	0/90	23	85.63	72.41	84.56	807.81	98.73	1.162
314-5	±45	23	14.06	11.67	83.00	97.44	105.52	2.256
314-13	±45	23	15.56	8.19	52.63	86.64	93.83	1.761
313-6	0/90	150	88.74	53.94	60.78	823.67	102.30	1.577
306-20	0/90	150	68.72	46.34	67.43	907.35	112.67	1.631
313-7	0/90	150	83.13	70.20	84.44	930.85	115.89	1.301
313-18	0/90	150	79.97	32.85	41.08	874.99	108.65	1.443

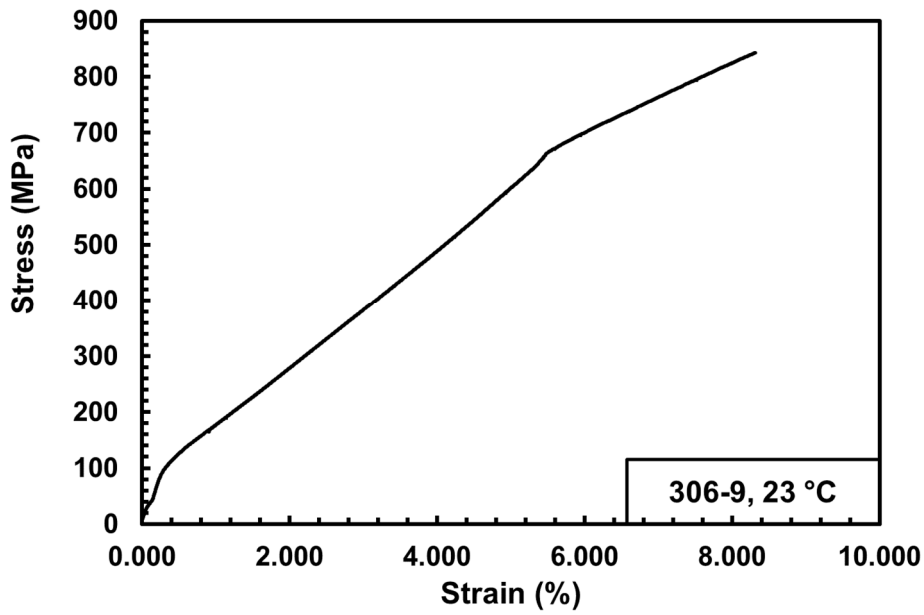

Figure 44. Post-fatigue tension to failure stress-strain curve for specimen 306-9

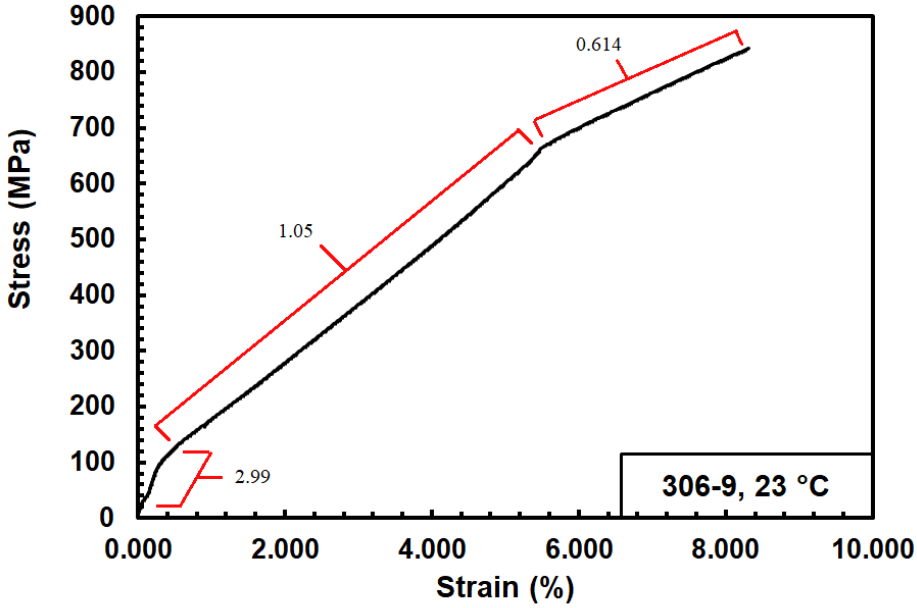

Figure 45. Modulus values for specimen 306-9, three distinct damage regimes. Modulus values are given in GPa

Specimen 306-9 exhibited the damage shown in Figure 27. The stress-strain loops in Figure 27 take on the same shape as the stress-strain curve in Figure 44, but with the exception of a further decrease in slope when the stress level exceeds 700 MPa. At this stress level the elastic modulus decreases further, suggesting the existence of a third damage regime in addition to those seen in the stress-strain loops of Figure 27. Each change in the slope of the stress-strain curve indicates a change in stiffness for the specimen. Whatever damage mechanism that caused the "S" shaped stress-strain loops in Figure 27 progressed even further after exceeding the stress level of the fatigue test (700 MPa). Figure 45 labels these three damage regimes for specimen 306-9 with the accompanying slopes for each.

It is not surprising, the 0/90 specimens tested in fatigue at 23 °C exhibit the best modulus retention. On average, 0/90 specimens subjected to prior fatigue at 23 °C retained 83.63% of

their modulus. Note that results obtained for specimen 306-9 are not included in this calculation. The ±45 specimens subjected to prior fatigue retained 67.82% of their modulus on average. The 0/90 specimens subjected to prior fatigue at 150 °C retained 63.43% of their modulus on average.

Prior fatigue at 23 °C has little effect on tensile strength. Both the 0/90 and the ±45 specimens subjected to prior fatigue at 23 °C retained 100% of their tensile strength. This result is particularly noteworthy for the ±45 specimens. It indicates that fatigue cycling at 23 °C do not appreciably affect the strength of the matrix resin. Likewise, prior fatigue at 150 °C did not affect the tensile strength of the 0/90 specimens – they retained 100% of their tensile strength.

Fatigue did not have an appreciable effect upon the strain at failure compared to the monotonic tensile tests. The 0/90 specimens had an average strain to failure of 1.226% and 1.230% for tension-to-failure and tension-tension fatigue respectively (specimen 306-9 is excluded in this average for being a clear outlier). Given that this is the fiber dominated direction (i.e. less dependent upon the matrix properties), it can be concluded that the unique microstructure generated through the additive manufacturing process does not have a deleterious effect upon the failure strain on the fatigued vs as processed specimens. The ±45 specimens displayed similar behavior. The ±45 specimens had an average strain to failure of 2.112% and 2.009% for tension-to-failure and tension-tension fatigue respectively. The values of failure strain for the fatigued specimens fall within the range of values of the tension to failure specimens, but there were only two ±45 specimens that made it to runout. The average of 2.009% would likely more closely match 2.112% if more specimens made it to runout. The lack of an effect of fatigue on strain to failure implies that the resin performs well in fatigue.

Elevated temperature did have an effect on strain at failure compared to room temperature. The average strain at failure of the 0/90 specimens fatigued at 150 °C (1.488%) was 17.6% higher than the room temperature tests. This is not a surprising observation given that the elevated temperature would make the fibers and matrix less stiff. However, the 0/90 specimens tested at elevated temperature did have a smaller strain at failure than the elevated temperature tension-to-failure average of 1.632%. It is possible that this is due to statistical scatter. It is also possible that the softening of the matrix and fibers allows the fatigue damage to proceed via an accelerated mechanism compared to what occurs at room temperature, resulting in a difference between the tension-to-failure average and the fatigue average.

5.7 Optical Microscopy

The purpose of examining the failed specimens under an optical microscope is to elucidate the damage and failure modes operating during particular loading histories. Examination of the 0/90 specimens tested in fatigue at 23 °C and at 150 °C revealed that the change in test temperature did not affect the failure mode. A typical optical micrograph of the 0/90 specimen tested in fatigue is shown in Fig II (specimen 306-10, T = 150 °C, σ_{max} = 673 MPa, N_f = 4,856).

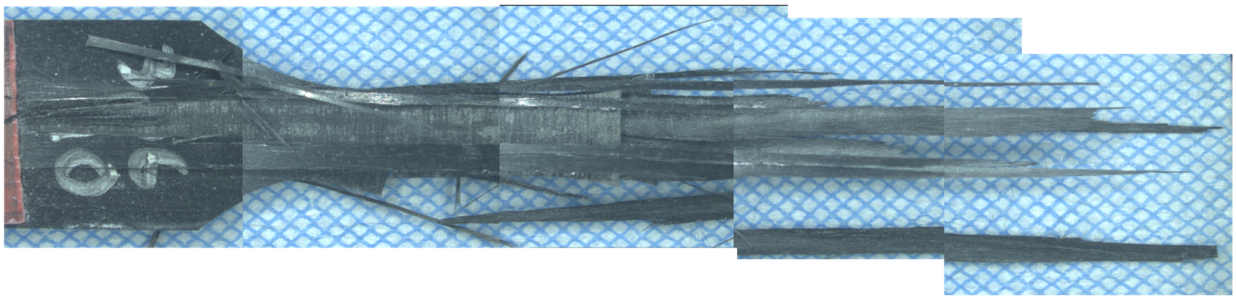

Figure 46. Optical micrograph showing typical failure of AD-PMC specimens with 0/90 fiber orientation (specimen 306-10, fatigue at 150 °C, σ max = 673 MPa, Nf = 4,856).

Micrograph in Figure 46 reveals severe delamination throughout the length of the specimen. Figure 47 presents stills from a high-speed video of specimen 313-4 developing extensive damage during a tension test at 23 °C. Ultimate failure of each 0/90 specimen was very messy and loud. Fiber fragments were sent flying in all directions and the length of the specimens became suffused with non-uniform damage.

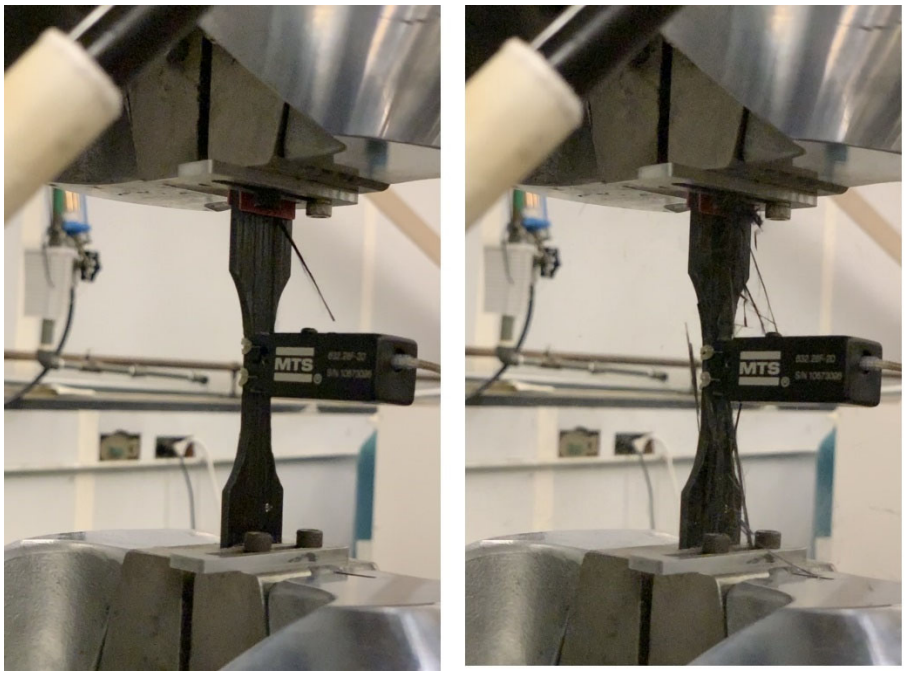

Figure 47. Specimen 313-4 before failure (left) and after failure (right)

The delamination of the 0/90 specimens was not neatly contained along any ply boundaries. This pattern of chaotic delamination can be attributed to the additive manufacture process used to fabricate the composite studied in this work. During traditional manufacturing, large sheets of preimpregnated carbon fibers are laid out in a near-monolithic whole. During additive manufacturing process, the fibers are laid down one fiber tow at a time. During AM, the fibers and the resin forming a single ply exist as separate entities, not all connected as one whole. As a result, the fibers and resin are not distributed evenly throughout the specimen. This uneven

microstructure creates an uneven state of stress within the specimen, causing the messy failure surfaces as the one seen in Figure 46.

The failure of the ±45 fiber orientation specimens occurred via the same mechanism, but was far less energetic. Optical micrograph showing typical failure of AD-PMC specimens with ±45 fiber orientation (specimen 314-15, fatigue at 23 °C, σ_{max} = 60 MPa, N_f = 14,932) is presented in Figure 48.

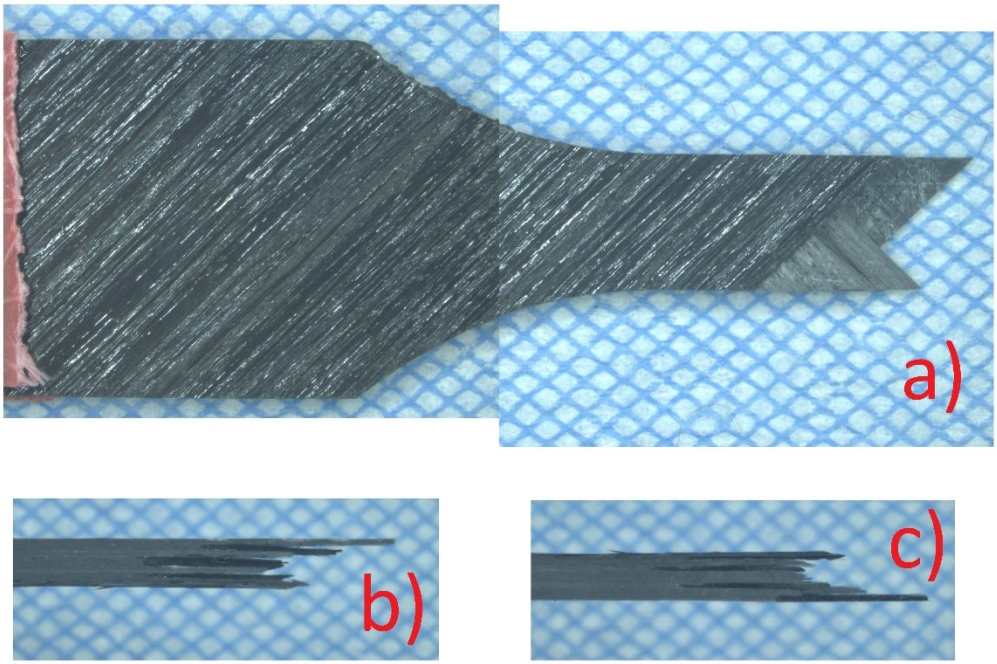

Figure 48. Optical micrograph showing typical failure of AD-PMC specimens with ±45 fiber orientation (specimen 314-15, fatigue at 23 °C, σ max = 60 MPa, Nf = 14,932). (a) Front view, (b) side view, (c) opposite side view.

The failure surface of the ±45 specimens (Figure 48) is much cleaner than the failure of the 0/90 specimens. The additive manufacturing process did not change the appearance of the failure surface, we still observe a typical V-shaped failure surface. Furthermore, in the case of ±45 specimen the delamination is limited to the immediate vicinity of the fracture surface.

Delamination did not extend along the length of the specimen, even in specimens tested at higher load levels and those with short cyclic lives. Limited delamination noted for the composite panel with ±45 fiber orientation indicates that the matrix has good interlaminar adhesion in this particular panel.

5.8 X-Ray Computed Tomography

X-Ray Computed Tomography (CT) images were collected by Dr. Jevan Furmanski at AFRL/RXCC to assist in understanding this material and its behavior on a deeper level. The unique nature of the additive manufacturing process necessitated this data collection as it creates a unique and uninvestigated microstructure that makes direct comparisons with TM-PMCs difficult. Figure 49 shows a typical image from this data collection.

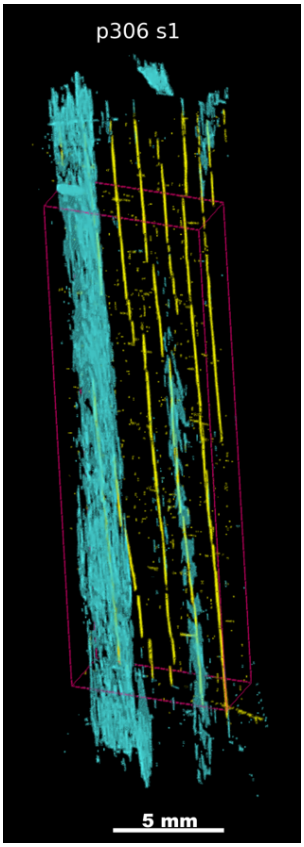

Figure 49. An X-Ray CT image of the gauge section of specimen 306-1

The purple box represents the gauge section of the specimens. The blue painted regions represent void space within the specimen, and the yellow painted regions represent cracks in the matrix. Blue and yellow features were extended outside and past the purple box in order fully capture the features within the gauge section. With few exceptions, the blue regions were limited to being located just under the rough "front" face of the specimens. This was the side facing up when the panels were being manufactured. There was extensive void content just at the surface that can be traced to the unique manufacturing process of this material. As the tows are laid down, the tows are compacted by the ones above them in the stacking sequence. The top ply has nothing to compact it, so it loosely adhered relative to the other plies in the panel. Some specimens displayed this quality in the second ply orthogonal to the top layer. The yellow cracks are limited to the smooth "back" face of the specimens and are likely due to a CTE mismatch between the panel and the print surface during the curing cycle.

5.8.1 Correlation of CT Images with Initial Elastic Modulus Measurements

Using the CT images collected by Dr. Furmanski, it is possible to qualitatively correlate the initial elastic modulus of the test specimens to the microstructure visible in the images. Figure 50 shows the results for panel 306 with 0/90 fiber orientation. Figure 15 is reproduced below for the reader's convenience.

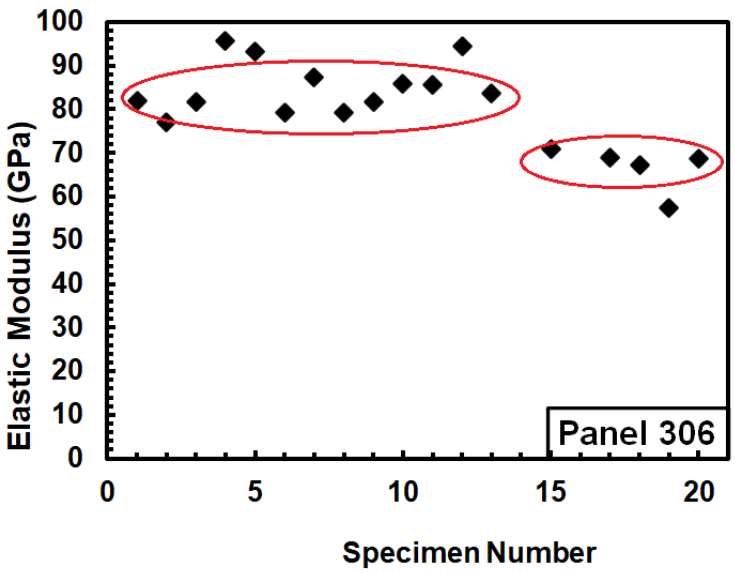

Figure 15. The two groupings of specimens in panel 306 with 0/90 fiber orientation. One grouping occurs at the 85 GPa level, and the other at around the 70 GPa level.

Data points in Figure 15 can be organized into two distinct groups. Recall that specimens 306-15 – 306-20 that produced lower modulus values clustered around 70 GPa, were cut at a 90° angle to specimens 306-1 – 306-13 that produced higher modulus values clustered around 85 GPa. The CT images reveal a large amount of matrix cracking on the back face of specimens 306-15 – 306-20 that produced lower modulus values. This type of matrix cracking not unique to specimens 306-15 to 306-20. Similar extensive matrix cracking can be found in the other specimens cut from panel 306 (i.e. the specimens with higher initial modulus values). Figure 51 shows X-Ray CT images of test specimens cut from panel 306. Specimens in Fig OO are ordered by descending initial modulus value. Modulus values are given in units of GPa.

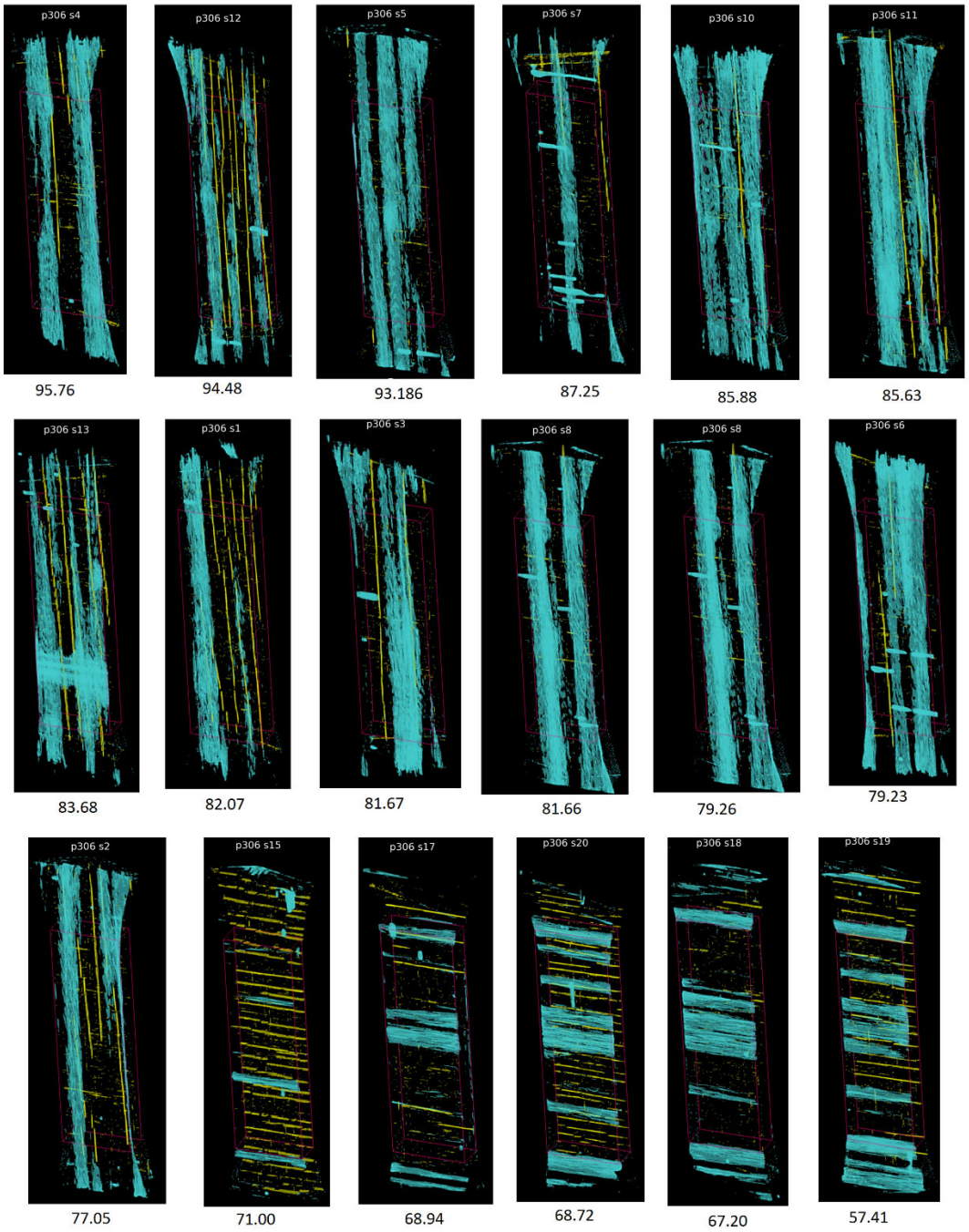

Figure 50. X-Ray CT images of test specimens cut from panel 306. Specimens are ordered by descending initial modulus value. Modulus values are given in units of GPa.

Images in Figure 51 reveal that extensive cracking is found in all specimens cut from panel 306. However, cracks in the specimens 306-1 and 306-12 are parallel to the specimen axis

and thus parallel to the loading direction. Conversely, cracks in specimens 306-15 and 306-20 are perpendicular to the loading direction. Clearly, cracks normal to the loading direction are much more likely to propagate even under small tensile loads. The detrimental effect of these internal cracks is clearly reflected in the initial modulus data. By and large there did not appear to be a correlation between the amount of void content and the initial elastic modulus.

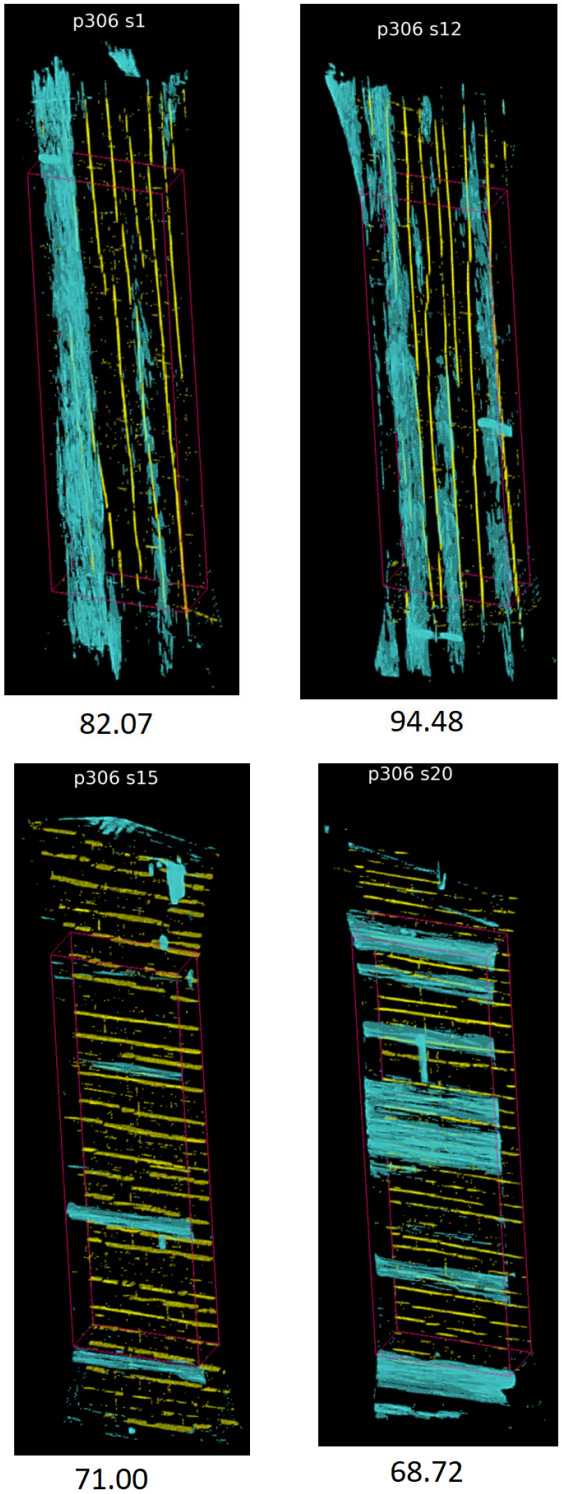

Figure 51. X-Ray CT images of specimens 306-1, 306-12, 306-15, and 306-20 with corresponding initial modulus values given in units of GPa.

Recall that initial modulus values obtained for specimens cut from panel 313 were much more consistent than those obtained for specimens cut from panel 306. Note that both panels had 0/90 fiber orientation. Furthermore, the specimen cutting plan was the same for both panels. Next we examine the X-Ray CT images of specimens 313-15 – 313-20 that were cut at a 90° angle to specimens 313-1 – 313-13 (Figure 52). Little to no matrix cracking can be found on these specimens. Specimen 313-20 represents an exception; it also has the lowest elastic modulus of the panel.

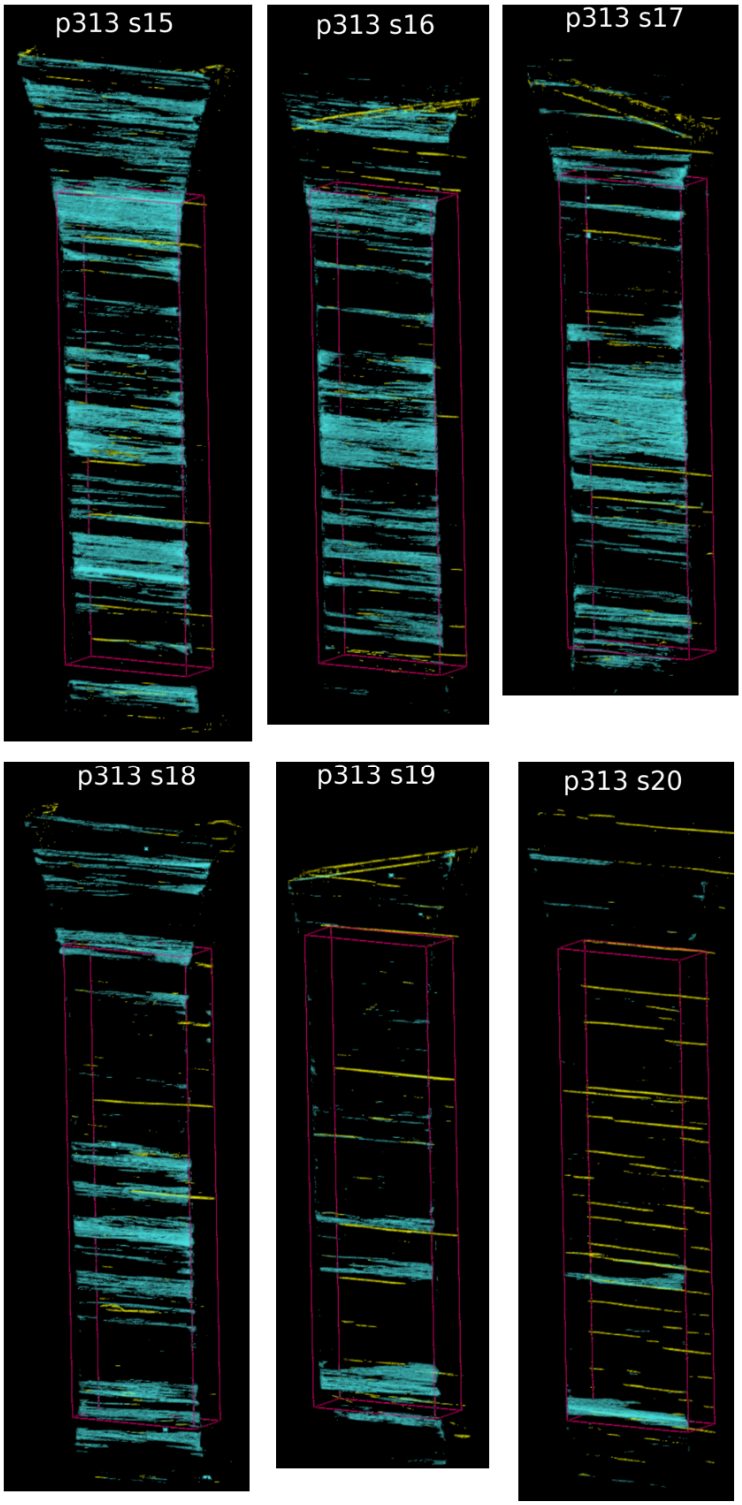

Figure 52. X-Ray CT images of specimens 313-15, 313-16, 313-17, 313-18, 313-19, and 313-20

Comparing the CT images obtained for specimens from panels 306 and 313, we conclude that matrix cracks formed during fabrication strongly influence the elastic modulus of the composite. Although both panels were fabricated via the same additive manufacturing process, there were some differences in the fabrication histories of the two panels. These differences caused matrix cracking in panel 306 that was not present in panel 313.

Recall that initial modulus values obtained for specimens cut from panel 314 with ±45 fiber orientation showed little variability, except for two outliers. Specimens 314-11 and 314-19 had significantly higher modulus values than the rest of the specimens cut from this panel (see Figure 18, reproduced here for reader's convenience).

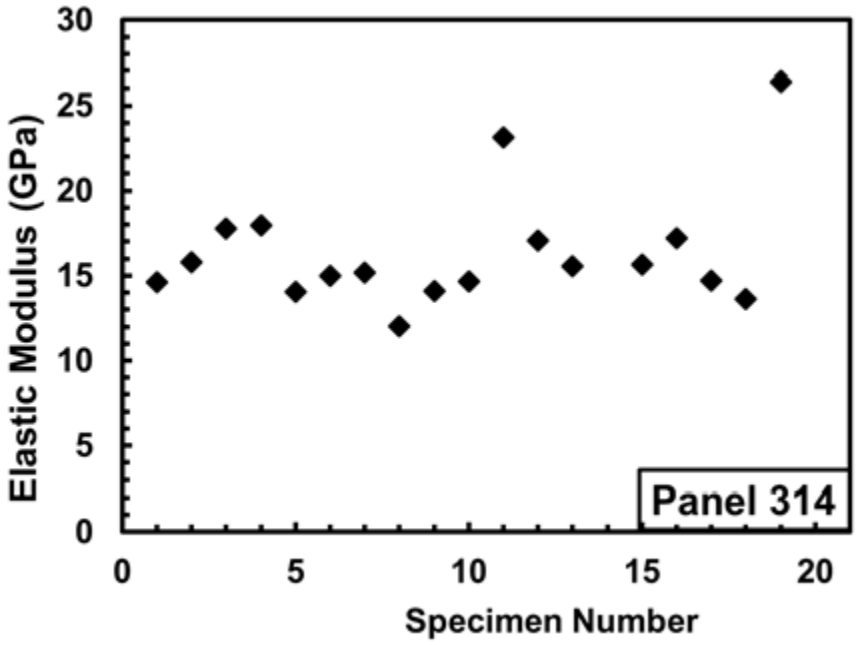

Figure 18. Modulus values for the specimens of panel 314

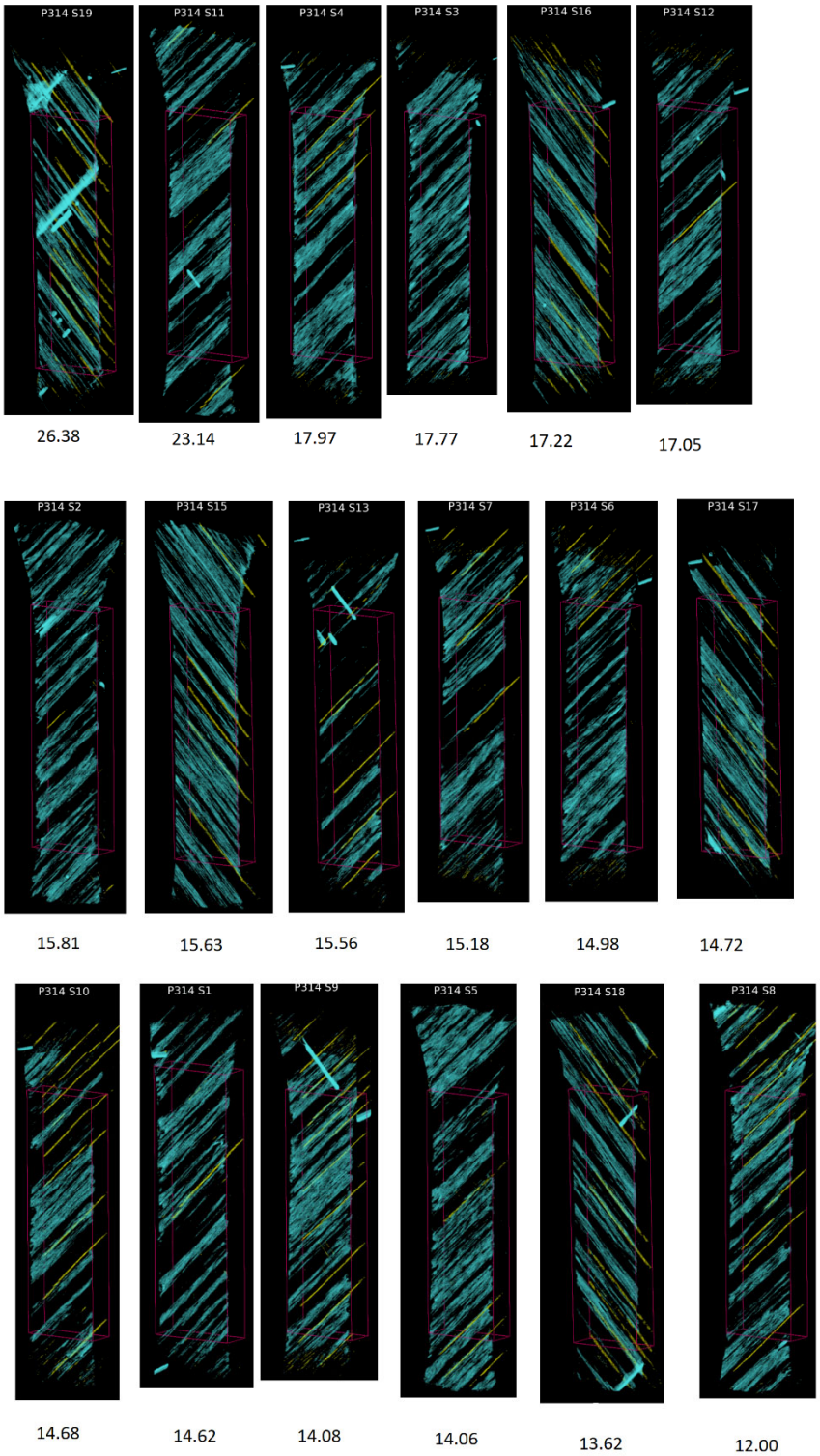

Figure 53. X-Ray CT images of test specimens cut from panel 314. Specimens are ordered by descending initial modulus value. Modulus values are given in units of GPa.

The X-Ray CT data (Figure 53) do not provide a clear explanation of these higher modulus values. The degree of matrix cracking has seemingly little to do with the elastic modulus values in this case. Consider for example the X-Ray CT image obtained for specimen 314-19 (Figure 54). Note the extensive cracking as well as the large amount of voids present. Yet specimen 314-19 produced the highest initial elastic modulus for that panel.

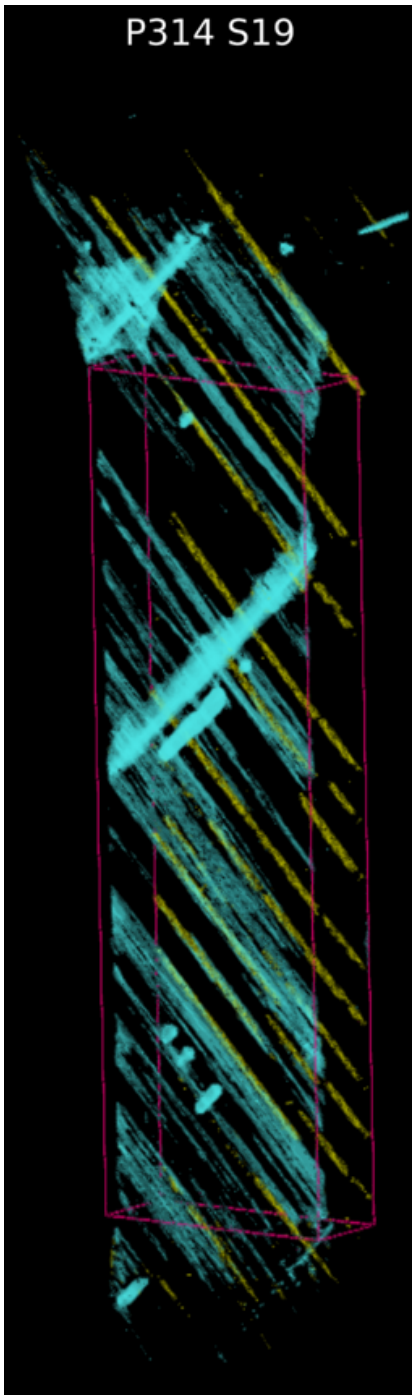

Figure 54. X-Ray CT image of specimen 314-19

5.8.2 Correlation of CT Images with Tension-Tension Fatigue Results

When discussing fatigue performance of the 0/90 specimens we alluded to the loud "crunch" noises heard during early cycles. These "crunch" noises are likely caused by the top ply peeling itself off. This conjecture is supported by the X-Ray CT images of the 0/90 specimens that show high void content just below the first layer. Apparently cyclic loading was sufficient to peel that layer completely off early in fatigue test. Recall that the "crunch" noise was heard only during the first dozen cycles. Evidently this particular damage was done early in cyclic life. The characteristic "crunch" noises were also heard during testing of 0/90 specimens that were cut at a 90° angle to the rest of test specimens in panels 306 and 313 (specimens 15-20 in both panels). However, in this case the noise was more muted indicating that damage did not have to propagate all the way along the length of the specimen. In these specimens the top layer has poor adhesion to the rest of the laminate. Furthermore, the top layer in specimens 15-20 in panels 306 and 313 has only 90° fibers. As a result, this layer has a lower load bearing capacity. Hence the top layer in specimens 15-20 is more readily peeled off during early fatigue cycling.

Additionally considerable scatter in the fatigue results can be explained using the X-Ray CT images. Consider the X-Ray CT images of the 0/90 specimens tested at 23 °C in fatigue with the maximum stress level set to 85%UTS (Figure 55).

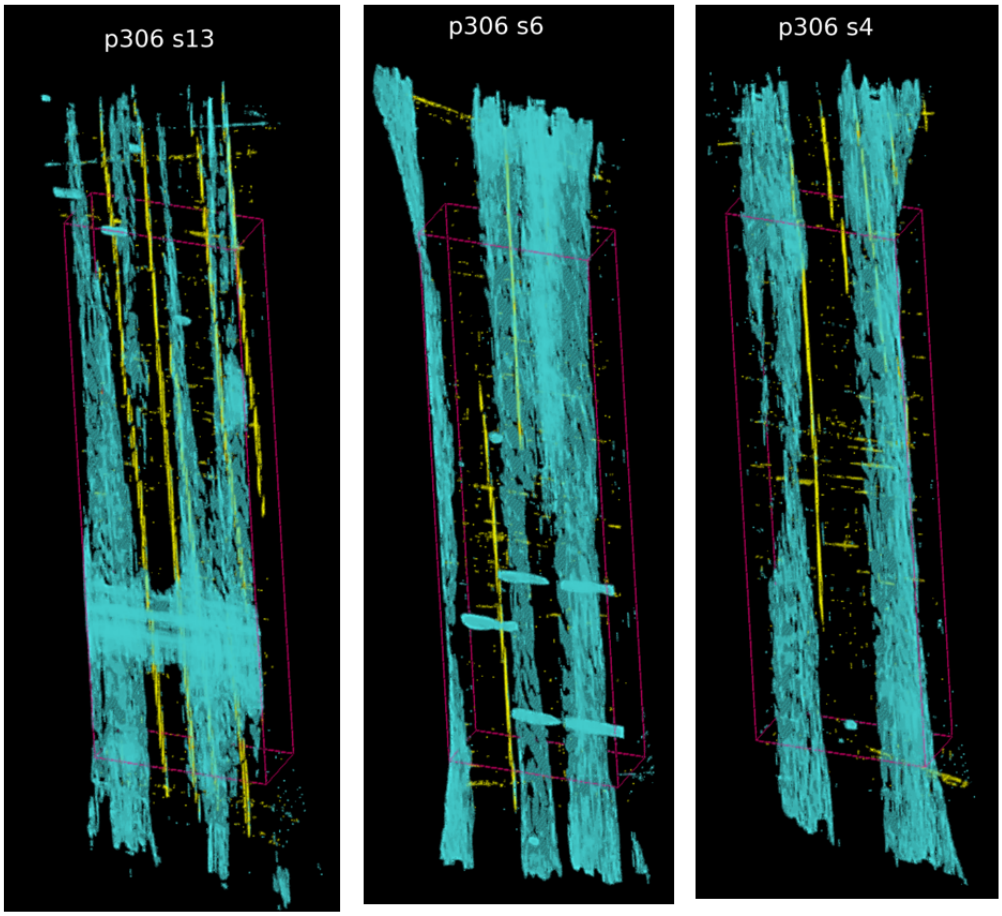

Figure 55. X-Ray CT images of specimens tested at 23 °C in fatigue with the maximum stress level set to 85%UTS. Specimen 306-13 (σ max = 691 MPa, Nf = 30,648). Specimen 306-6 (σ max = 702 MPa, Nf = 180,780). Specimen 306-4 (σ max = 693 MPa, Nf > 200,000).

Specimens 306-13 and 306-6 failed after 30,648 and 180,780 cycles, respectively. Specimen 306-4 achieved fatigue runout of 200,000 cycles. The X-Ray CT images of these specimens in Figure 55 show extensive void content running just under the top surface of each specimen. Specimens 306-13 and 306-6 exhibit transverse voids. This void content extends two plies deep into the specimen. Specimen 306-13 has considerable transverse void content within the gauge section, while specimen 306-6 has an appreciably lower void content. Specimen 306-4 has no transverse void content. This lack of transverse voids is behind a much better fatigue performance and longer cyclic life produced by this specimen.

The X-Ray CT images obtained for specimens tested at the elevated temperature are less readily correlated with the fatigue results. Figure 56 shows the X-Ray CT images of the 0/90 specimens tested at 150 °C in fatigue with the maximum stress level set to 85%UTS.

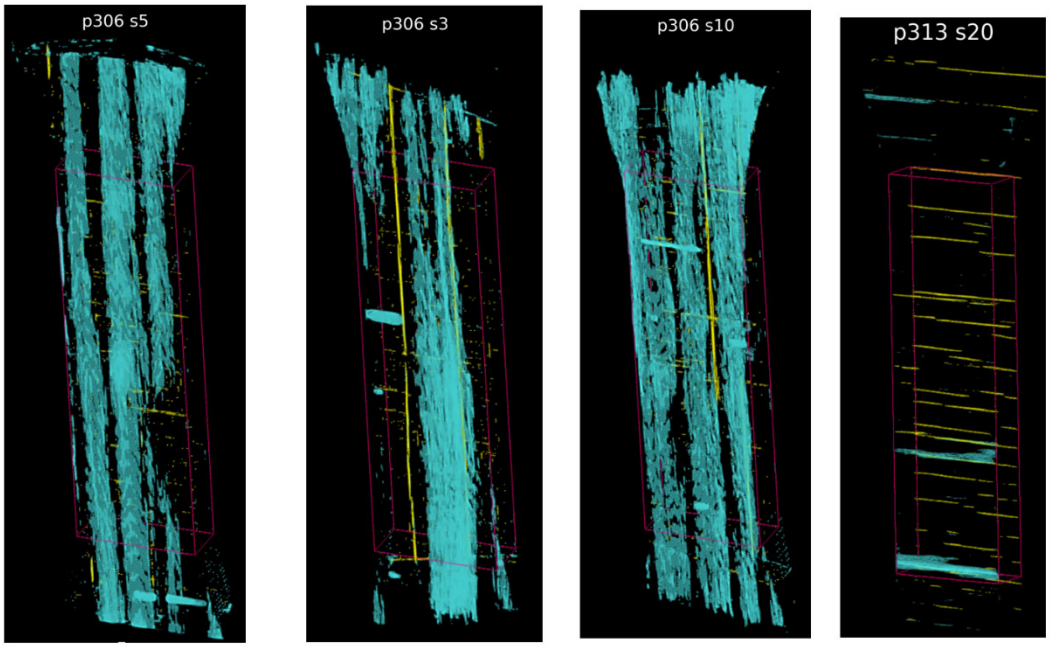

Figure 56. X-Ray CT images of the 0/90 specimens tested at 150 °C in fatigue with the maximum stress level set to 85%UTS. Specimen 306-5 (σ max = 679 MPa, Nf = 65,563). Specimen 306-3 (σ max = 678 MPa, Nf = 16,795). Specimen 306-10 (σ max = 673 MPa, Nf = 4,856). Specimen 313-20 (σ max = 678 MPa, Nf = 1,610).

Specimens 306-5, 306-3, 306-10, and 313-20 failed after 65,563, 16,795, 4,856, and 1,610 cycles, respectively. Results of the room temperature fatigue tests could be correlated with the surface void content. This is also the case for specimens 306-5, 306-3, and 306-10 tested at 150 °C. In contrast, specimen 313-20 shows virtually no surface void content, but has extensive matrix cracking normal to the loading direction. Specimen 313-18 (σ_{max} = 653 MPa, N_f > 200,000) also shows matrix cracking perpendicular to the loading direction, but to a much lesser extent (Figure 57). Specimen 313-18 achieved fatigue runout of 200,000 cycles, but it was tested

with the maximum stress set to a lower 82.5% UTS. Hence we cannot directly compare the microstructure and fatigue performance of specimen 313-18 to those of specimen 313-20. Additional testing and imaging is needed in order to determine whether matrix cracking normal to the loading direction plays a large role in fatigue response of the AM composite.

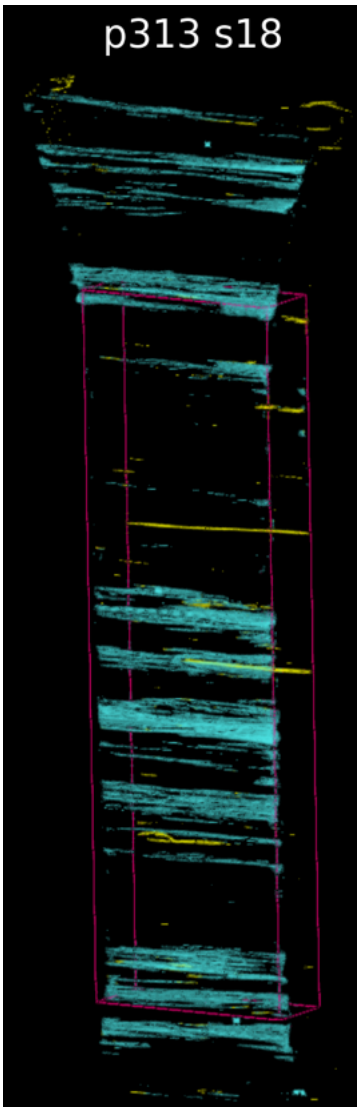

Figure 57. X-Ray CT image of specimen 313-18 tested at 150 °C in fatigue with the maximum stress level set to 82.5%UTS (σ max = 653 MPa, Nf > 200,000).

Figure 58 shows The X-Ray CT images of the ±45 specimens tested in fatigue at 23 °C.

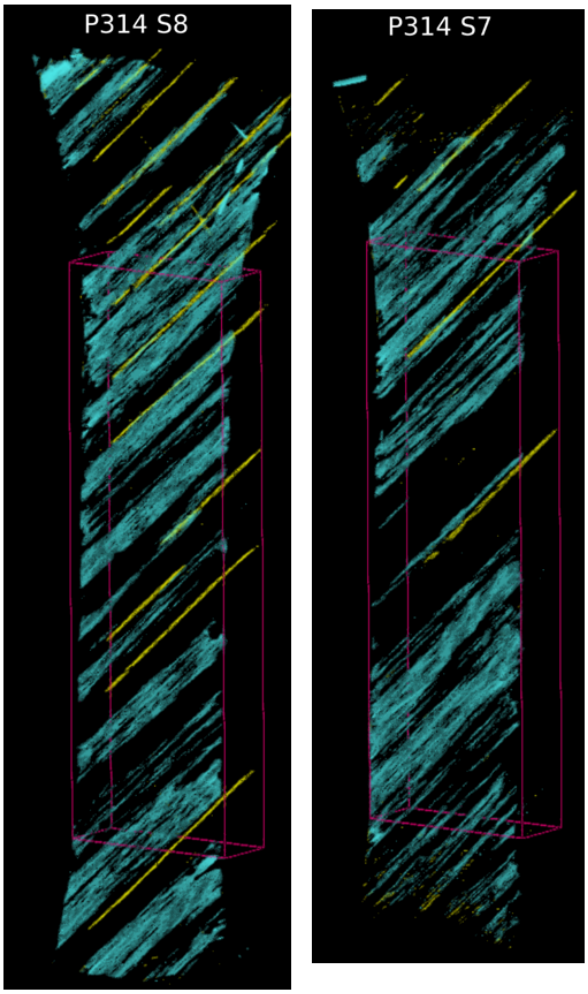

Figure 58. X-Ray CT images of specimen 314-8 (σ max = 59 MPa, Nf = 168,010) and specimen 314-7 (σ max = 59 MPa, Nf = 22,617).

Specimens 314-8 and 314-7 were both tested with maximum stress set to ~64%UTS. Specimen 314-7 failed after 22,617 cycles, while specimen 314-8 survived 168,010 cycles. The X-Ray CT images of these two specimens (Figure 58) have similar appearance. If anything, specimen 314-7 appears to be slightly less damaged, yet its cyclic life was dramatically shorter than that of specimen 314-8. Again, we recommend much additional testing and imaging in order to explore whether X-Ray CT is beneficial for evaluating the fatigue performance of the ±45 AM-PMC.

VI. Conclusions and Recommendations

6.1 Conclusions

The tension-tension fatigue behavior of an additively manufactured (AM) composite consisting of a UV photocured resin matrix reinforced with T1100 carbon fibers was studied in this work. Tensile properties of this novel AM-PMC were also determined. Properties and fatigue performance of both 0/90 and ±45 fiber orientations were examined. Specimens with 0/90 fiber orientation were tested in fatigue at 23 °C and at 150 °C, while specimens with ±45 fiber orientation were tested at 23°C only. In addition to measuring the tensile properties and evaluating the tension-tension fatigue performance of the AM-PMC, the results of this study were compared to the results of prior work produced for a traditionally manufactured (TM) PMC. Such comparison is particularly important as we need to ascertain that the benefits of additive manufacturing do not come at a cost of unsuitably low mechanical properties and performance of the resultant composite.

As expected, specimens with 0/90 fiber orientation produced considerably higher tensile properties (elastic modulus and tensile strength) than those with ±45 fiber orientation. As regards the elastic modulus, the AM-PMC material system performed as well as the traditionally manufactured (TM) aerospace-grade carbon-fiber reinforced composite. This conclusion is valid for both 0/90 and ±45 both fiber orientations. Tensile strength of the 0/90 AM-PMC was lower than that of the 0/90 TM-PMC (IM7/977-3 material system) despite the fact that AM-PMC was reinforced with higher-strength carbon fiber than the TM-PMC. The lower tensile strength of the 0/90 AM-PMC is attributed to the uneven state of stress within the specimen gauge section caused by the uneven distribution of fibers and matrix from the AM process. The tensile strength of the ±45 AM-PMC was also substantially lower than that of the ±45 IM7/977-3 material

system. This result suggests that the novel resin used in the AM-PMC is likely brittle and has a lower load bearing capacity.

In tension-tension fatigue, the AM-PMC with 0/90 fiber orientation produced a considerably higher fatigue limit than the ±45 AM-PMC. Increasing the temperature from 23°C to 150 °C had little effect on the tension-tension fatigue performance of the 0/90 AM-PMC. The tension-tension fatigue performance of the 0/90 AM-PMC system was worse than that of the 0/90 IM7/977-3 composite. Conversely, the ±45 AM-PMC delivered better fatigue performance than the ±45 IM7/977-3 material system. This was a positive sign, suggesting that the AM-PMC is nearly ready to compete with proven aerospace-grade composites in mechanical properties and performance. At 150 °C the fatigue performance of the 0/90 AM-PMC material system was considerably better than the fatigue performance of the traditionally manufactured NRPE/T650-35 material system at 329°C. This result is not entirely surprising as the NRPE/T650-35 material system was tested at a higher temperature.

Experimental results obtained for the AM-PMC exhibit considerable scatter. It was possible to correlate the data scatter with specific microstructural features and defects revealed by X-Ray Computed Tomography (TM). Analysis of the X-Ray TM images yielded better results for the 0/90 specimens than for the ±45 specimens.

6.2 Recommendations

Much additional testing of the AM-PMC needs to be accomplished before structural integrity and environmental durability of this novel material system can be assure. Due to the large amount of specimen-to-specimen variability encountered in this work, it is recommended that the AM fabrication process be further researched and optimized to yield consistent composite panels. Composite panels supplied for this research had a large number of defects at

the surface layer, as well as extensive matrix cracking on the back face. These defects need to be eliminated or at least minimized for this material to be safely and reliably used in structural applications.

There was a shortage of test specimens throughout this effort. Because so few tests could be performed and even fewer could be duplicated, results offer only limited statistical confidence. A substantial number of additional specimens should be dedicated to a follow-on effort in order to obtain statistically significant experimental data. Some portions of this research had to be delayed until such time when more composite panels become available. A fatigue study should be planned where the specimens would be subjected to a certain number of cycles, then scanned in the X-Ray CT in order to assess the damage progression. If interrupted fatigue studies are carried out, it would be prudent to use acoustic emission to monitor failure events during fatigue tests to gain insight into damage growth and to have a better idea when to interrupt testing for X-Ray CT scanning.

Bibliography

1. "Boeing 787 from the Ground Up" J. Hale. *Aeromagazine*, Qtr 4, 2006
2. Gibson, R. (2016). *Principles of Composite Material Mechanics* (4th Ed). CRC PRESS.
3. Callister, W., & David, R. (2020). *Fundamentals of Materials Science and Engineering: An integrated approach* (4th Ed). John Wiley & Sons.
4. Daniel, I. M., & Ishai, O. (2007). *Engineering mechanics of Composite Materials* (2nd ed). Oxford University Press.
5. Fischtziur, E. (2016, June 16). *'Grand-scale' autoclave for Boeing's biggest wings nears completion*. Boeing. from http://boeing.com/company/about-bca/washington/grand-scale-autoclave-for-boeing-s-biggest-wings-nears-completion 06-16-2015
6. Matsuzaki, R., Ueda, M., Namiki, M. *et al.* Three-dimensional printing of continuous-fiber composites by in-nozzle impregnation. *Sci Rep* **6,** 23058 (2016). https://doi.org/10.1038/srep23058
7. Quan, Z. et al. (2015). Additive manufacturing of multi-directional preforms for composites: Opportunities and challenges. *Materials Today*. 255. 10.1016/j.mattod.2015.05.001.
8. AlNatifat, Saleh A., "Tension-Compression Fatigue Behavior of 2D And 3D Polymer Matrix Composites at Elevated Temperature" (2015). Theses and Dissertations. 1925.
9. Talreja, R. (2003). *Fatigue of Composite Materials*. In Modern Trends in Composite Laminates Mechanics (pp. 281–294). Springer Vienna.
10. 3D Printing of Fibre-Reinforced Thermoplastic Composites Using Fused Filament Fabrication—A Review

11. Tekinalp, H.L.; Kunc, V.; Velez-Garcia, G.M.; Duty, C.E.; Love, L.J.; Naskar, A.K.; Blue, C.A.; Ozcan, S. Highly oriented carbon fiber-polymer composites via additive manufacturing. *Compos. Sci. Technol*. 2014, 105, 144–150
12. "Rapid energy-efficient manufacturing of polymers and composites via frontal polymerization," S.R. White et al. *Nature*, 09 May 2018
13. "UV-Assisted 3d Printing of Glass and Carbon Fiber-Reinforced Dual-Cure Polymer Composites" M. Invernizzi et al. *Materials*, July 2016
14. Continuous Composites. (2021) *PiCARD Monthly Report*. Unpublished Internal Report
15. MTS Series 810 Tuning and Calibration, MTS Systems Corporation
16. Lam, Benjamin C., "Mechanical Properties and Performance of a Novel Nano-Engineered Unitized Composite for Aerospace Systems" (2021). Theses and Dissertations. 4978.
17. Wilkinson, M. "Mechanical Properties and Fatigue Behavior of Unitized Composite Airframe Structures at Elevated Temperature". Master's thesis, Air Force Institute of Technology, Wright-Patterson AFB, Ohio, 2013.
18. S. G. Miller et al., "Out-Life Characteristics of IM7/977-3 Composites." NASA, Jul. 15, 2020
19. Toray Composite Materials of America Inc, "T1100S Intermediate Modulus Carbon Fiber", 8 May 2019, https://www.toraycma.com/wp-content/uploads/T1100S-Technical-Data-Sheet-1.pdf.pdf

REPORT DOCUMENTATION PAGE

Form Approved
OMB No. 074-0188

The public reporting burden for this collection of information is estimated to average 1 hour per response, including the time for reviewing instructions, searching existing data sources, gathering and maintaining the data needed, and completing and reviewing the collection of information. Send comments regarding this burden estimate or any other aspect of the collection of information, including suggestions for reducing this burden to Department of Defense, Washington Headquarters Services, Directorate for Information Operations and Reports (0704-0188), 1215 Jefferson Davis Highway, Suite 1204, Arlington, VA 22202-4302. Respondents should be aware that notwithstanding any other provision of law, no person shall be subject to an penalty for failing to comply with a collection of information if it does not display a currently valid OMB control number.
PLEASE DO NOT RETURN YOUR FORM TO THE ABOVE ADDRESS.

1. REPORT DATE *(DD-MM-YYYY)*	2. REPORT TYPE	3. DATES COVERED *(From – To)*
18-07-2022	Master's Thesis	June 2020 – September 2022

TITLE AND SUBTITLE

Mechanical Properties and Tension-Tension Fatigue Behavior of a Novel Additively Manufactured Polymer Matrix Composite at Room and Elevated Temperature

5a. CONTRACT NUMBER

5b. GRANT NUMBER

5c. PROGRAM ELEMENT NUMBER

6. AUTHOR(S)

Harber, Grayson M., Captain, USAF

5d. PROJECT NUMBER

5e. TASK NUMBER

5f. WORK UNIT NUMBER

7. PERFORMING ORGANIZATION NAMES(S) AND ADDRESS(S)

Air Force Institute of Technology
Graduate School of Engineering and Management (AFIT/EN)
2950 Hobson Way, Building 640
WPAFB OH 45433-7765

8. PERFORMING ORGANIZATION REPORT NUMBER

AFIT-ENY-MS-22-S-119

9. SPONSORING/MONITORING AGENCY NAME(S) AND ADDRESS(ES)

Intentionally left blank

10. SPONSOR/MONITOR'S ACRONYM(S)

11. SPONSOR/MONITOR'S REPORT NUMBER(S)

12. DISTRIBUTION/AVAILABILITY STATEMENT

DISTRUBTION STATEMENT A. APPROVED FOR PUBLIC RELEASE; DISTRIBUTION UNLIMITED.

13. SUPPLEMENTARY NOTES

This material is declared a work of the U.S. Government and is not subject to copyright protection in the United States.

14. ABSTRACT

The tension-tension fatigue behavior of a novel additively manufactured (AM) carbon fiber reinforced polymer matrix composite was studied. Tensile properties and tension-tension fatigue were investigated for the 0/90 fiber orientation as well as for the ±45 fiber orientation. Results obtained for the AM composite in this study were compared to the results obtained in previous studies for traditionally manufactured (TM) aerospace-grade carbon fiber/resin composite systems. The tension-tension fatigue performance of the additively manufactured material system with 0/90 fiber orientation was somewhat worse than that of the traditionally manufactured aerospace-grade composites with 0/90 fiber orientation at both room and elevated temperature. The additively manufactured material system ±45 fiber orientation exhibited better tension-tension fatigue performance than the ±45 aerospace-grade composite. The AM composite exhibited considerable degree of specimen-to-specimen variability, and consequently considerable data scatter. The additive manufacturing process shows considerable promise for rapid and cost-effective fabrication of composite parts. However, at present additive manufacturing produces composites with numerous internal defects and unordered microstructure that cause wide variability in both the mechanical properties and mechanical response of each specimen. Until a consistent mechanical response can be achieved for each specimen, this material will be unsuitable for structural applications.

15. SUBJECT TERMS

Composite, Additive Manufacturing

16. SECURITY CLASSIFICATION OF:			17. LIMITATION OF ABSTRACT	18. NUMBER OF PAGES	19a. NAME OF RESPONSIBLE PERSON
a. REPORT	b. ABSTRACT	c. THIS PAGE			Name of Advisor, AFIT/ENY
U	U	U	UU	116	19b. TELEPHONE NUMBER *(Include area code)* (937) 255-3636, ext 4641 (marina.ruggles-wrenn@afit.edu)

Standard Form 298 (Rev. 8-98)
Prescribed by ANSI Std. Z39-18